Interaction Notes

Note 208

March 11, 1974

THE TRANSIENT CHARACTERISTICS OF THE CONICAL SPIRAL ANTENNA*

J. A. Landt
E. K. Miller

Lawrence Livermore Laboratory
Livermore, California

ABSTRACT

The short-pulse characteristics of the conical spiral antenna are examined in detail. The antenna is analyzed using a time-domain integral equation. We first discuss various peculiarities associated with the numerical solution procedure, including the effects of high Q, low-frequency resonance, and impedance loading of the antenna. We then direct special attention to the radiated-pulse properties of the antenna for various types of time-varying excitation. We conclude with a quantitative assessment of the antenna's fidelity under pulsed conditions and present an approach to obtaining the desired radiated-pulse shape by tailoring the time variation of the applied antenna voltage.

*This work was performed under the auspices of the Atomic Energy Commission and the Defense Nuclear Agency.

CONTENTS

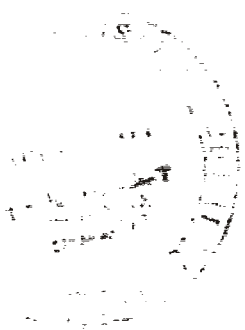

INTRODUCTION

The conical spiral antenna belongs to the class of antennas characterized as frequency independent over some operating band. Yet it has been found that such antennas are not able to radiate short pulses with high fidelity, even those having spectra confined to the antenna's operating band. This phenomenon is caused by the nonstationary phase center of the antenna in the frequency sense, which in the time domain translates to a time dispersion of the radiated pulse.

Other aspects of the transient response of conical spiral antennas have not been well understood, since previous studies of this antenna have generally been confined to the frequency band where the antenna is operating in a frequency-independent mode.[1-4] Consequently, our study is addressed to determining the behavior of conical spiral antennas both within and outside of the normal operating band.

The results presented here were derived as part of a study to determine the response of conical antennas to EMP illumination. The procedure followed was to calculate the quantities of interest using a time-dependent integral-equation model for wire structures. In the course of this study some interesting facets of the pulse characteristics of conical spirals were demonstrated by the numerical results. We will discuss some of these results here.

NUMERICAL SOLUTION

Integral equations for wire and surface structures for both frequency- and time-domain analysis have been derived and successfully used. Descriptions of some of this work can be found elsewhere.[5-7] The results presented here were obtained using a time-domain version of the thin-wire, electric-field integral equation. This time-dependent integral equation can be solved via time stepping and permits a much more efficient solution to be realized for some classes of problems than would be possible using a frequency-domain approach.[8] Generally speaking, the time-domain integral equation yields greater solution efficiency than that afforded by a frequency-domain approach when the source configurations to be considered are relatively few in number but are broad-band in character as typified by pulses short compared with the maximum structure dimensions.

The time-domain solution process begins by developing a piecewise, linear, wire approximation (total of N pieces or segments) to the actual structure of interest in a fashion similar to that used for the frequency domain. While frequency does not explicitly play a role in this process, the maximum segment size used to develop the model must take into account the wavelength of the highest frequency component for which solution accuracy is to be maintained.

After the structure geometry has been selected, a time-dependent interaction matrix is computed on the basis of the piecewise linear model. Multiplication of the interaction matrix's inverse by the distribution of total tangential electric field existing over the structure at a given time step yields the corresponding current distribution at that particular time step. Since the initial electric-field distribution is that due to

the known exciting source, the starting current values are also known. At subsequent time steps the total field becomes a summation of the known applied fields plus that reradiated by known currents induced at an earlier time. Consequently, this procedure is basically that of solving an initial-value problem.

The solution process is terminated when the induced currents have decayed to values regarded as numerically insignificant or where the resonance characteristics of the structure lead to currents that decay with a fixed frequency and decay rate, so that analytical extrapolation in time of the computed waveform can be performed. In either case, a time history of the current excited on each of the N structure segments is obtained for the given exciting source. A subsequent Fourier transform to the frequency domain can then be performed in order to obtain such characteristics of interest as input impedance, radiation patterns, etc., as a function of frequency.

Although a gaussian pulse is perhaps most convenient to use for the time variation of the exciting field,[8-10] other waveforms can, of course, also be employed. For EMP calculations for example, a commonly employed four-term analytical expression for the EMP field was used. On the other hand, experimentally measured waveforms could be employed as well. The essential point is that the structure model should have been so developed as to permit resolution of the highest frequency components in the exciting field. Once a transient solution has been obtained for a given exciting field, convolution or other procedures may be employed to determine the response to other field time variations.

It must be emphasized however, that the solution is dependent on source geometry and that any change in source exitation, such as, for example, the polarization or incidence angle of a plane-wave field, would require the solution to be repeated. This is in contrast to the more familiar frequency-domain approach, where the admittance matrix obtained from a moment method permits any source distribution to be handled, but which on the other hand is valid for only a single frequency.

Normally, for the time-domain solution, one chooses a source waveform most directly of interest for the intended application. For the EMP problem we might then consider only EMP-type waveforms. Since the impedance characteristics of any device that might be connected to the antenna terminals may not be known apriori, it might be necessary to repeat the calculation for several different values of the load impedance. This is not necessary though, if instead the input impedance of the structure excited as an antenna is obtained over the frequency range of concern, for, given the input impedance at a given port and the short-circuit transfer admittance of the antenna for the same port, it is possible to obtain the current flowing through an arbitrary load impedance, using the frequency-domain formula:

$$I_L = \frac{I_{sc} Z_A}{Z_A + Z_L} \qquad (1)$$

Here, $I_{sc} = Y_T E_{inc}$, where E_{inc} is the field strength of the incident plane-wave field and Y_T is the transfer admittance.

It is thus useful, in connection with using a time-domain calculation to determine an antenna's EMP response, to also calculate its input impedance as a function of frequency. Some results obtained from that analysis as well as the EMP-response calculations are included below.

NUMERICAL RESULTS

Antenna Characteristics

The initial time-domain calculations made for the conical spiral were performed for the structure excited as an antenna. Gaussian-pulse excitation was used for this purpose, as this same source waveform had been found useful for prior calculations involving linear dipoles and circular loop antennas. However, the conical spiral is sufficiently different from these antennas that its unloaded response to gaussian-pulse excitation was found unsuitable for the time-domain calculation as is demonstrated below.

Figure 1a shows the geometry of a 2-1/2-turn, two-arm spiral having a cone half-angle of 10 deg, a wire radius of 0.003 m, and a total wire length of 3 m. In Fig. 1b we observe that the input current to the antenna decays only slightly with time. The reason for this is evidently due to the fact that the conical spiral has a low-frequency cutoff below which it will not radiate very efficiently. As a result, the energy of the gaussian pulse, which extends to dc, is only partly radiated in the operating band of the structure, with the remainder trapped on it as in a resonant cavity.

Figure 1c demonstrates this more graphically. It plots contours of constant current as a function of time and distance along the spiral arms (measured from the feed region). In this figure, the antenna feed region is at the origin (i.e., where length = 0), positive currents are plotted as heavy lines, negative currents are plotted as dotted lines, and the increment between contour lines is 0.3 mA. After the initial current pulse is launched, and as it propagates down the arms of the antenna, it is seen to decrease in amplitude and to spread out due to dispersion. Upon its first reflection from the ends of the antenna and subsequent transits however, the antenna-current decay rate is much reduced.

The slow loss of energy at late times can be seen in the boresight radiated far field, measured parallel to the source region, plotted in Fig. 1d. At early times, the time behavior of the radiated field approximates an inverse chirp, decreasing in instantaneous frequency with time. Since radiation at a given frequency is most efficient where the antenna circumference is approximately one wavelength, this result singly demonstrates that the current pulse is propagating down a structure of increasing circumference.

After the initial burst of radiation from the antenna, there is relatively low-amplitude field observed thereafter even though, as seen in Fig. 1b, the current itself remains of high amplitude, showing that the energy remaining on the antenna, being of low frequency, is not radiated efficiently by the spiral.

The calculations discussed above demonstrate the difficulties associated with obtaining accurate frequency-domain results from a Fourier transform of the calculated transient response of a conical spiral excited by a gaussian pulse using a time-domain integral equation. The current has not decayed sufficiently in amplitude, even after 10 transit times (600 time steps) of the antenna, to permit an accurate Fourier transform to the frequency domain. At the same time the antenna temporal characteristics are not regular enough to allow an analytic extrapolation to future time to permit the time calculation to be terminated. Consequently, it is necessary to consider using alternative exciting-pulse waveforms if the time-domain calculation is to be useful for obtaining frequency-domain data.

A second time-domain calculation was performed, using the derivative of a gaussian pulse for the exciting source, because its spectrum goes to zero at zero frequency. A series of figures similar to those corresponding to Fig. 1 are included in Fig. 2 for this source waveform.

In Fig. 2a we observe that while initially the input current to the antenna does decay somewhat more rapidly as a function of time than for Fig 1b, accurate extrapolation, or a Fourier transform, cannot be performed after the number of transit times shown. Note too, that the radiated field has little resemblence to the exciting pulse.

To more effectively confine the spectrum of the exciting pulse to the bandwidth of the conical spiral, a third waveform was chosen. This was that of a harmonic sinusoid centered at a frequency in the bandpass of the conical spiral, and modulated with a gaussian envelope. The spectrum of this pulse was chosen so as to have an amplitude of 0.001 at the low-frequency resonance of the spiral. Figure 3 shows the results of this calculation. There it may be seen that after the initial feed-region current pulse produced by the exciting source, there is very little current reflected back to the feed region of the antenna from the ends, thus allowing the calculation to be terminated after only a few transit times.

This current waveform is therefore well suited for Fourier transformation to the frequency domain.

Figures 3d and 3e show the results obtained from Fourier transforming the input current on this antenna to the frequency domain. There we see a relatively frequency-independent behavior exhibited by this antenna, where the conductance and susceptance are only slowly changing with frequency, but below which low-frequency resonances occur. Also note that below the low-frequency resonance, no information was obtained because the exciting pulse contains very little energy in this region.

There is another approach to obtaining time-domain results useful for determining frequency-domain characteristics. Instead of changing the exciting waveform to confine its spectrum to the operating band of the antenna, it is possible instead to load the antenna with a resistance chosen to obtain an external damping of the antenna. Because it is known that the input impedance of conical spirals generally falls in the range between 300 and 400 Ω, a 350-Ω load impedance was used for this calculation.

The results, obtained again for a gaussian-pulse excitation, are shown in Fig. 4. The input waveform is seen to be confined to numerically significant current values for only the first reflected pulse, beyond which the current is essentially zero. This waveform can be Fourier transformed to obtain frequency-domain results for the input admittance that include the effect of the 350-Ω load. Upon calculating the input impedance of the antenna-load combination, the load impedance can be subtracted, and what remains is the antenna input impedance (or admittance). These results are shown in Figs. 4d and 4e. From a numerical computation viewpoint, it may be appreciated that the usefulness of including a load impedance is not confined to determining physical loading effects alone, but may be exploited as well to permit earlier termination of the time-domain calculation with relatively little loss of information and providing data

over a wider band than those found using the pulsed sinusoid employed above.

Scattering Characteristics

Figure 5 shows several results for EMP excitation of the conical spiral antenna. The current at the feed point of the antenna is shown for (1) EMP field incident from the boresight direction, with the electric field aligned parallel to the antenna feed region, for short circuit conditions (Fig. 5a) and for a load of 350 Ω (Fig. 5b), and (2) for a load of 350 Ω (Fig. 5c), with the field incident broadside to the antenna axis, and the electric field aligned parallel with the antenna axis. These results, obtained for the antenna previously considered, illustrate that although this antenna is relatively small compared to the wavelength at the peak of the EMP spectrum, short-circuit currents of appreciable magnitude (of the order of 4 A) are still excited by the EMP waveforms.

It is possible to determine the response of the conical spiral to other waveforms for different loads by using the transfer admittance shown in Figs. 6a, b, c, and d, and utilizing the input impedances as calculated above. This transfer admittance relates the current driven through a 350-Ω load connected to this conical spiral antenna for an incident field of 1 V/m at all frequencies and for the incident wave orientation used for Fig. 5b.

Pulse Shaping

As a final application of the time-domain calculation to the conical spiral antenna, we consider the possibility of pulse shaping. For this purpose, the antenna was excited with a gaussian pulse and several derivatives (up to the fourth) of the gaussian pulse. Figure 7 shows the driving-point voltage (solid curves) and the corresponding radiated field (dotted curves) in the boresight direction. The actual peak driving voltage was 1 V in each case, and the scales were altered for plotting these voltages. There is little correlation between the applied voltage and the resulting far-radiated field.

We may then ask the question, "What driving-point voltage is required in order to obtain a desired far-field time characteristic?" Two approaches might be considered to this problem. One approach would be to obtain the pulse response of the antenna, and from the far field that this produces, determine (by inversion of the convolution integral) the time variation of the exciting source actually required to produce the desired far field.

Alternatively, in the frequency domain, we can divide the far-field transfer function of the conical spiral (Fig. 8a) into the spectrum of the desired waveform to obtain the frequency variation of the required exciting field (Fig. 8b). Upon Fourier transforming the latter to the time domain, we can obtain the time waveform of the required excitation to generate the desired far field (Fig. 8c). This process is illustrated by the graphs shown in Figure 8, using as the desired waveform the third derivative of the gaussian pulse. The required pulse in the time domain may be seen to begin with a rather low frequency, and to increase very sharply in effective instantaneous frequency, beyond which the pulse slowly decays. This may be accounted for by noting that the lower frequency radiation occurs from regions on the antenna away from the vertex, so that any low-frequency far fields required to coincide with higher frequencies produced near the vertex would have to be radiated in advance.

Also shown in Fig. 8d is the computed far-radiated field that results from using the time waveform of Fig. 8c as the exciting pulse. The far field obtained using the synthesized applied waveform agrees within the numerical accuracy to that actually specified, as can be appreciated by comparing the field of Fig. 8d with the solid curve of Fig. 7d.

Although the test field used here may not be one sought for in actual application, and the pulse required to generate this field might be too complex to be realized, this same general procedure could be used to determine bounds on radiated fields permissible using realizable pulses. Consequently, this procedure could determine practicable far-field waveforms that include the antenna response itself as part of the pulse-shaping network.

DISCUSSION

The currents shown in Fig. 5 illustrate that coupling of EMP to conical spirals can be significant. As a result of this observation, and because conical spirals are widely used in communications, command, and control systems, a parameter study of the conical spiral antenna was completed. The results of this study are summarized in Appendix A. The input impedance of all of these conical spiral antennas was designed to be approximately 240 Ω, using Fig. 9 of Ref. 3. The cone half-angles cover the range from 5 to 20 deg, and the wire pitch angles extend from 60 to 80 deg. The total length of wire used in these antennas was 6 m. These data can be used to estimate the EMP response of conical spiral antennas connected to loads other than the 240 Ω by employing Eq. (1).

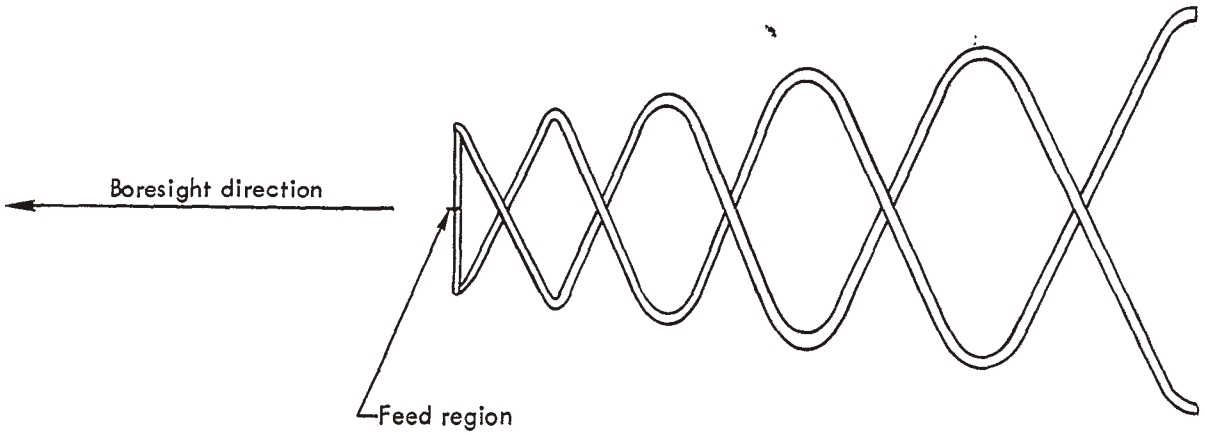

Fig. 1. Characteristics of a conical spiral antenna driven by a gaussian voltage waveform. (a) Antenna geometry. (Continued on the following three pages.)

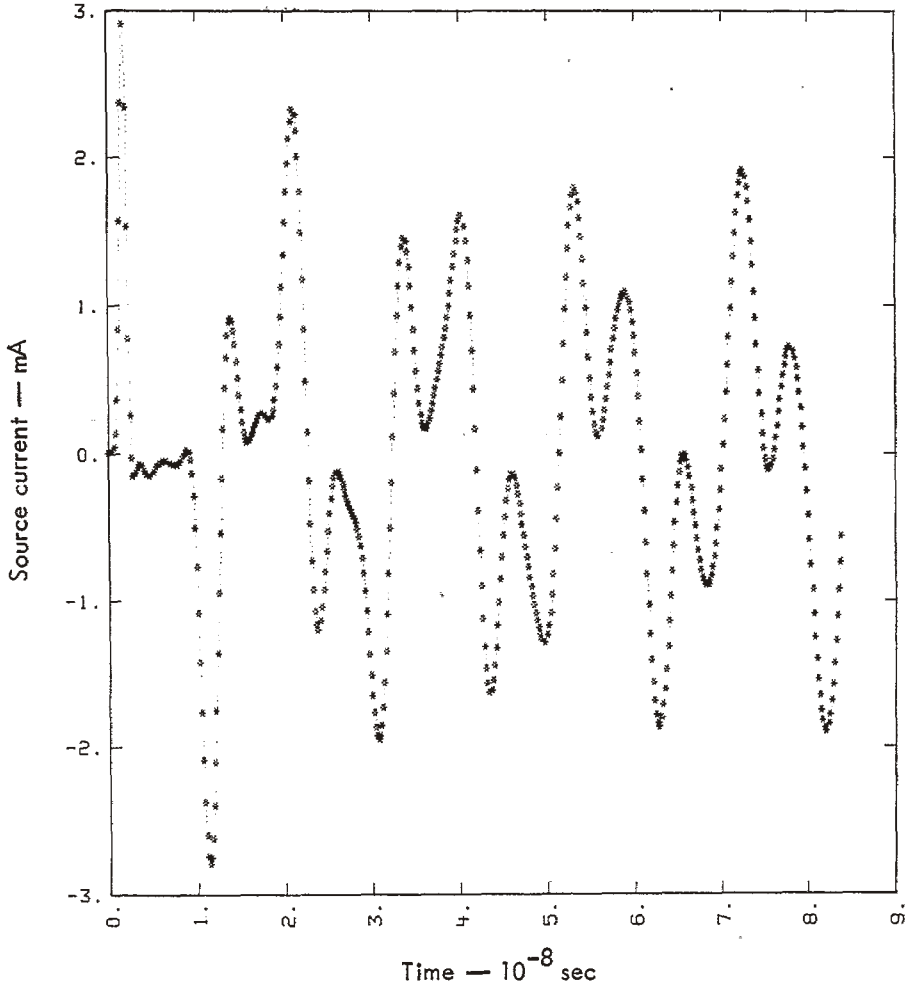

Fig. 1. (Continued.) (b) Driving-point current.

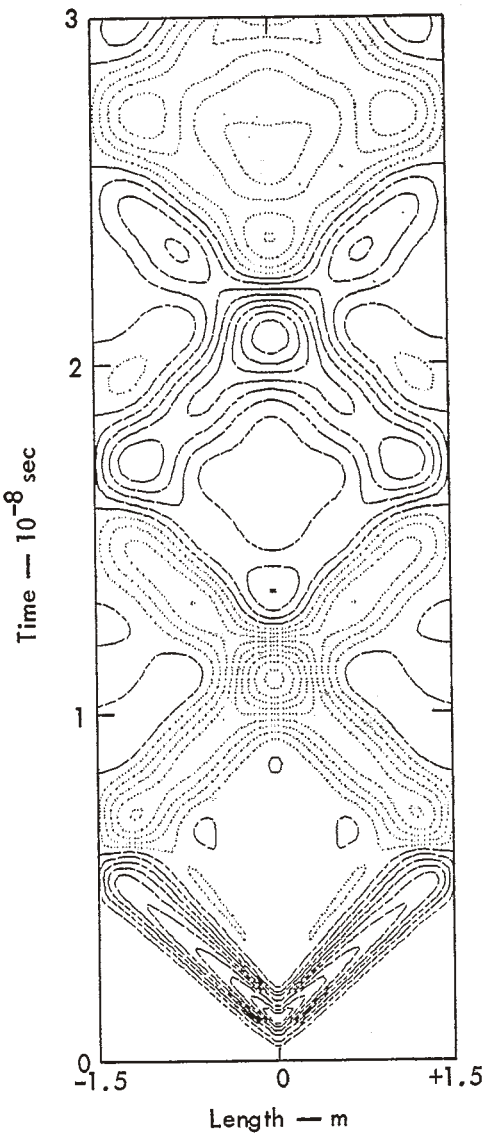

Fig. 1. (Continued.) (c) Space-time contours of constant current.

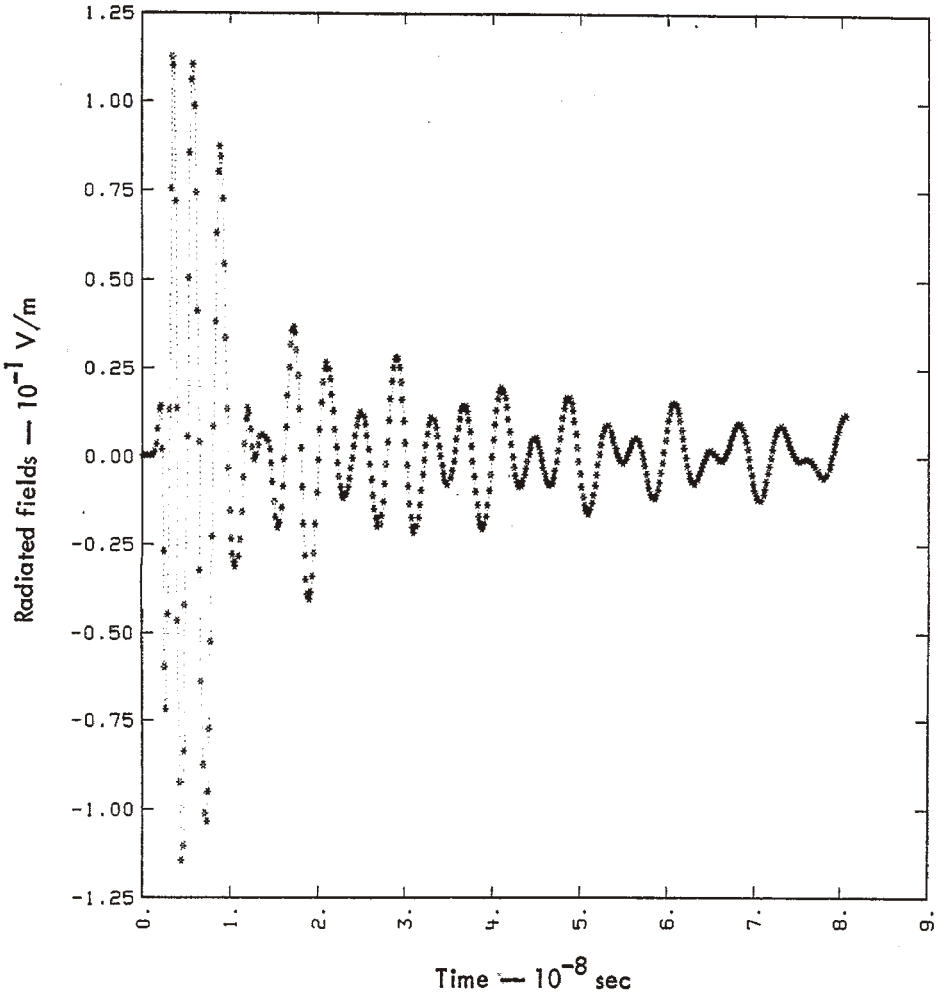

Fig. 1. (Continued.) (d) Radiated far field in boresight direction.

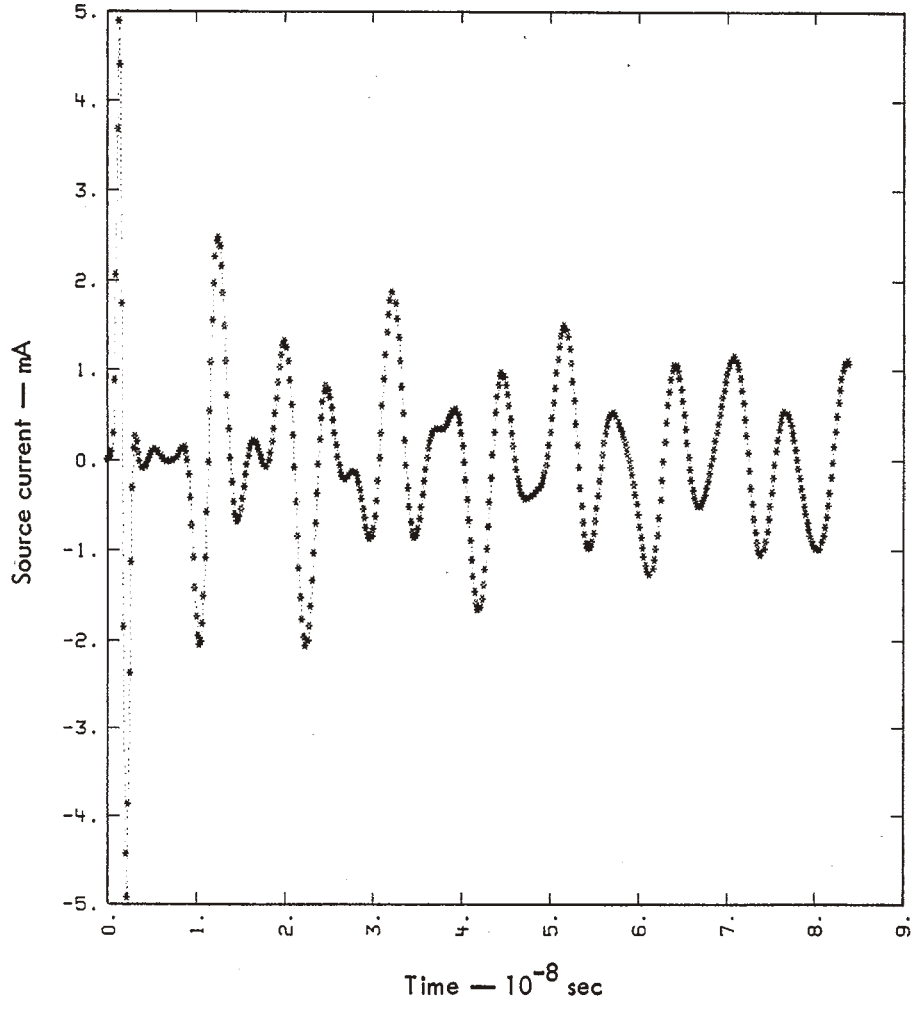

Fig. 2. Characteristics of a conical spiral antenna driven by the derivative of a gaussian voltage waveform.
(a) Driving-point current. (Continued on the following two pages.)

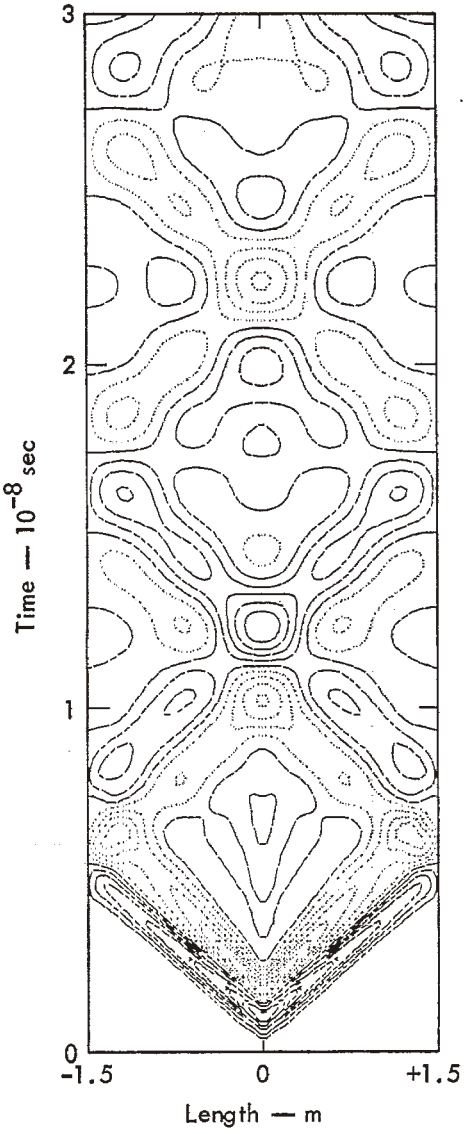

Fig. 2. (Continued.) (b) Space-time contours of constant current.

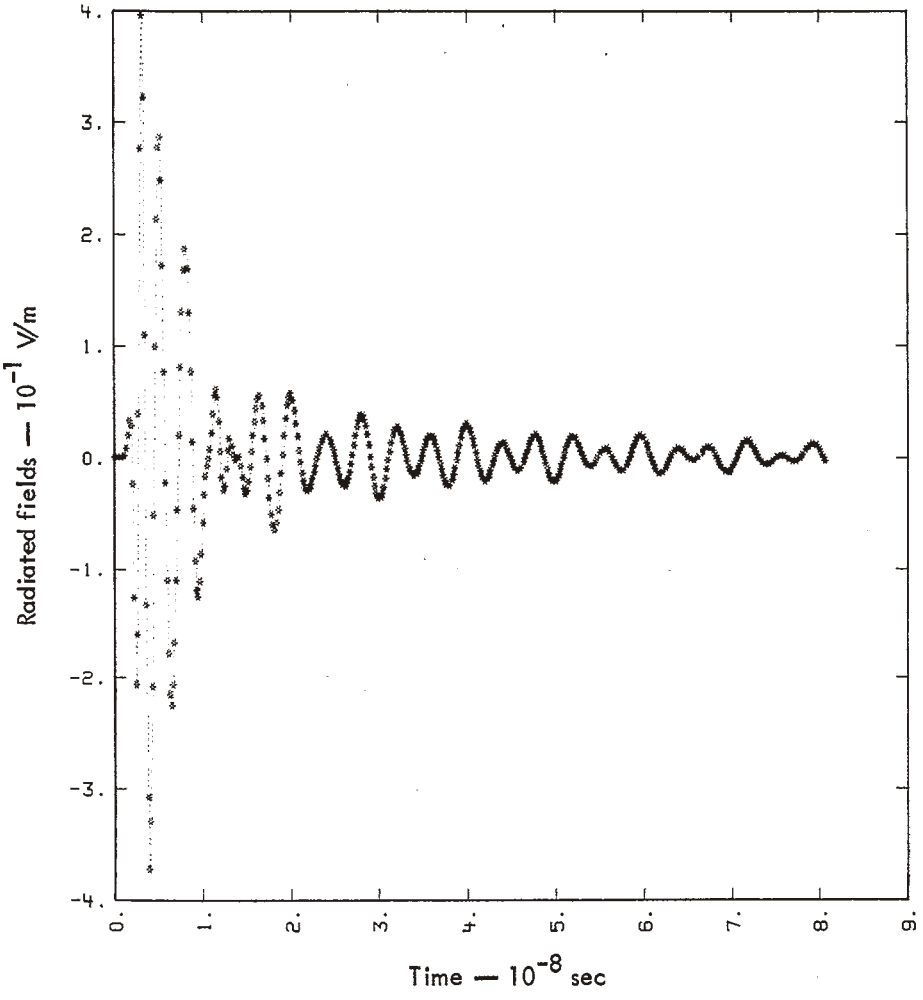

Fig. 2. (Continued.) (c) Radiated far field in boresight direction.

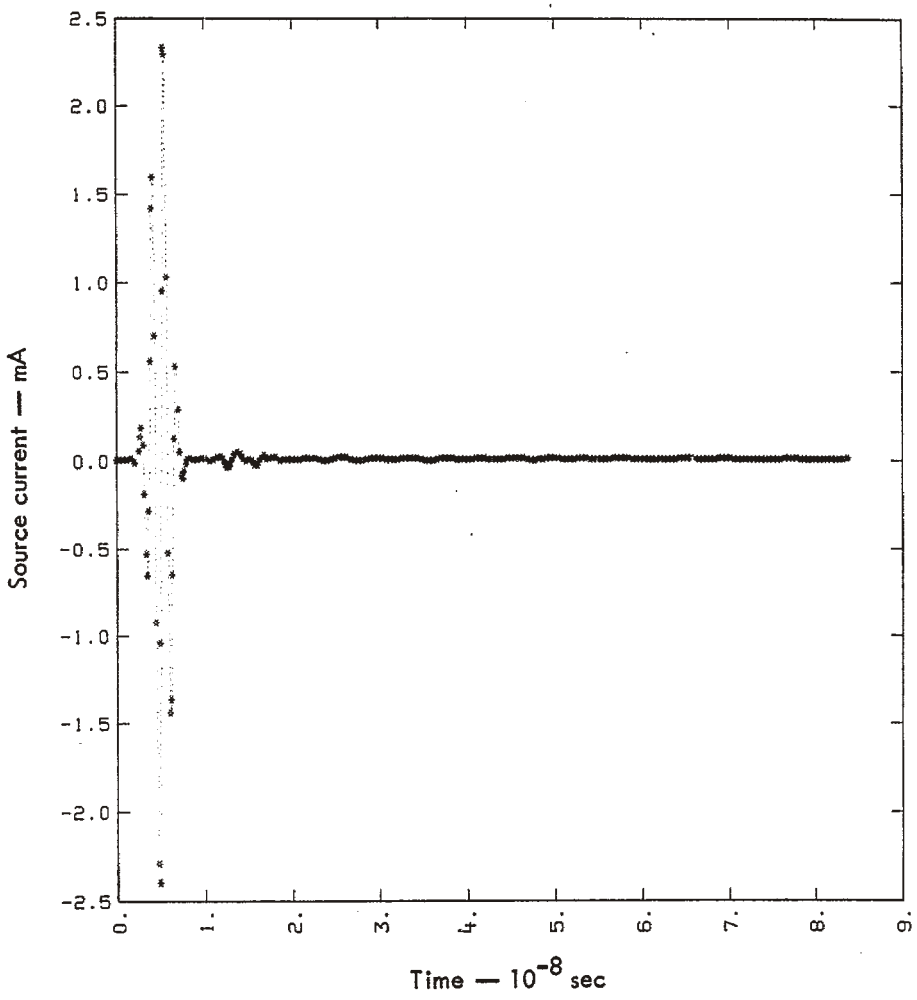

Fig. 3. Characteristics of a conical spiral antenna driven by a gaussian-envelope, sinusoidal-voltage waveform. (a) Driving-point current. (Continued on the following four pages.)

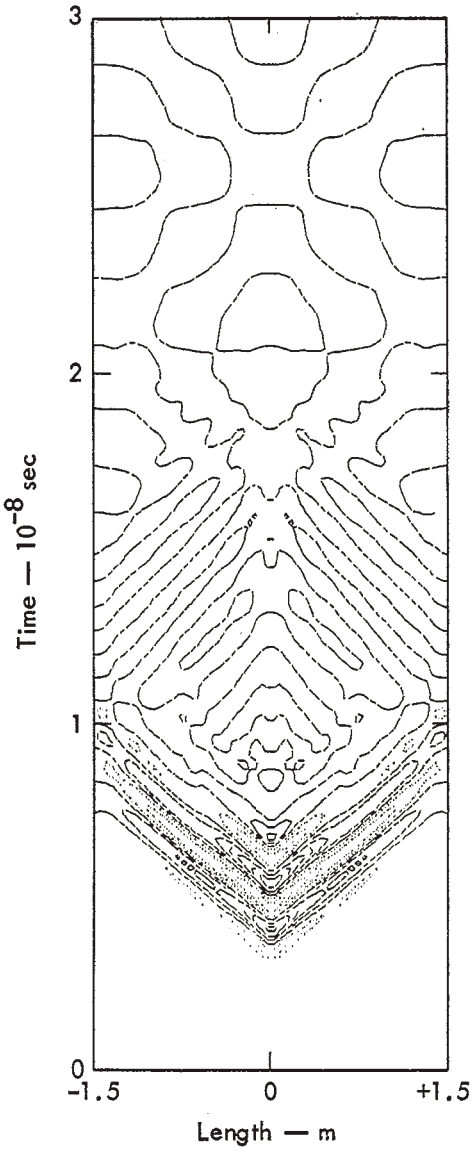

Fig. 3. (Continued.) (b) Space-time contours of constant current.

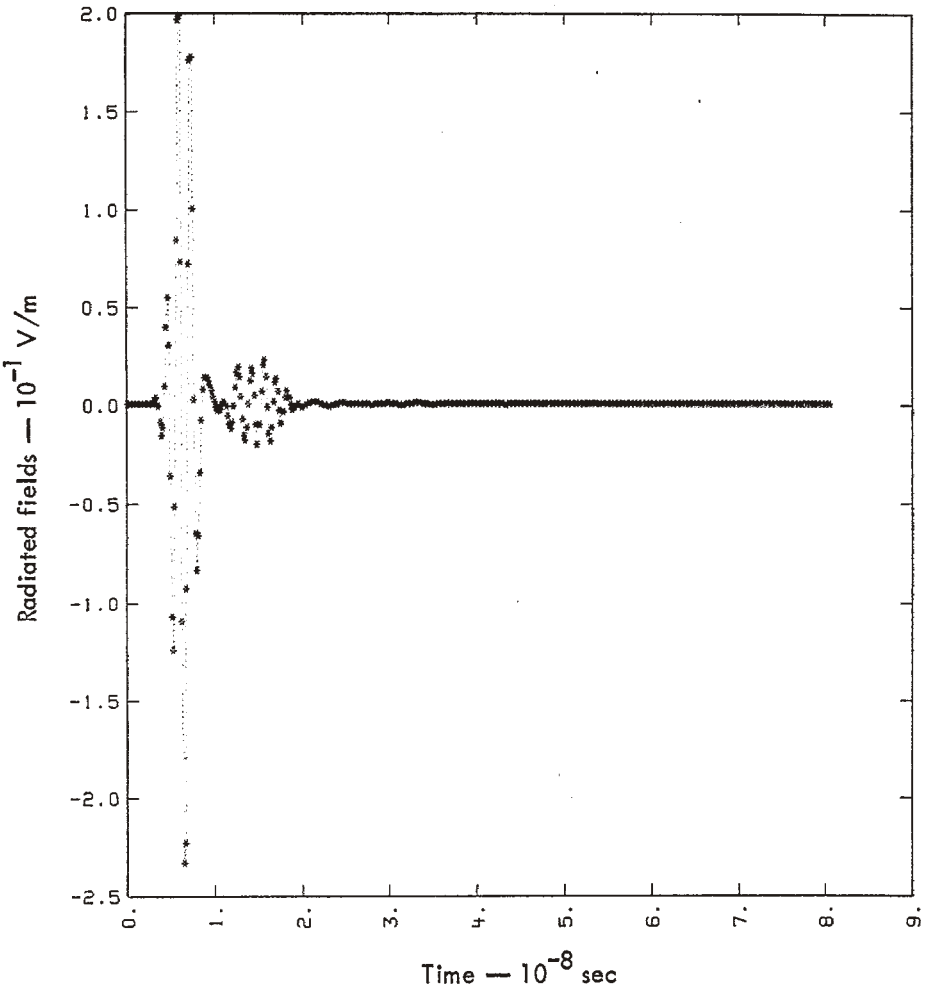

Fig. 3. (Continued.) (c) Radiated far field in the boresight direction.

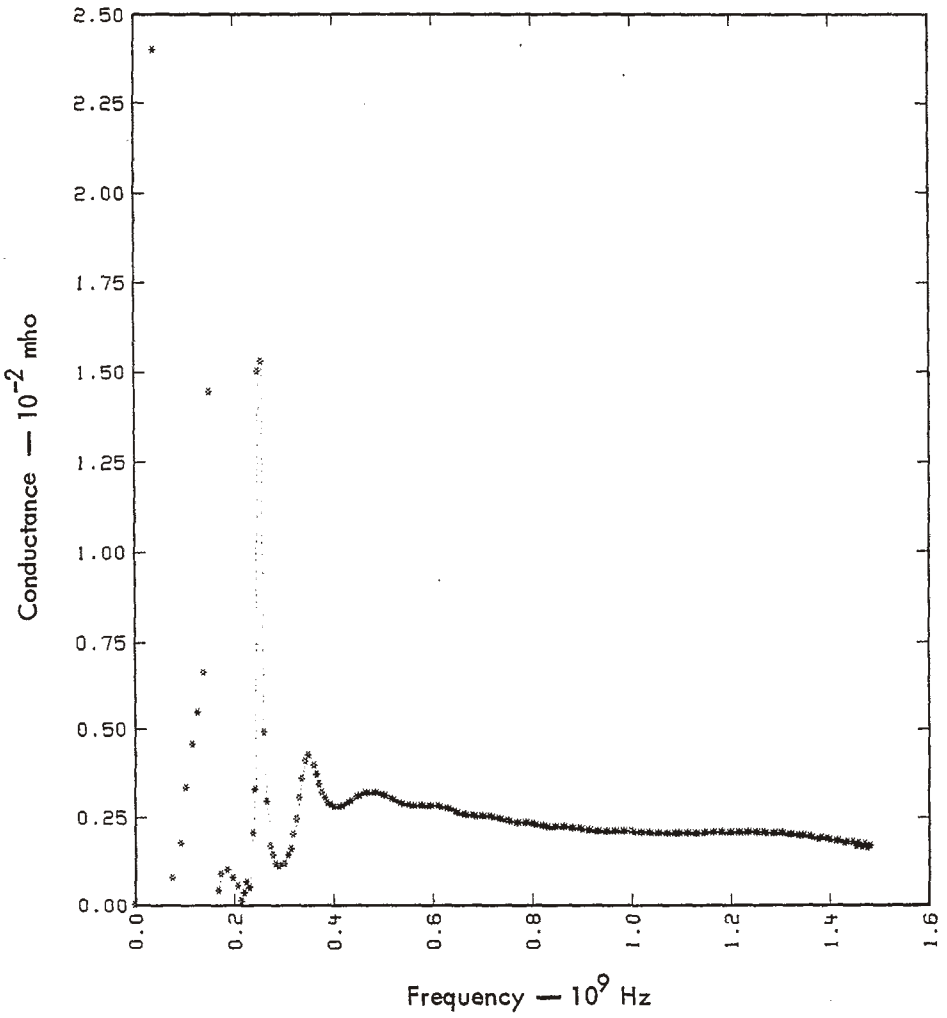

Fig. 3. (Continued.) (d) Real part of the antenna driving-point admittance.

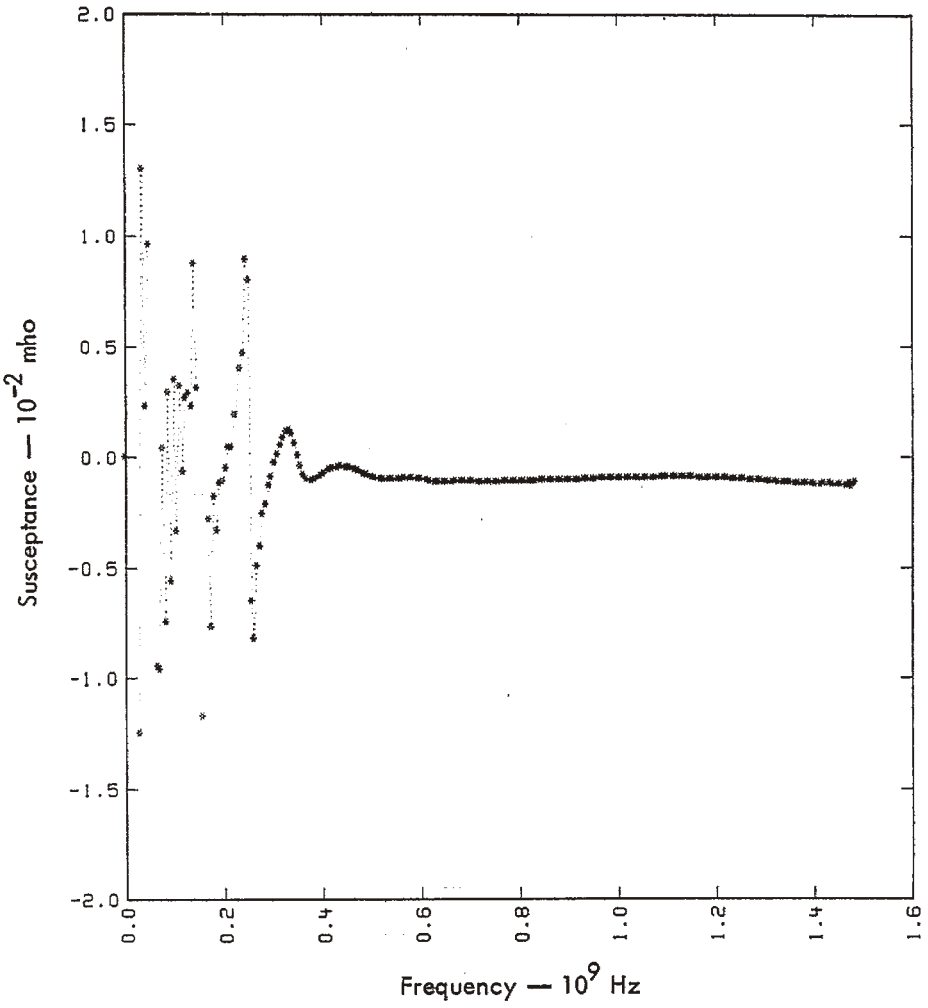

Fig. 3. (Continued.) (e) Imaginary part of the antenna driving-point admittance.

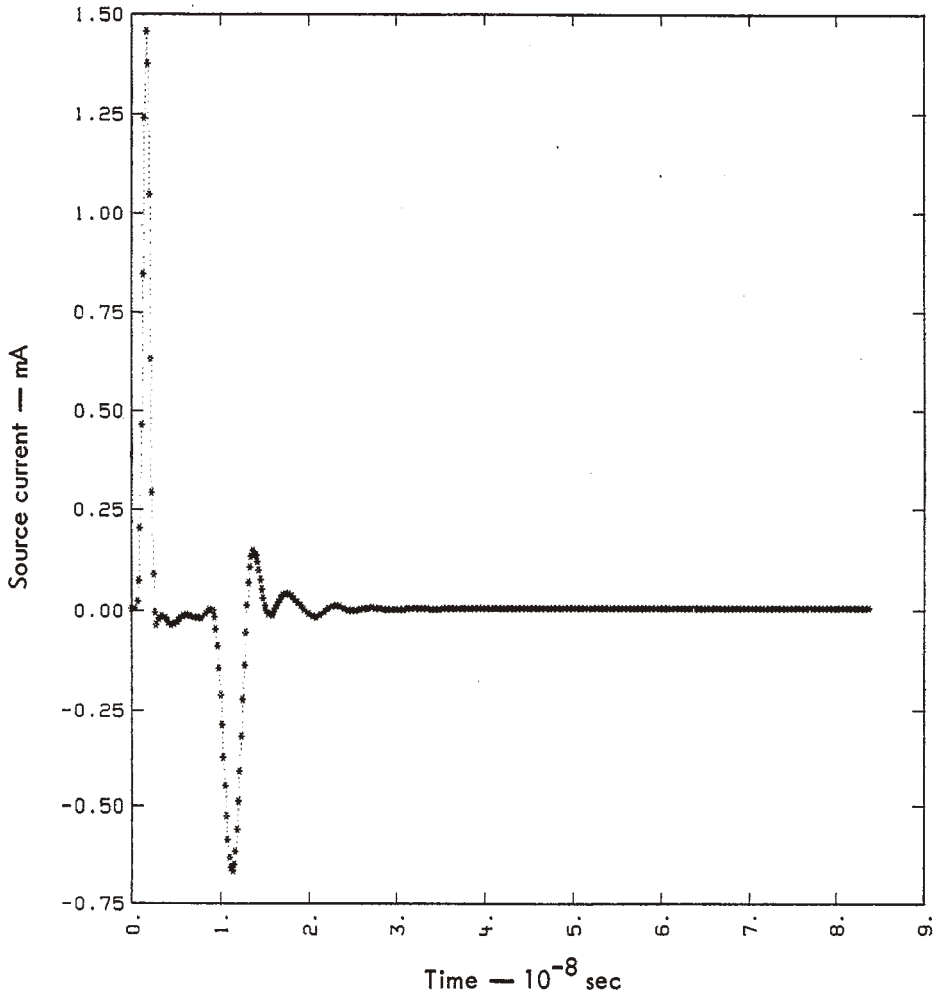

Fig. 4. Same as Fig. 1, except for a generator impedance of 350 Ω. (a) Driving-point current. (Continued on the following four pages.)

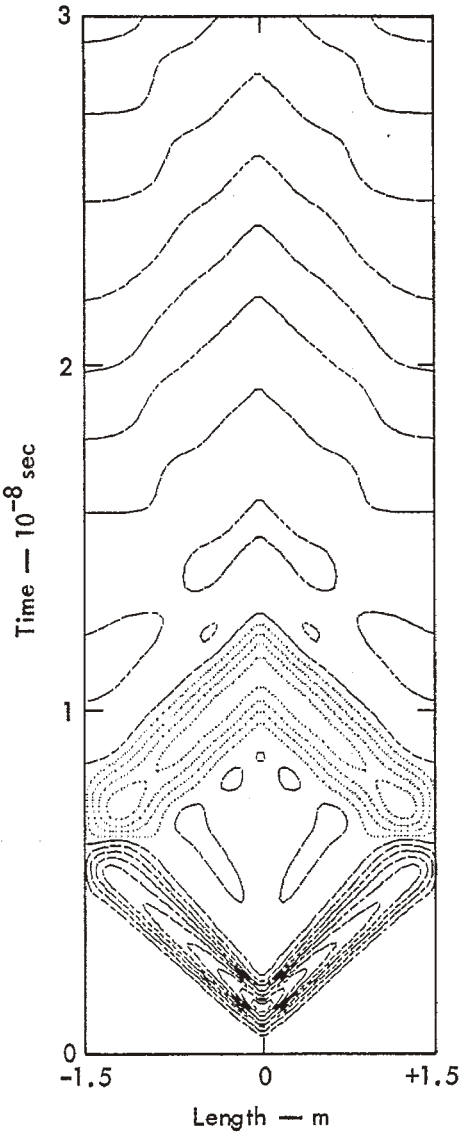

Fig. 4. (Continued.) (b) Space-time contours of constant current.

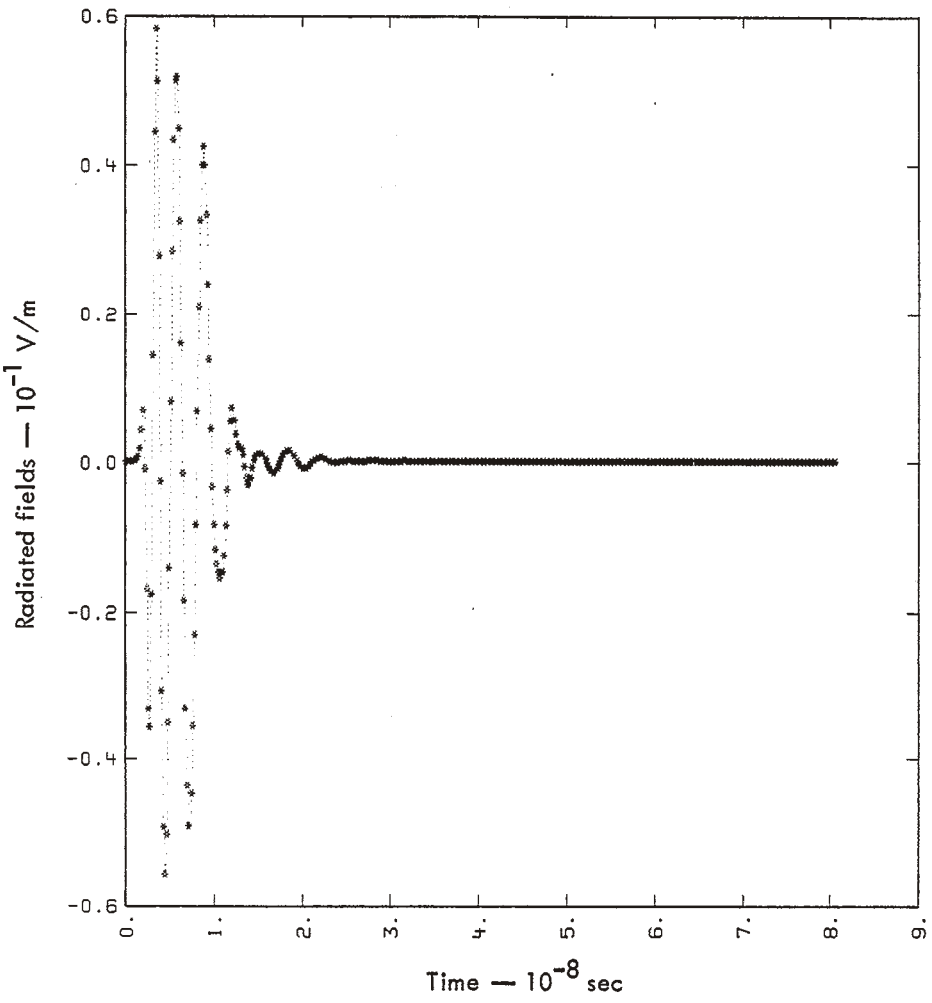

Fig. 4. (Continued.) (c) Radiated far field in the boresight direction.

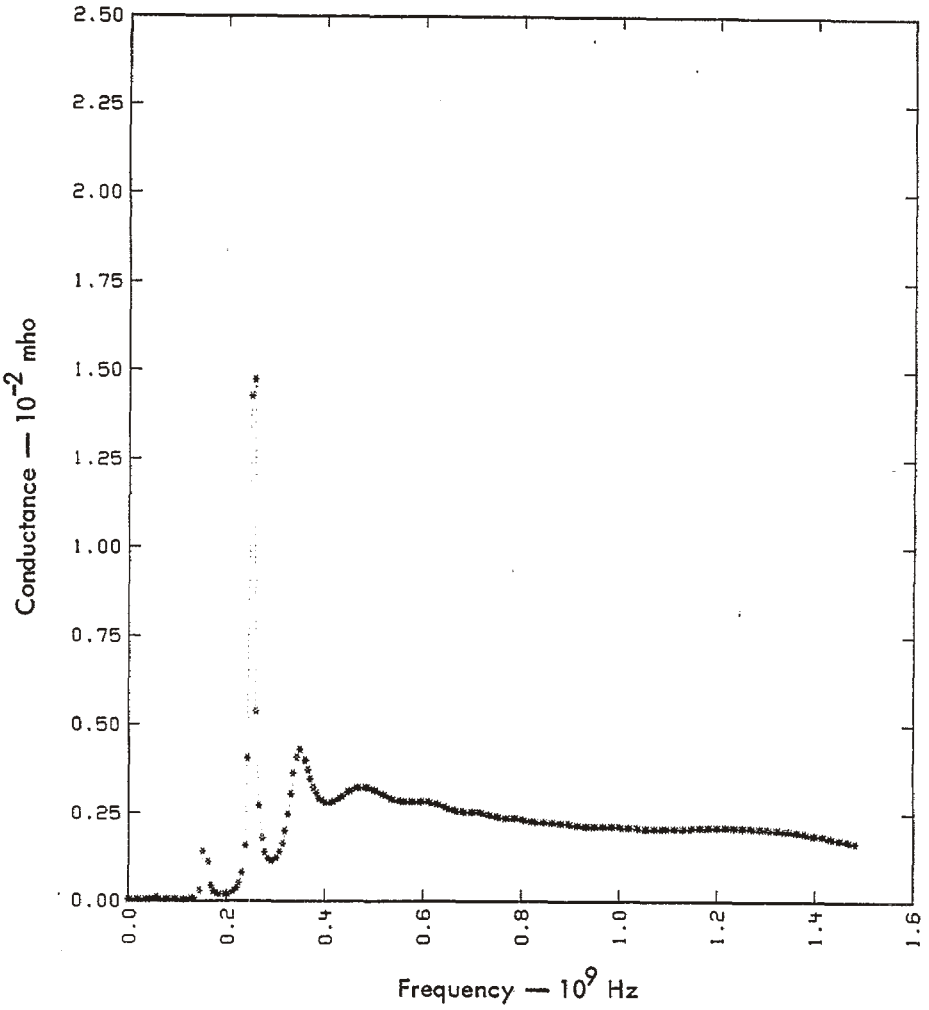

Fig. 4. (Continued.) (d) Real part of the antenna driving-point admittance.

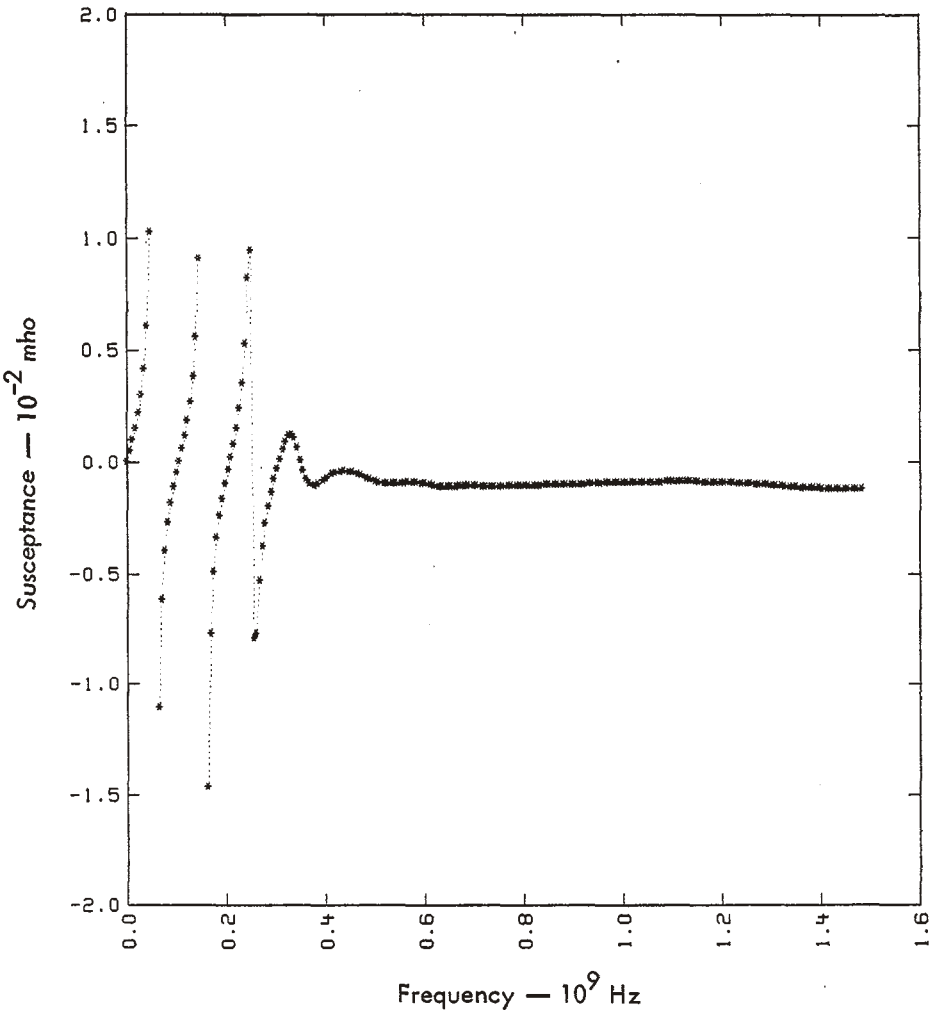

Fig. 4. (Continued.) (e) Imaginary part of the antenna driving-point admittance.

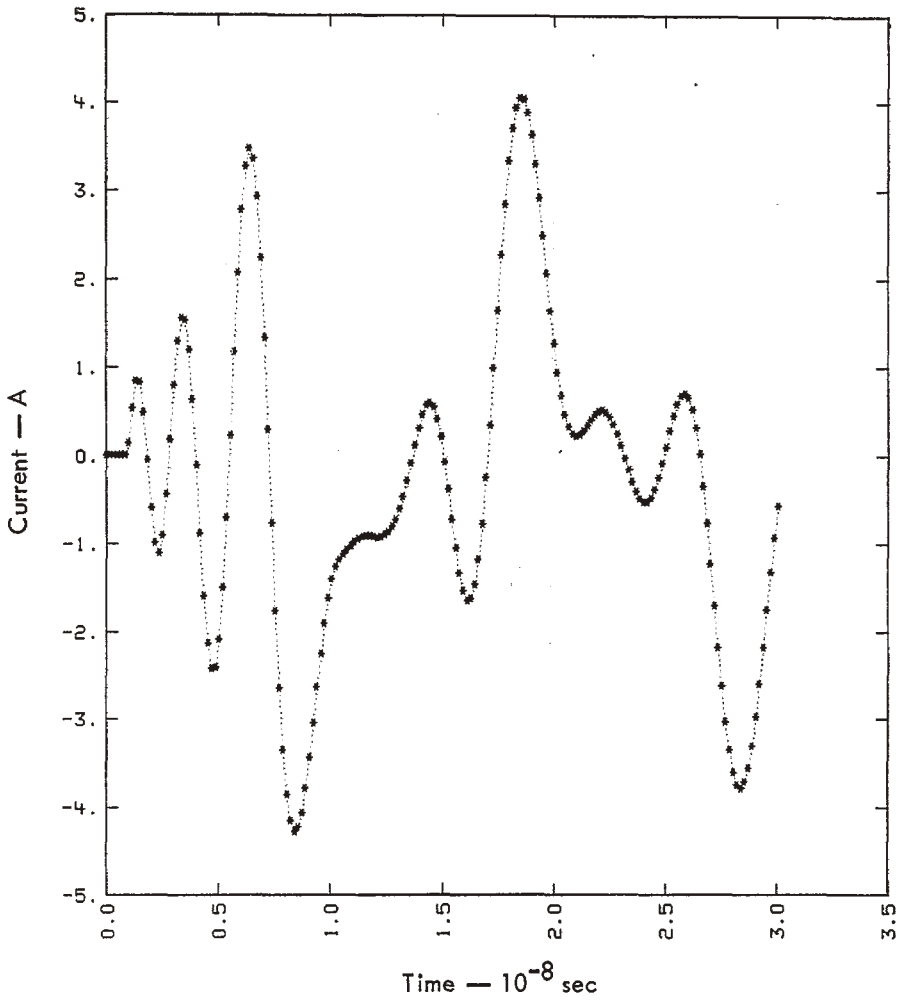

Fig. 5. EMP response of a conical spiral antenna. (a) Boresight illumination for a 0-Ω load. (Continued on the following two pages.)

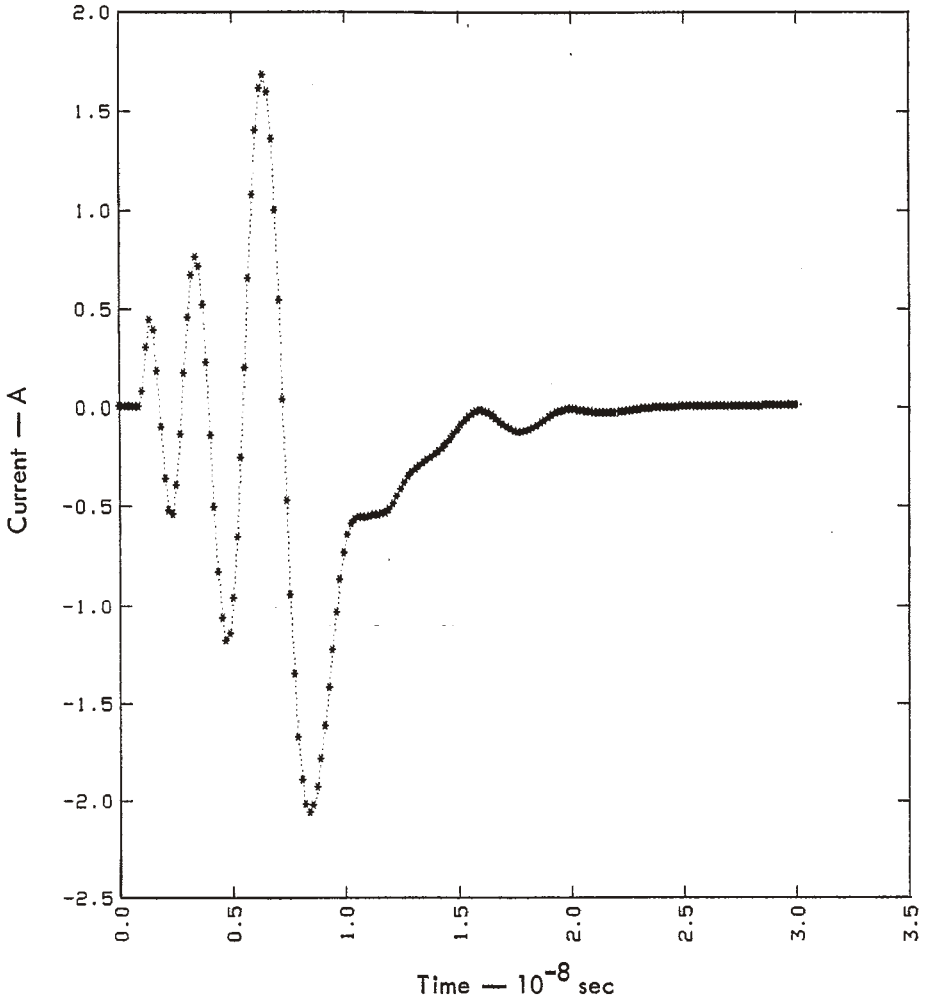

Fig. 5. (Continued.) (b) Boresight illumination for a 350-Ω load.

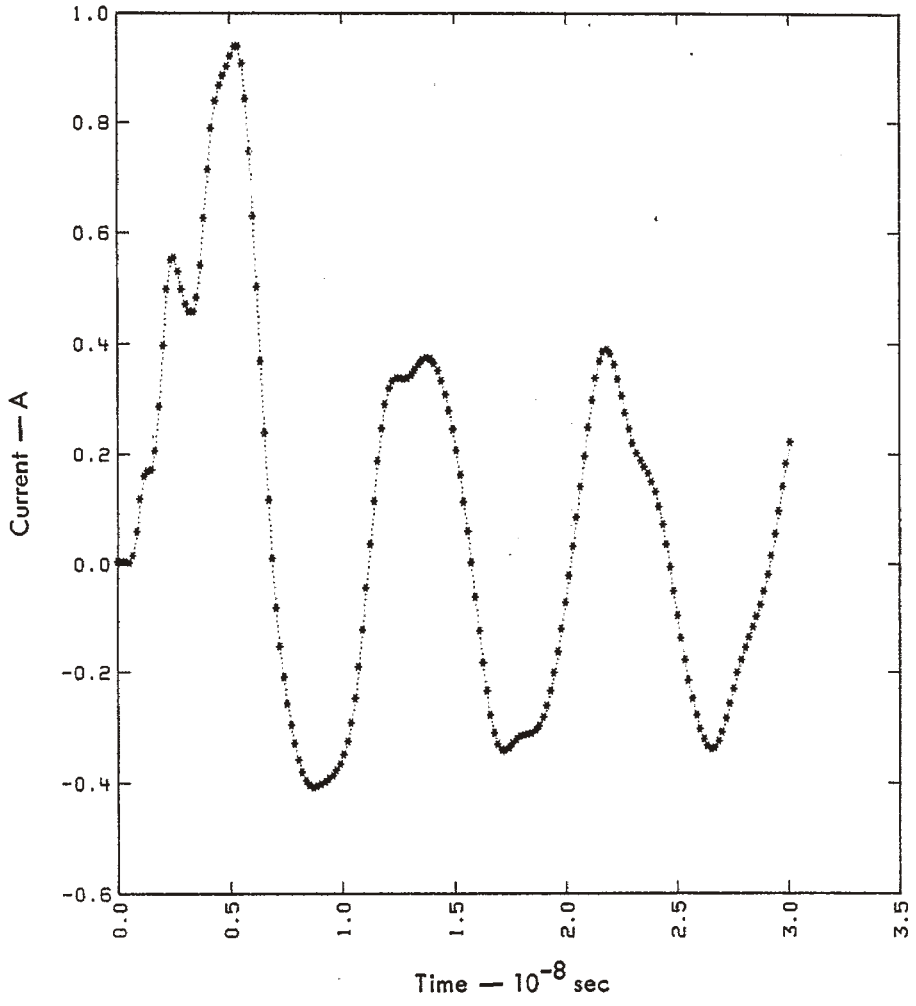

Fig. 5. (Continued.) (c) Off-axis illumination for a 350-Ω load.

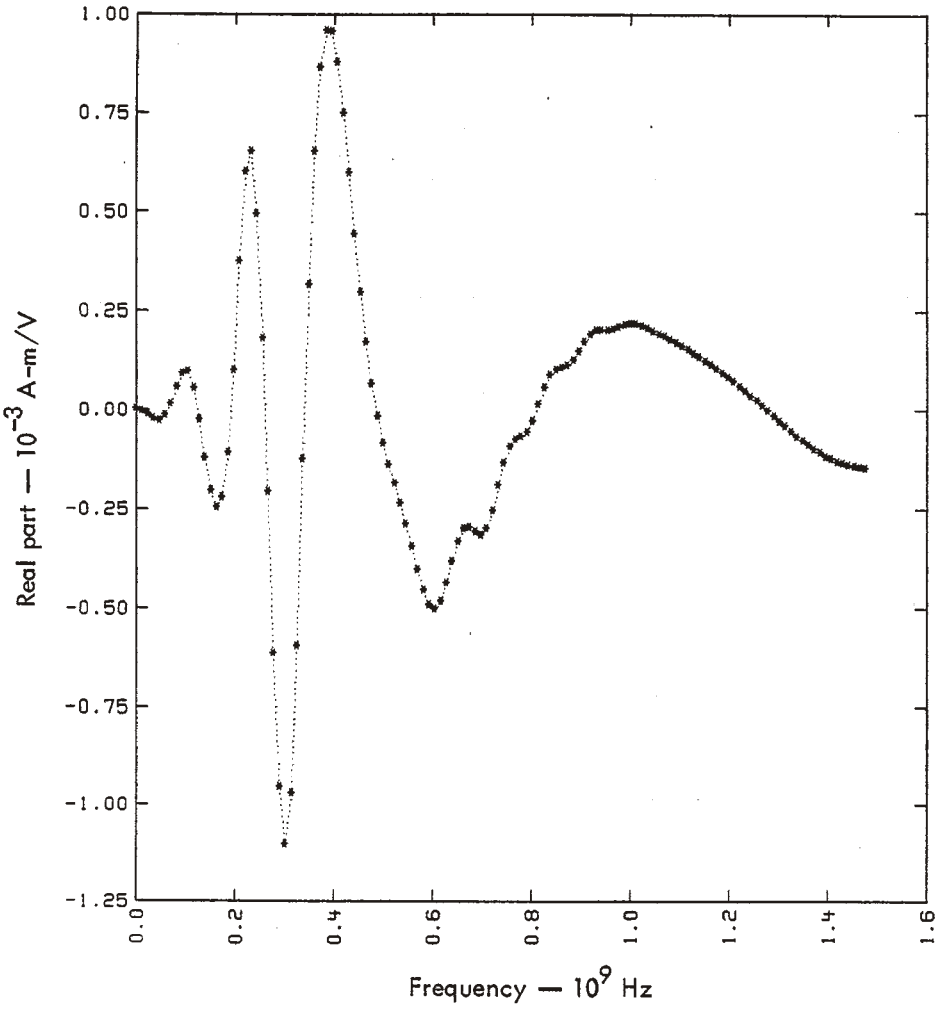

Fig. 6. Transfer admittance for the conditions of Fig. 5b. (a) Real part. (Continued on the following three pages.)

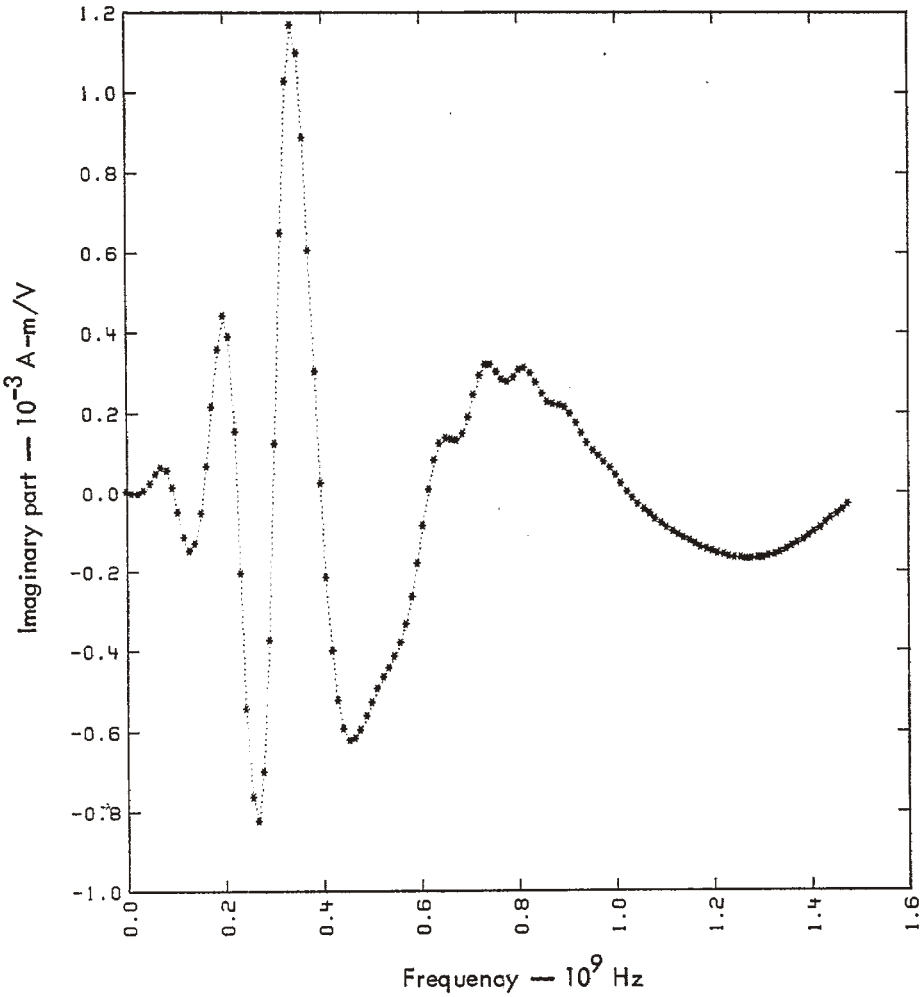

Fig. 6. (Continued.) (b) Imaginary part.

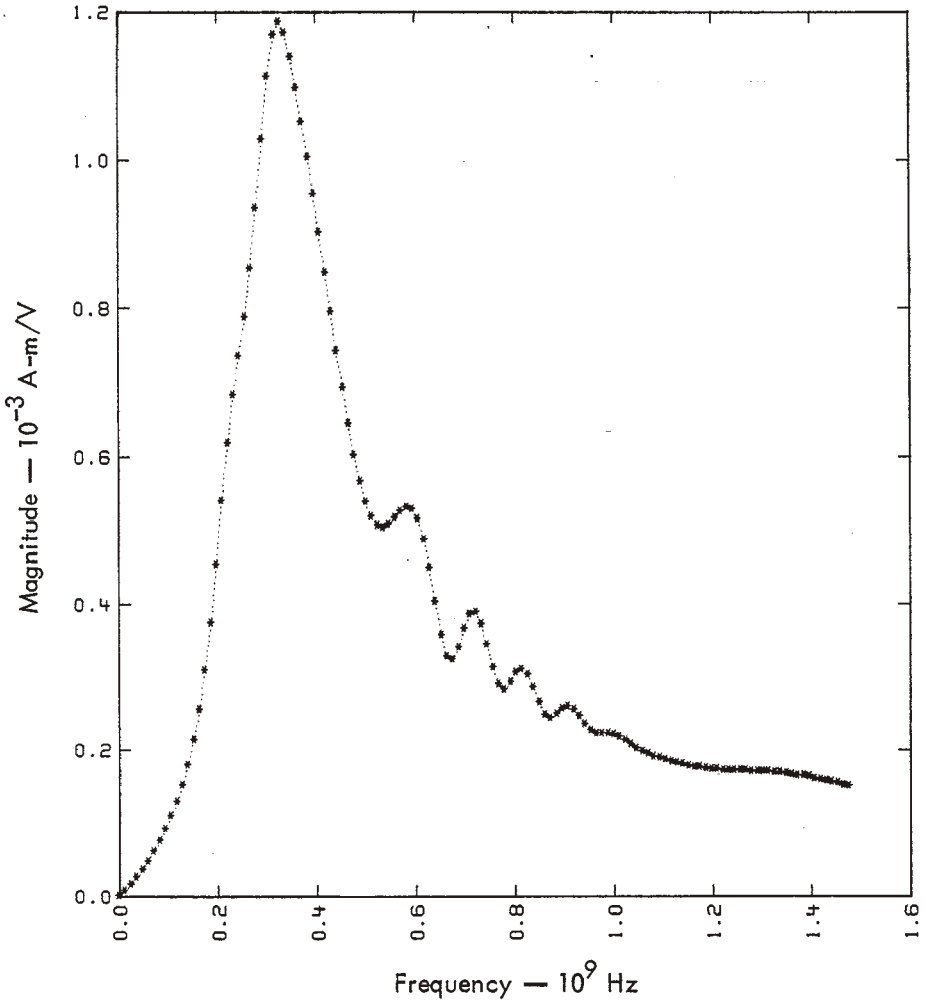

Fig. 6. (Continued.) (c) Magnitude.

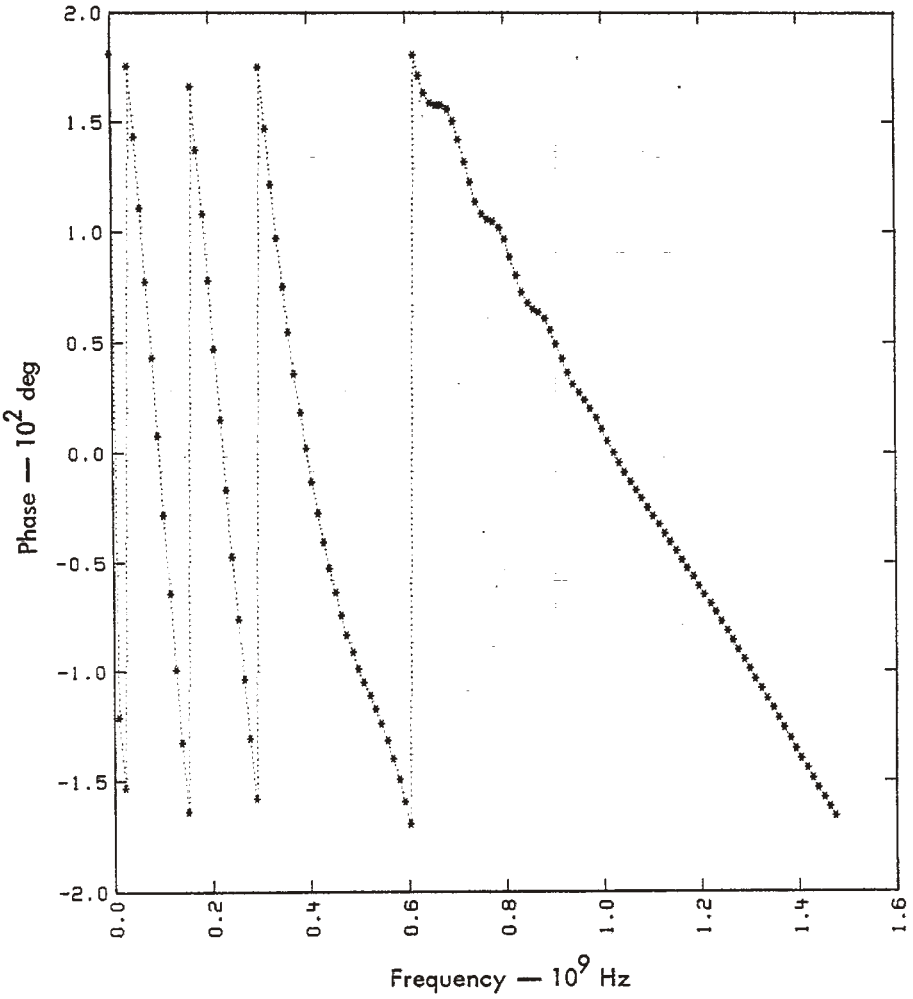

Fig. 6. (Continued.) (d) Phase.

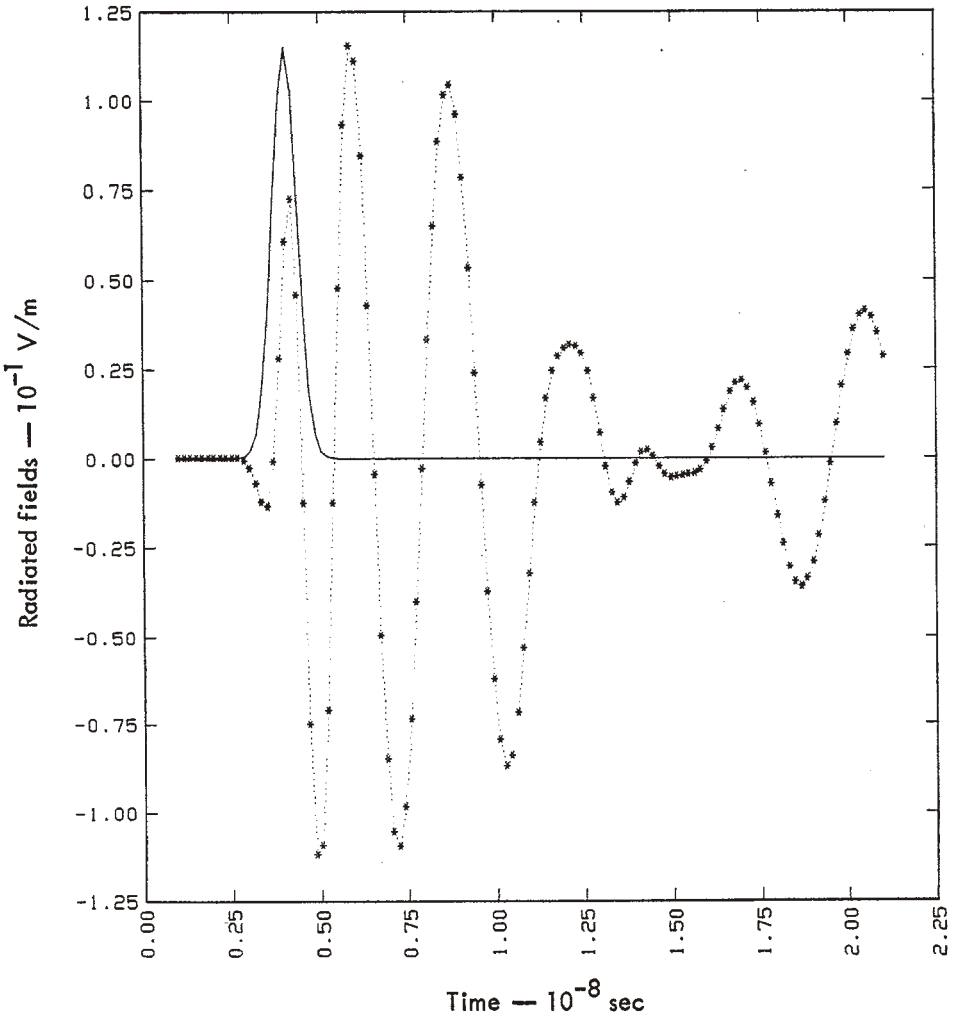

Fig. 7. Driving-point voltages and radiated far fields in the boresight direction. The applied voltages are listed in parts (a) through (e). (a) Gaussian. (Continued on the following four pages.)

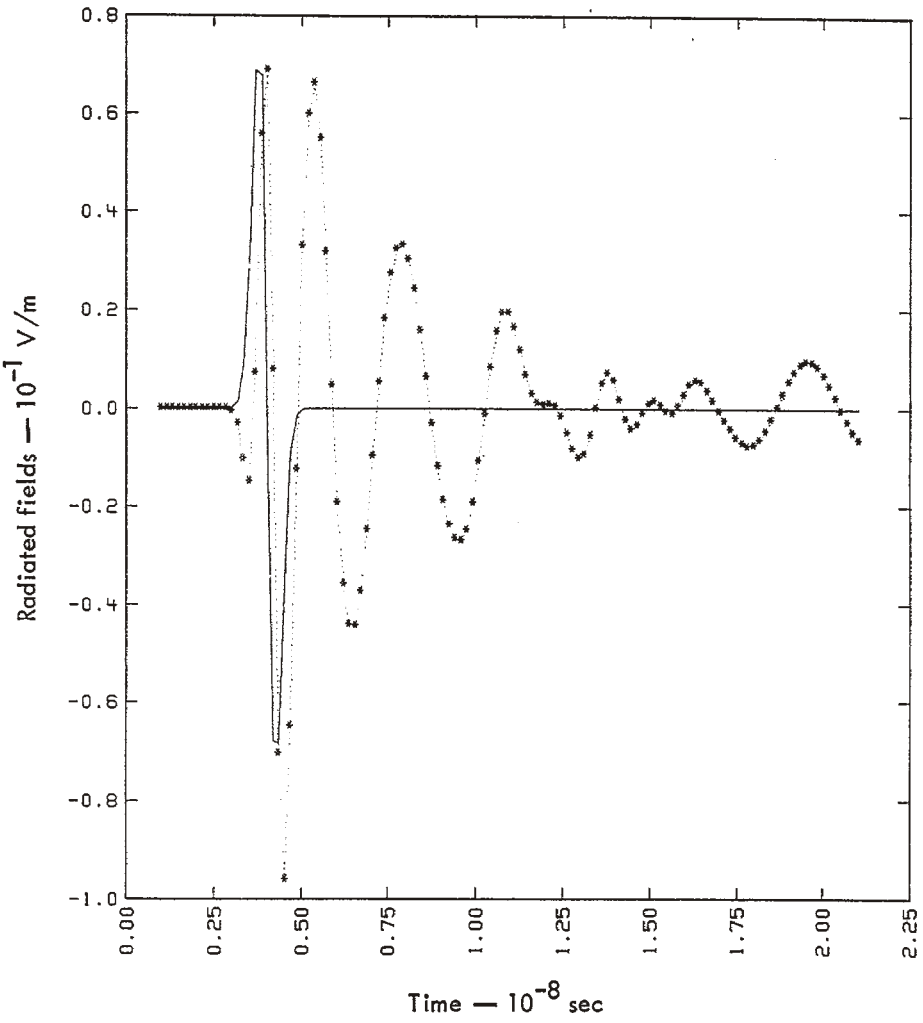

Fig. 7. (Continued.) (b) First derivative of a gaussian.

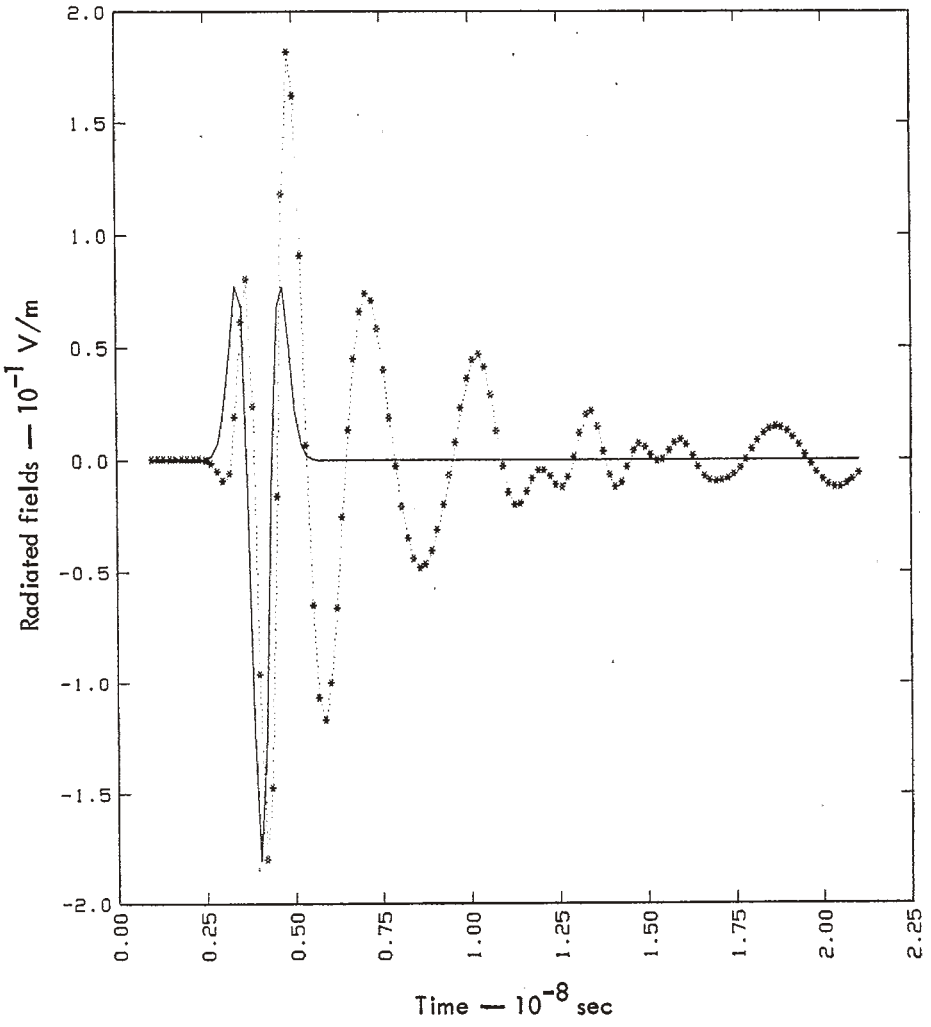

Fig. 7. (Continued.) (c) Second derivative of a gaussian.

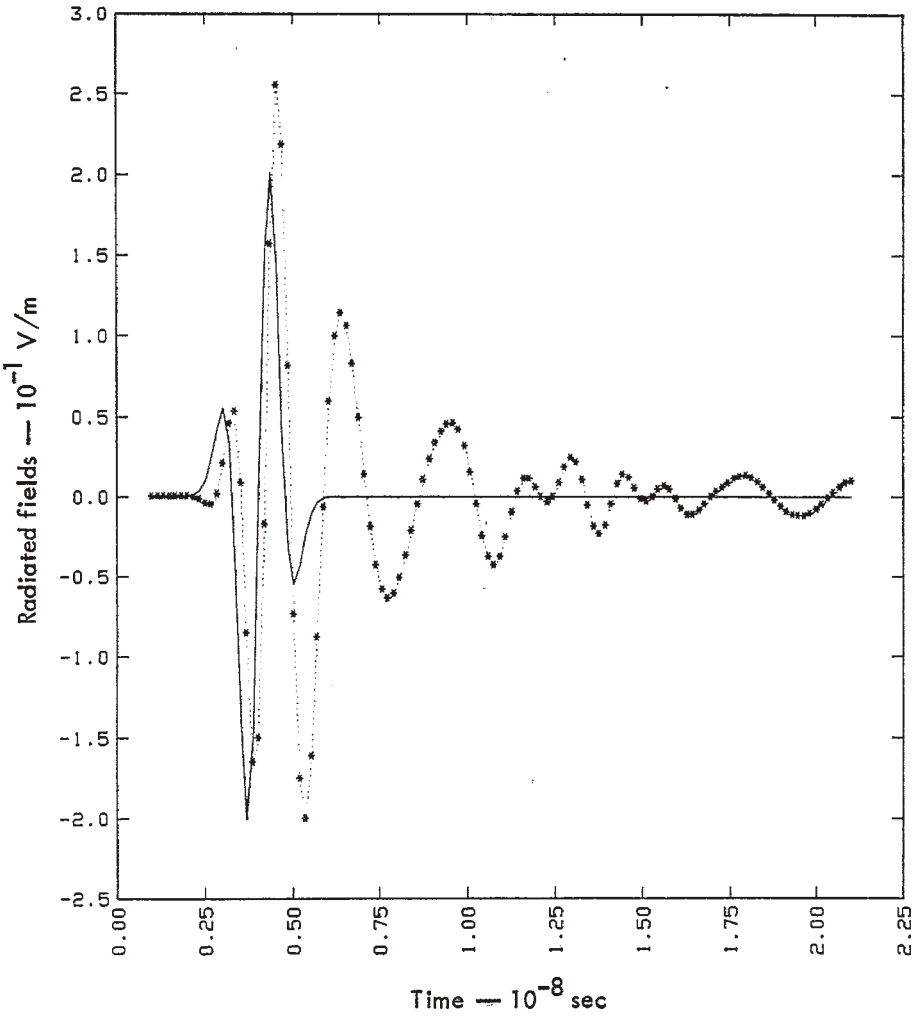

Fig. 7. (Continued.) (d) Third derivative of a gaussian.

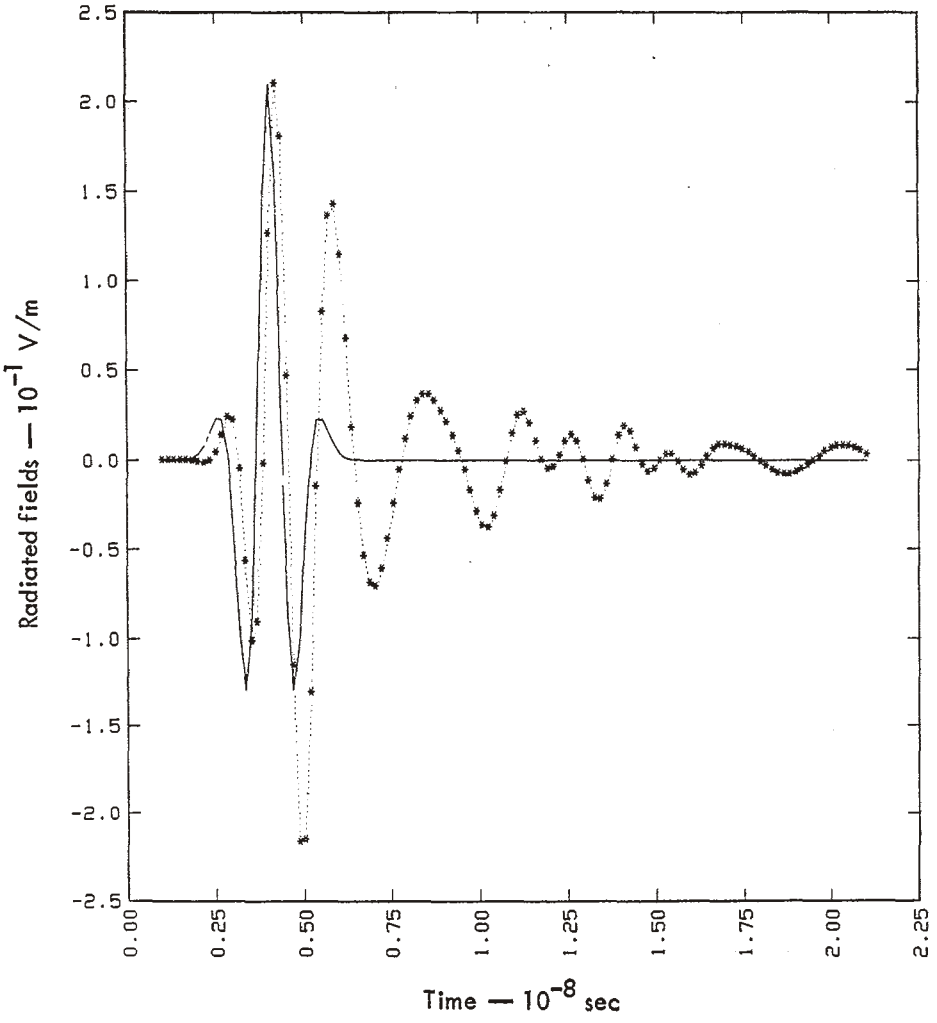

Fig. 7. (Continued.) (e) Fourth derivative of a gaussian.

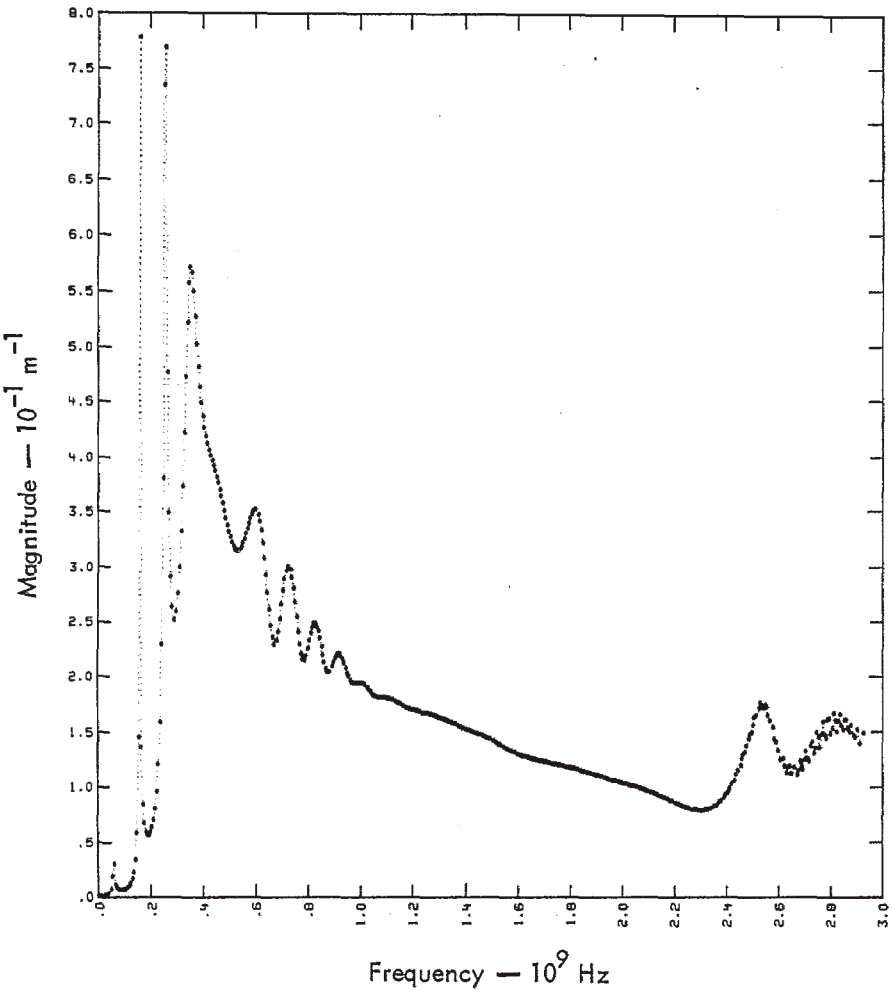

Fig. 8. Steps required for obtaining the third derivative of a gaussian waveform for the radiated far field. (a) Magnitude of the transfer function relating the radiated far field to the driving-point voltage. (Continued on the following three pages.)

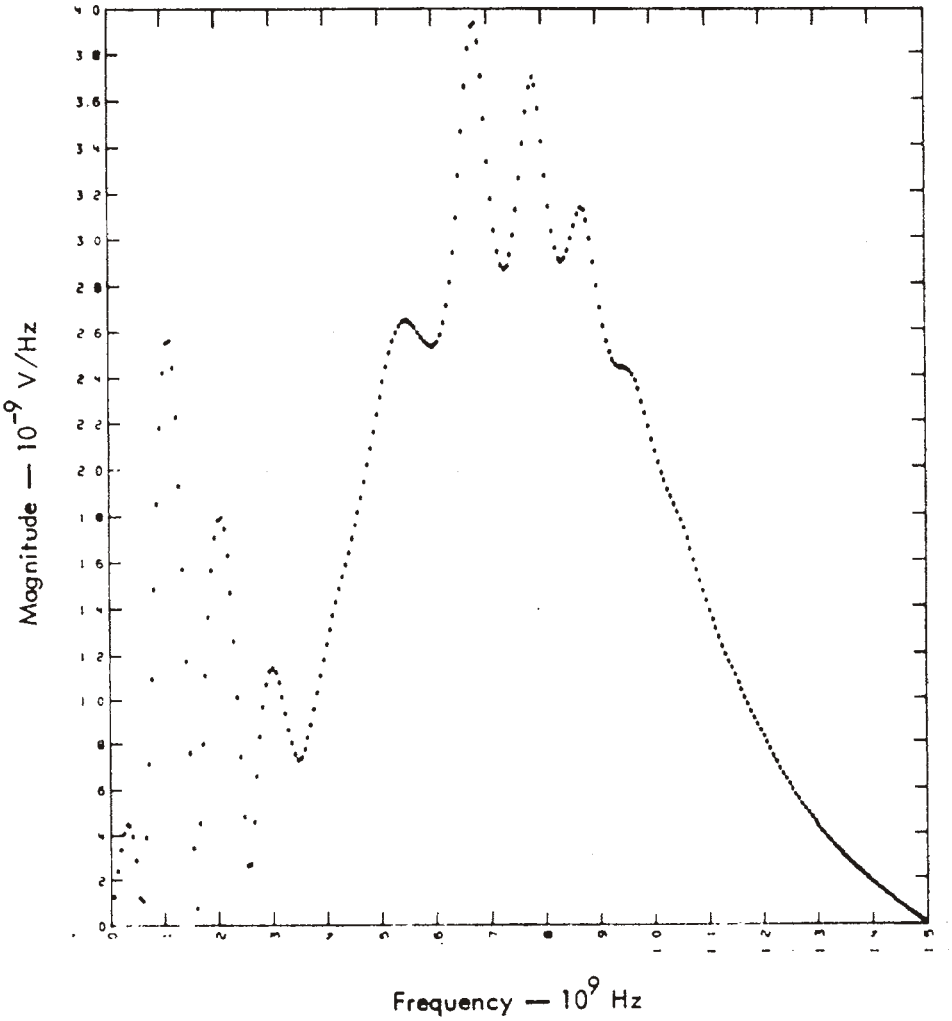

Fig. 8. (Continued.) (b) Spectrum of the third derivative of the gaussian waveform divided by the transfer function of (a).

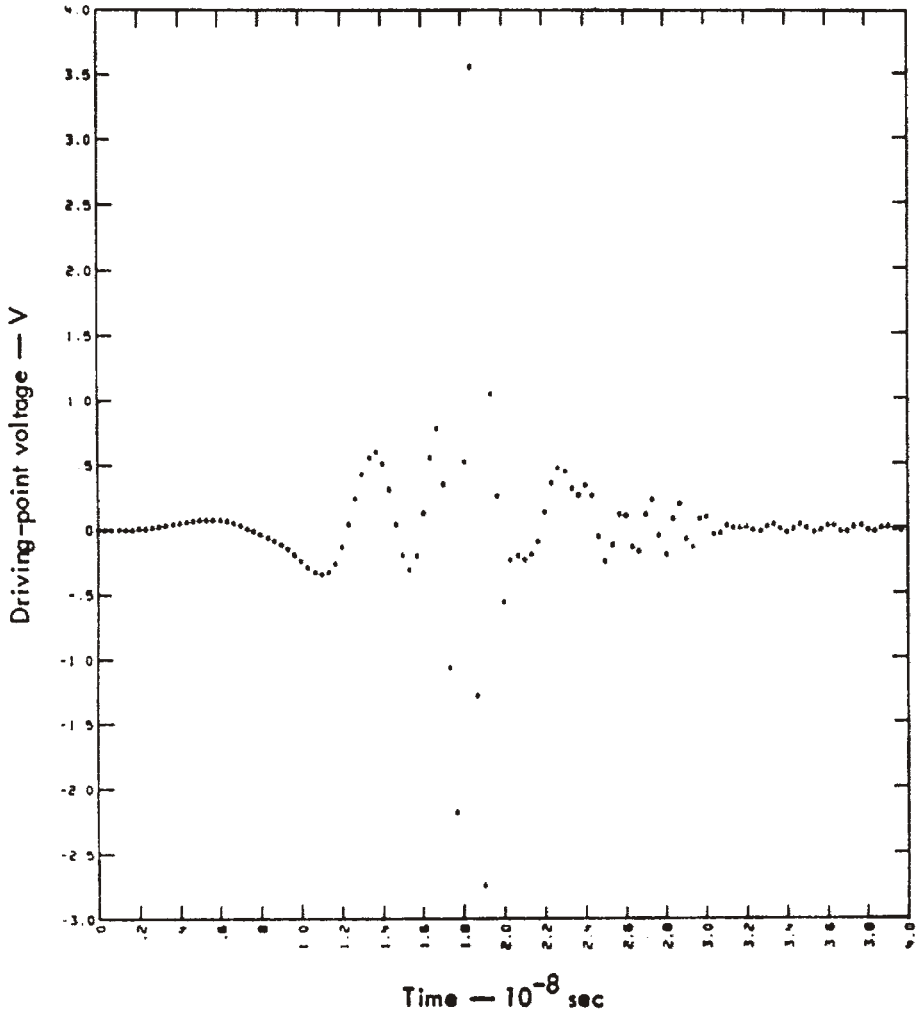

Fig. 8. (Continued.) (c) The inverse Fourier transform of the spectrum of (b).

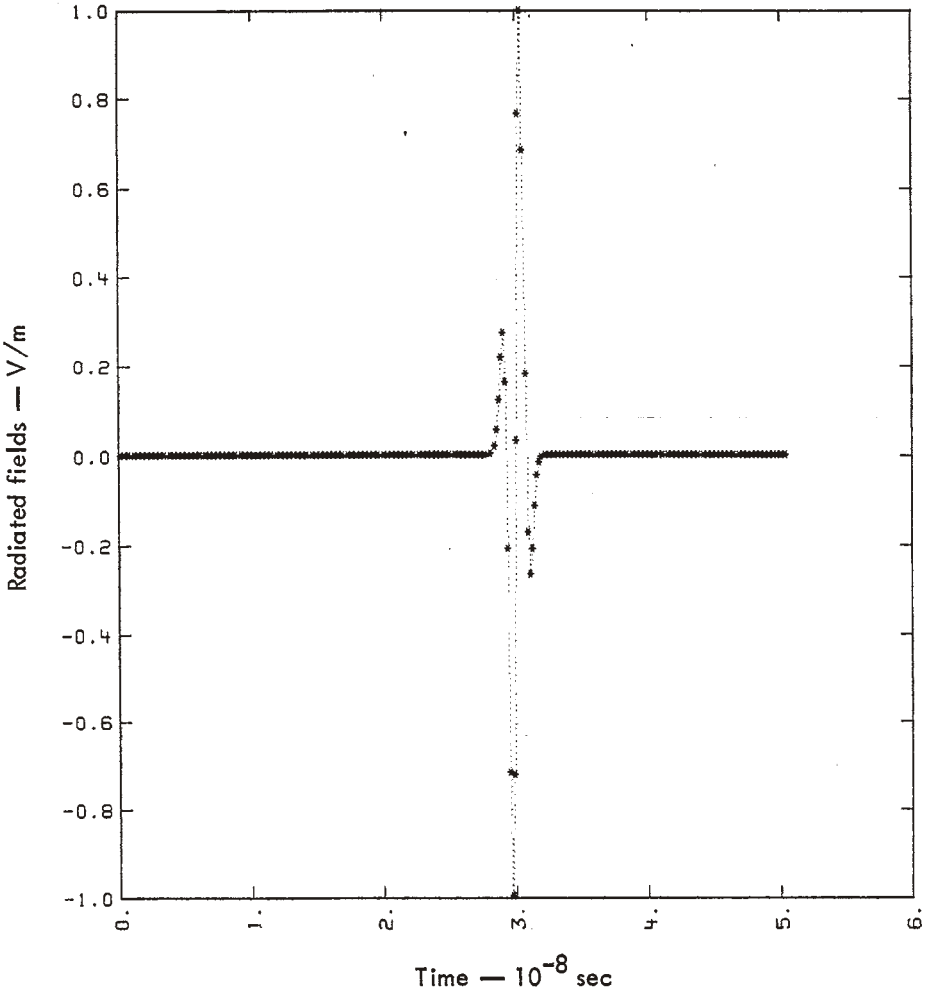

Fig. 8. (Continued.) (d) The resulting radiated far field using the waveform of (c) and the integral-equation solution procedure.

ACKNOWLEDGMENT

This research was sponsored by the Defense Nuclear Agency under Subtask R99QAXEB075, Work Unit 35: Communications, Antennas, and Transmission Lines.

REFERENCES

1. J.D. Dyson, "The Unidirectional Equiangular Spiral Antenna," IRE Trans. Antennas and Propagation AP-7, 329 (1959).
2. R. Mittra and D.W. Klock, "A Theoretical Study of the Conical Spiral Antenna," Department of Electrical Engineering, University of Illinois, Urbanna, Tech. Rept. AFAC-TR-66-114 (1966).
3. Y.S. Yeh and K.K. Mei, "Theory of Conical Equiangular-Spiral Antennas. Part I — Numerical Technique," IEEE Trans. Antennas and Propagation AP-15, 634 (1967).
4. Y.S. Yeh and K.K. Mei, "Theory of Conical Equiangular Spiral Antennas. Part II — Current Distributions and Input Impedances," IEEE Trans. Antennas and Propagation AP-16, 14 (1968).
5. R. Mittra, Ed., Computer Techniques for Electromagnetics (Pergamon Press, New York, 1973).
6. E.K. Miller, A.J. Poggio, and G.J. Burke, "An Integro-Differential Equation Technique for the Time-Domain Analysis of Thin Wire Structures, Part I — The Numerical Method," J. Computational Phys. 12, 24 (1973).
7. A.J. Poggio, E.K. Miller, and G.J. Burke, "An Integro-Differential Equation Technique for the Time-Domain Analysis of Thin Wire Structures, Part II — Numerical Results," J. Computation Phys. 12, 210 (1973).
8. E.K. Miller, "Some Computational Aspects of Transient Electromagnetics," Lawrence Livermore Laboratory, Interaction Note 143, September 1972.
9. C.L. Bennett and W.L. Weeks, "A Technique for Computing Approximate Electromagnetic Impulse Response of Conducting Bodies," Purdue University, Rept. TR-EE-68-11 (1968).
10. E.K. Miller and M.L. Van Blaricum, "The Short-Pulse Response of a Straight Wire," IEEE Trans. Antennas and Propagation AP-21, 396 (1973).

APPENDIX A
A PARAMETER STUDY OF THE CONICAL SPIRAL ANTENNA

The equation of a conical spiral is

$$r = r_0 e^{A\phi} \tag{1}$$

where r is the radial distance from the apex of the cone and ϕ is an angle in a normal cylindrical coordinate system. In this equation,

$$A = a \sin \theta_0 \tag{2}$$

where A is called the "slowing ratio" and θ_0 is the cone half-angle.

The angle made by the spiral with a line on the cone originating from the apex of the cone is

$$\alpha = \cot^{-1} a \tag{3}$$

The relationship between the arc length, L, and the angle ϕ is

$$\phi = \frac{1}{A} \ln \left[\frac{L}{r_0 \sqrt{1 + \frac{\sin^2 \theta_0}{A^2}}} + 1 \right] \tag{4}$$

The wire radius can be determined by Eq. (6) of Ref. 3:

$$R = \frac{\delta A \sin \alpha}{2} r$$

For the present study, we have used wire of constant radius determined at $r = r_0$, and $\delta = 45$. This yields an input impedance of 200 to 250 Ω using Fig. 9 of Ref. 3. Table A1 summarizes the parameters for the data plotted in Figs. A1 through A12.

Table A1. Antenna parameters for Figs. A1 through A12.

Figure No.	δ (deg)	θ_0 (deg)	α (deg)	L (m)	r_0 (m)
A1	45	5	60	3	0.05
A2	45	10	60	3	0.05
A3	45	15	60	3	0.05
A4	45	20	60	3	0.05
A5	45	5	70	3	0.05
A6	45	10	70	3	0.05
A7	45	15	70	3	0.05
A8	45	20	70	3	0.05
A9	45	5	80	3	0.05
A10	45	10	80	3	0.05
A11	45	15	80	3	0.05
A12	45	20	80	3	0.05

The antenna input admittance and a transfer admittance for each of these antennas are plotted in Figs. A1 through A12. In each figure, part (a) is the real part of the input impedance, part (b) is the imaginary part of the input impedance, part (c) is a Smith chart showing the input impedance normalized to 300 Ω, part (d) is the magnitude of the transfer admittance, and part (e) is the phase of the transfer admittance. This transfer admittance relates the current driven through a 240-Ω resistive load to an incident field of 1 V/m with the electric field parallel to the source region segments and incident from the boresight direction.

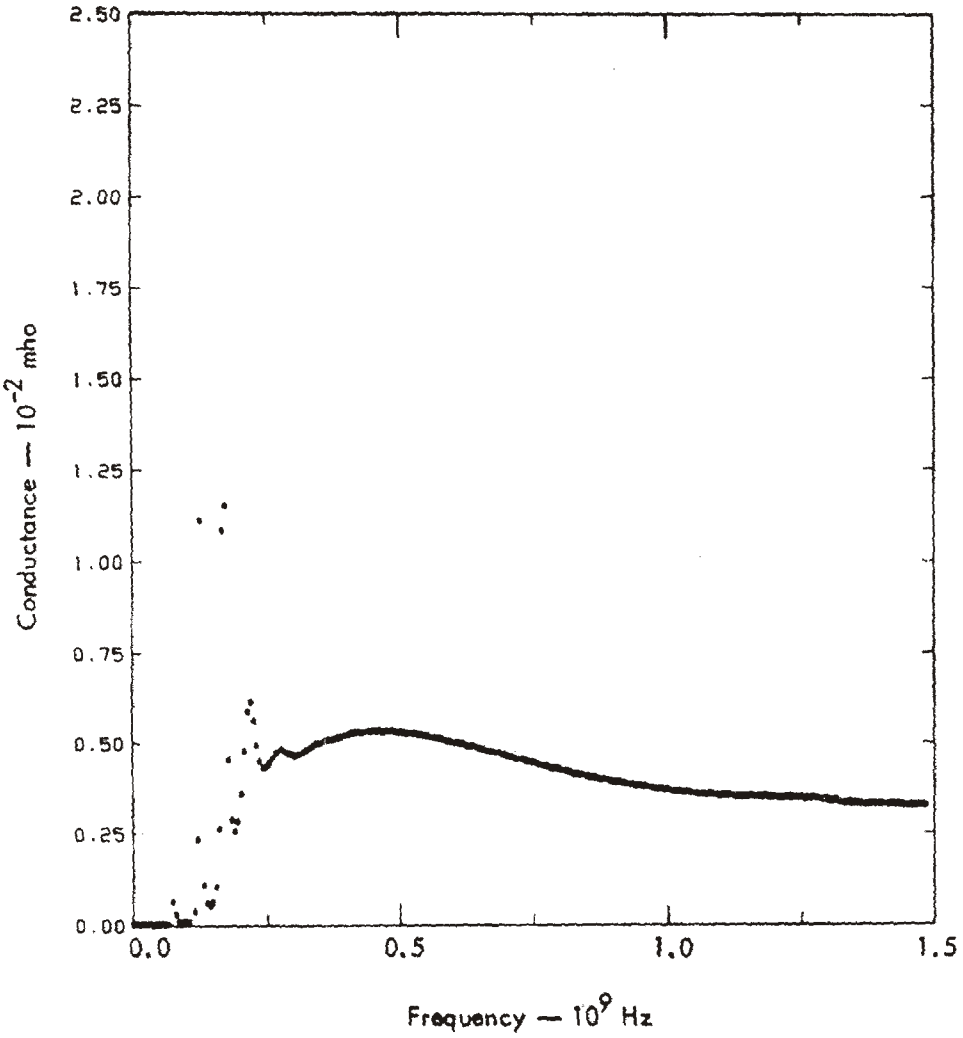

Fig. A1. Antenna characteristics for antenna A1 in Table A1.
(a) Real part of the driving-point admittance.
(Continued on the following four pages.)

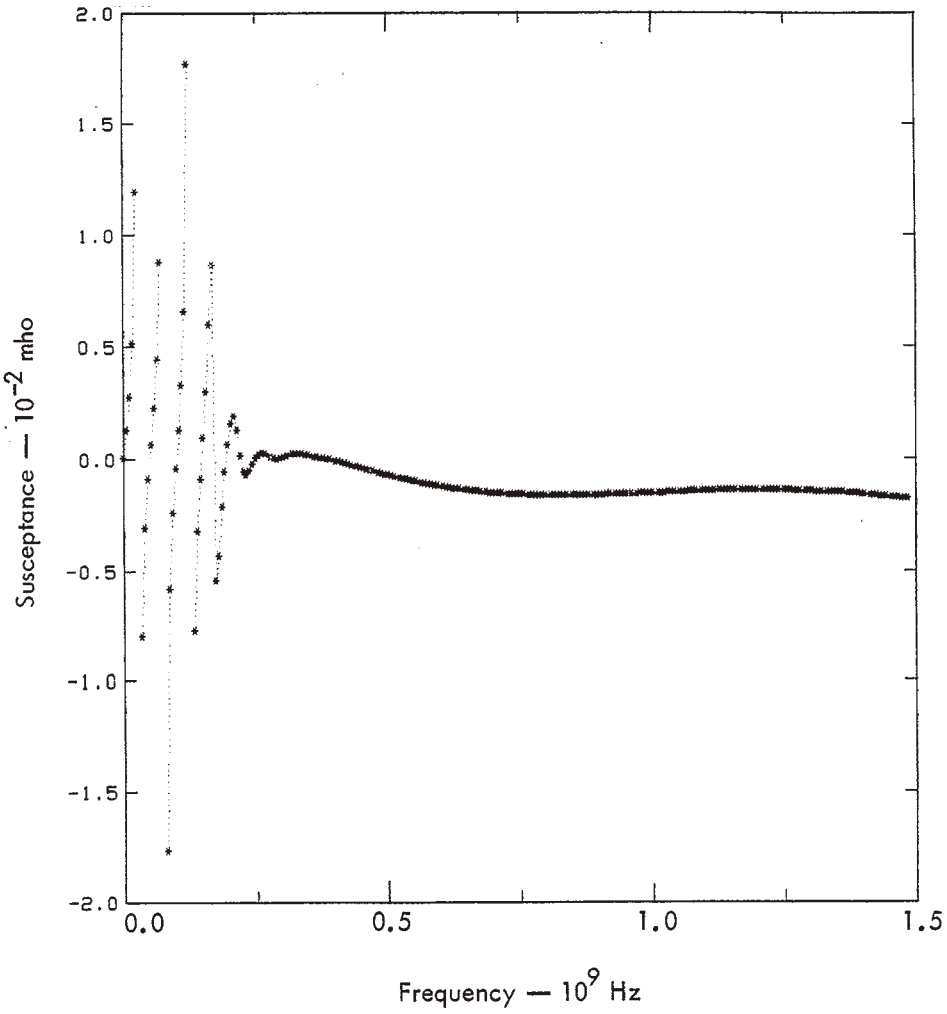

Fig. A1. (Continued.) (b) Imaginary part of the driving-point admittance.

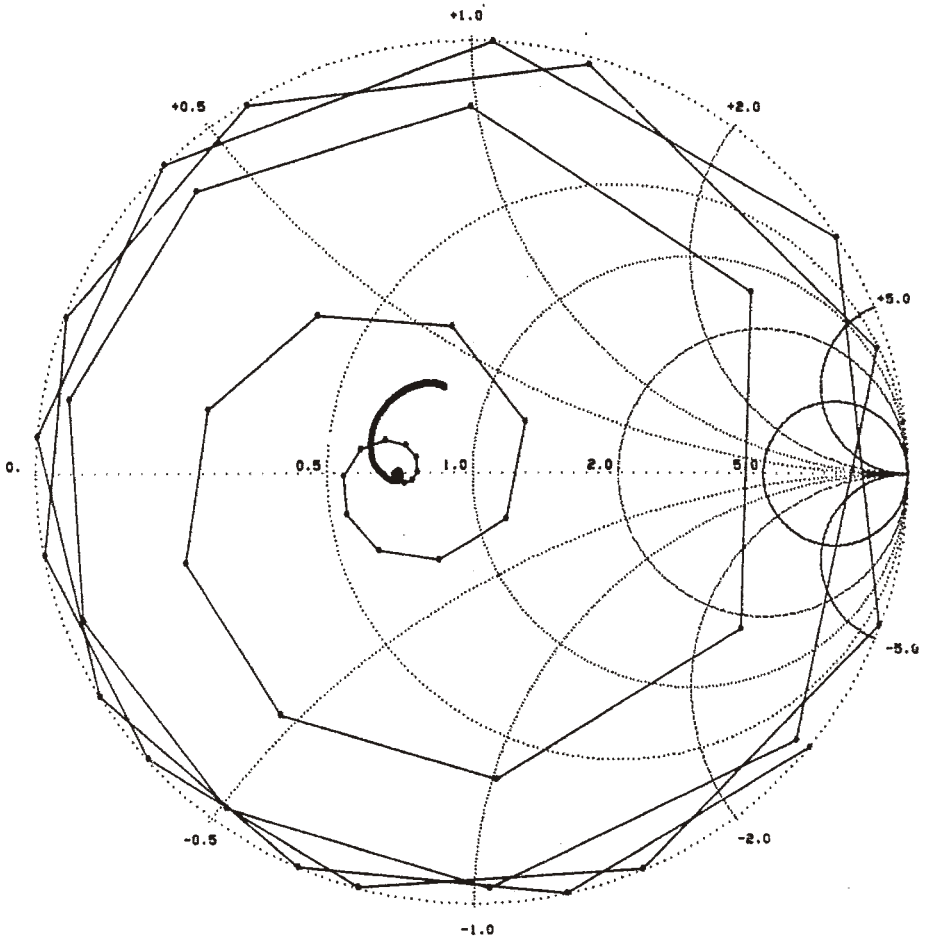

$Z_0 = 300\ \Omega$

Fig. A1. (Continued.) (c) Driving-point impedance normalized to 300 Ω.

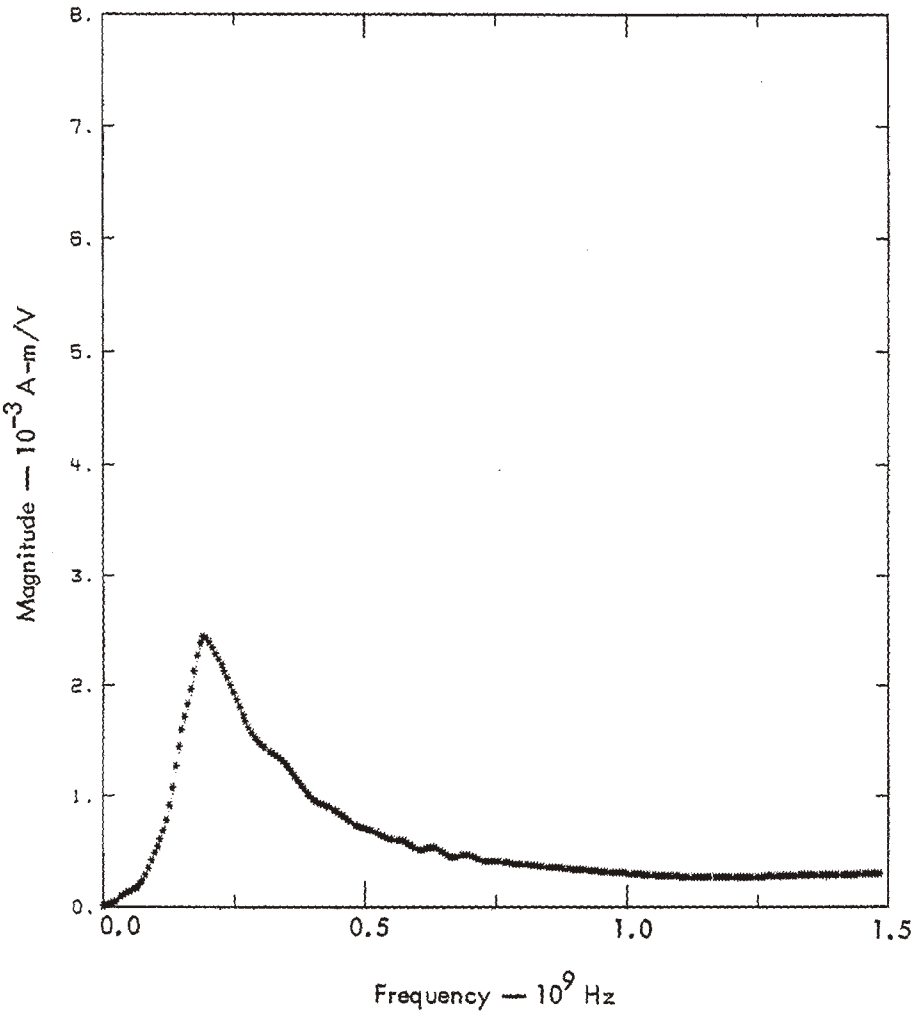

Fig. A1. (Continued.) (d) Magnitude of the boresight transfer admittance.

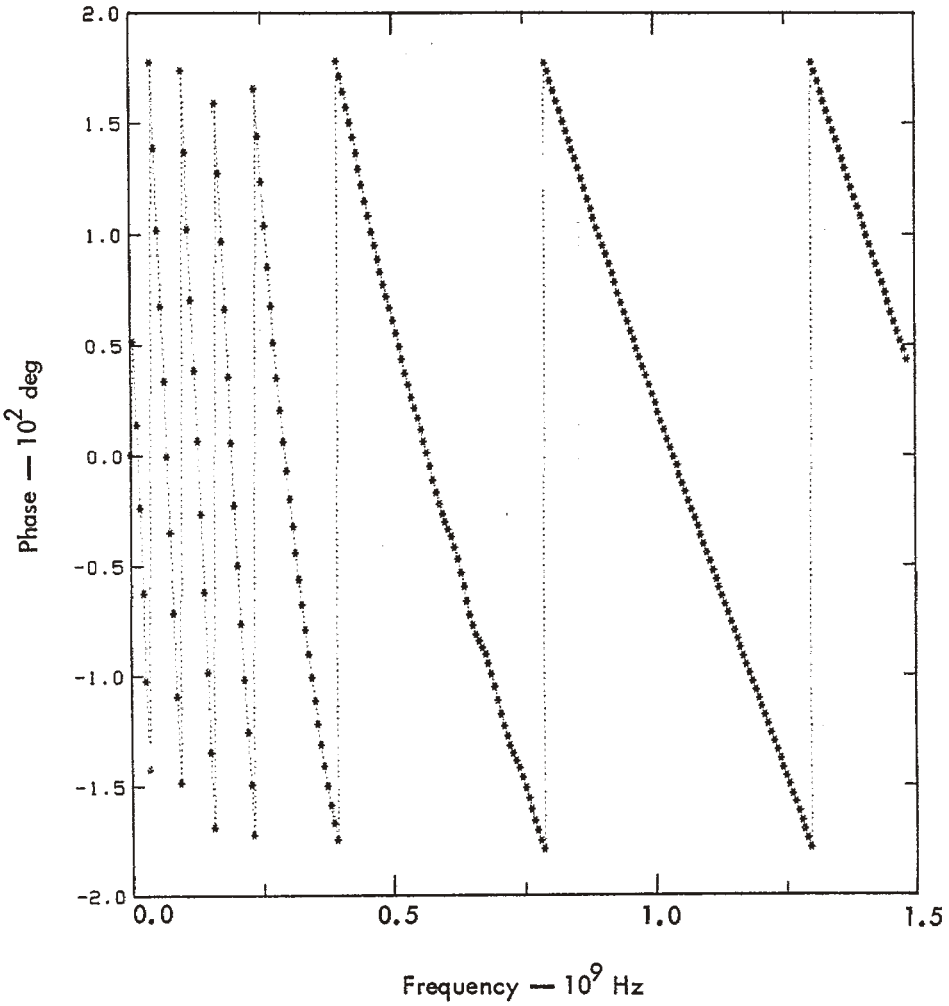

Fig. A1. (Continued.) (e) Phase of the boresight transfer admittance.

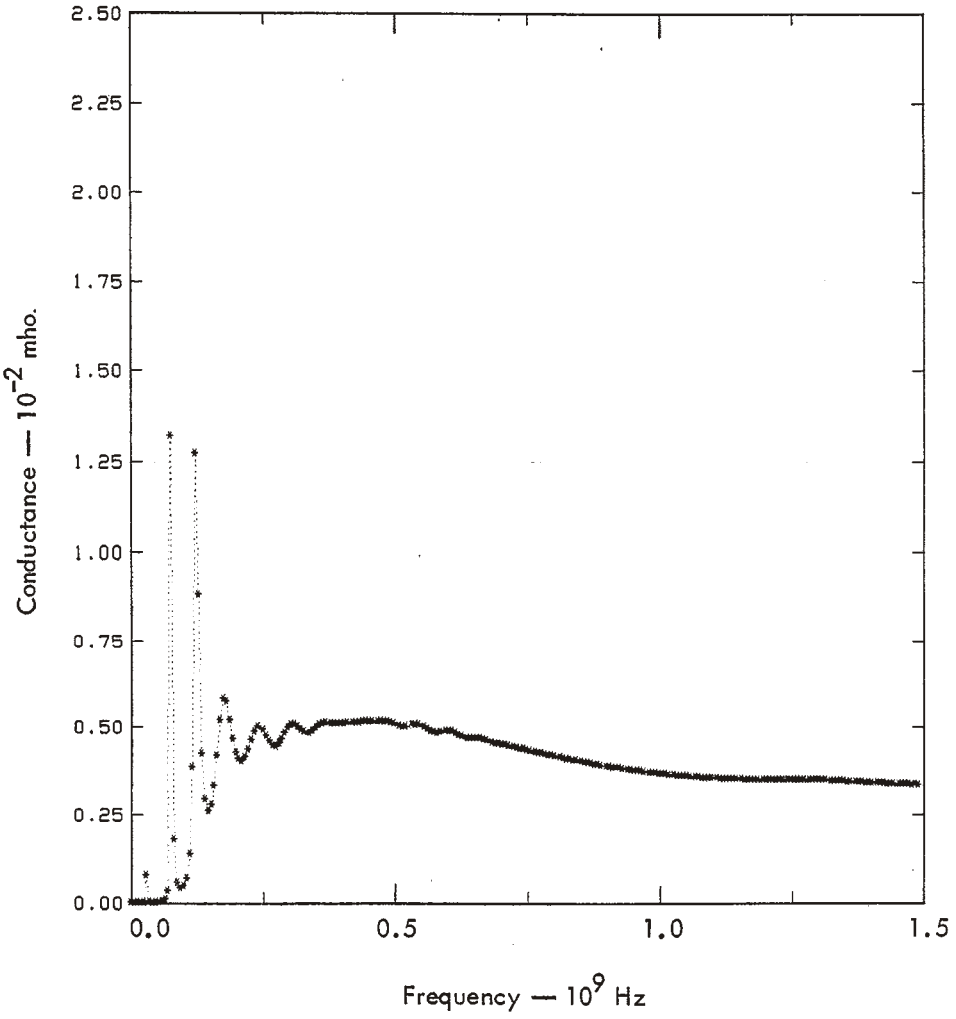

Fig. A2. Antenna characteristics for antenna A2 in Table A1.
(a) Real part of the driving-point admittance.
(Continued on the following four pages.)

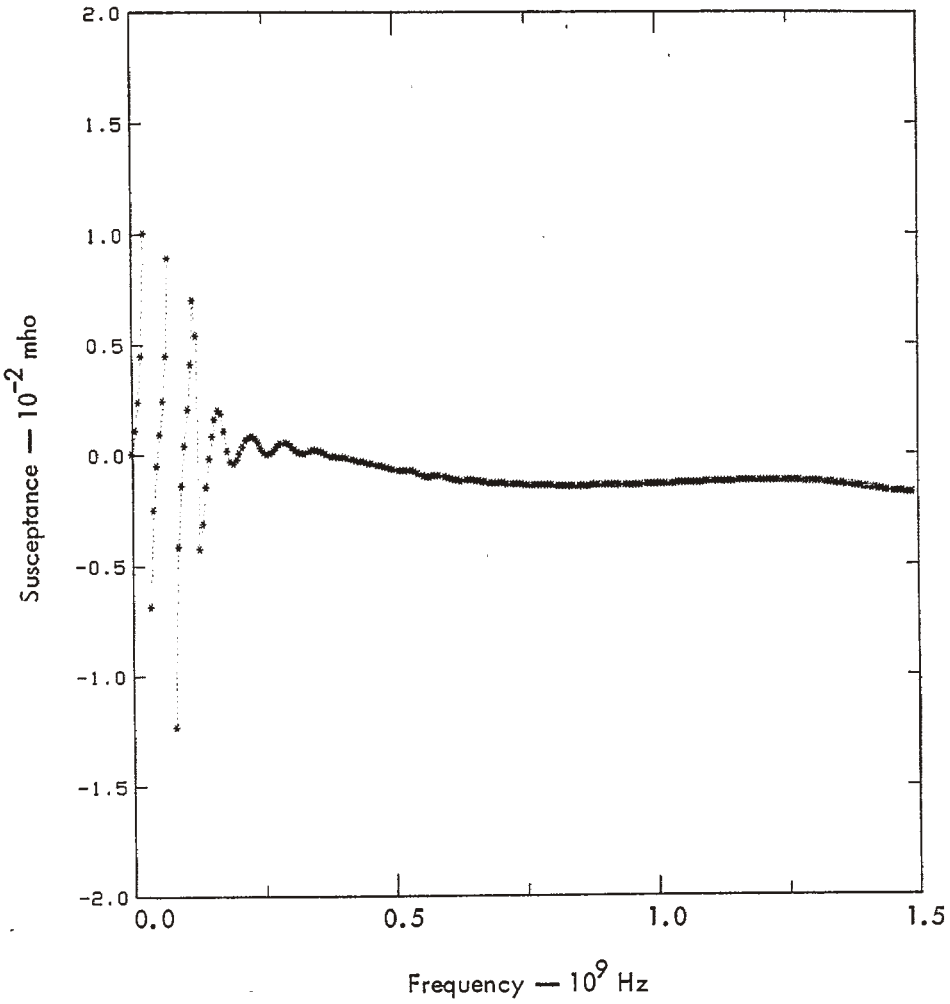

Fig. A2. (Continued.) (b) Imaginary part of the driving-point admittance.

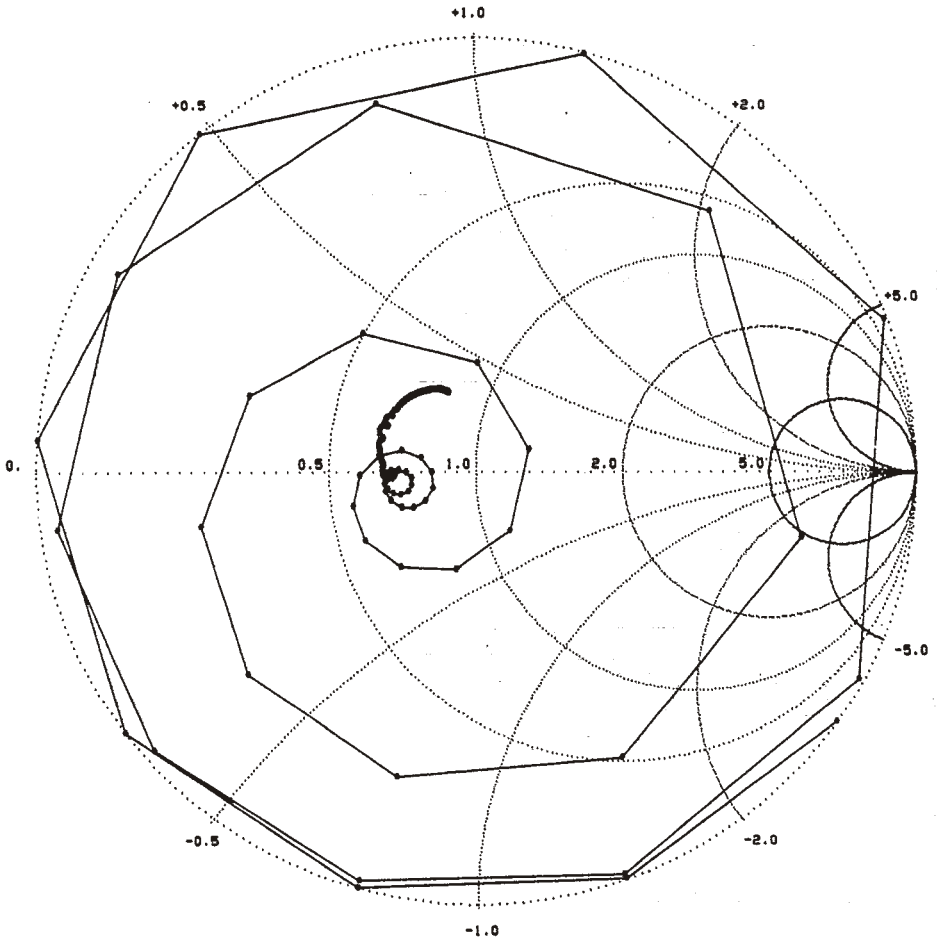

$Z_0 = 300\ \Omega$

Fig. A2. (Continued.) (c) Driving-point impedance normalized to 300 Ω.

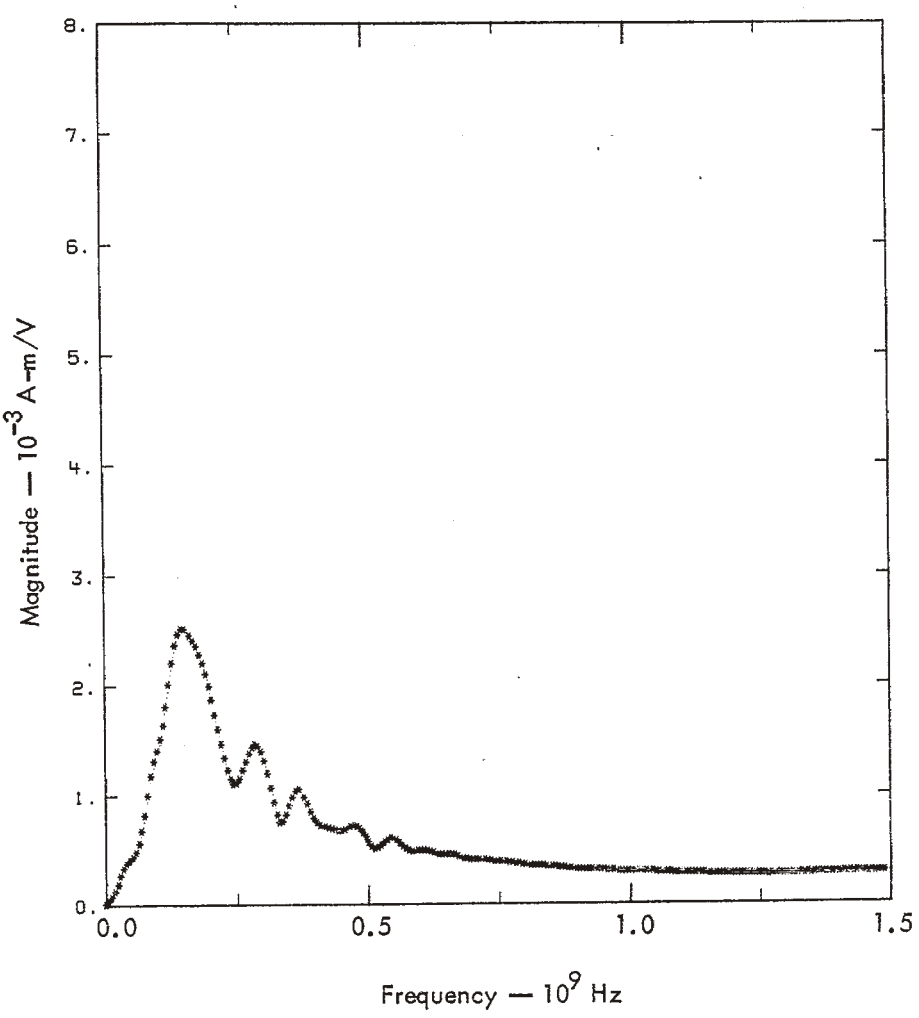

Fig. A2. (Continued.) (d) Magnitude of the boresight transfer admittance.

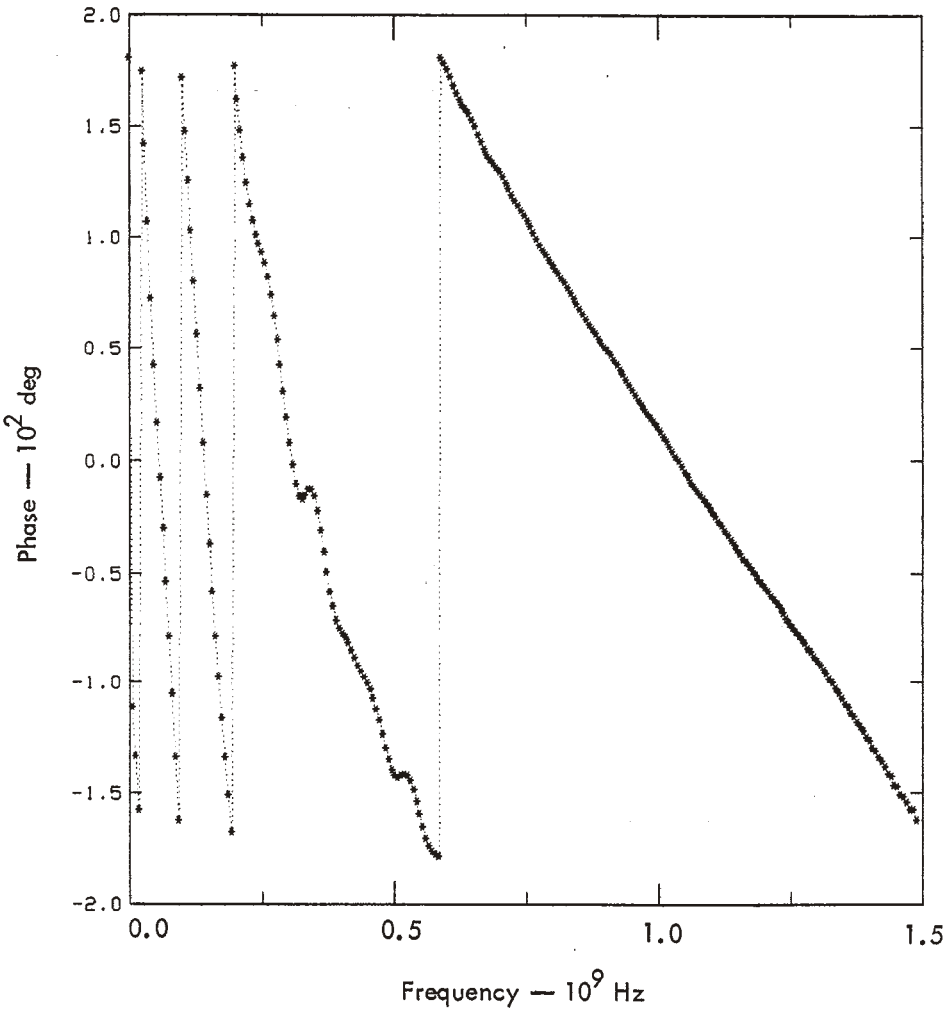

Fig. A2. (Continued.) (e) Phase of the boresight transfer admittance.

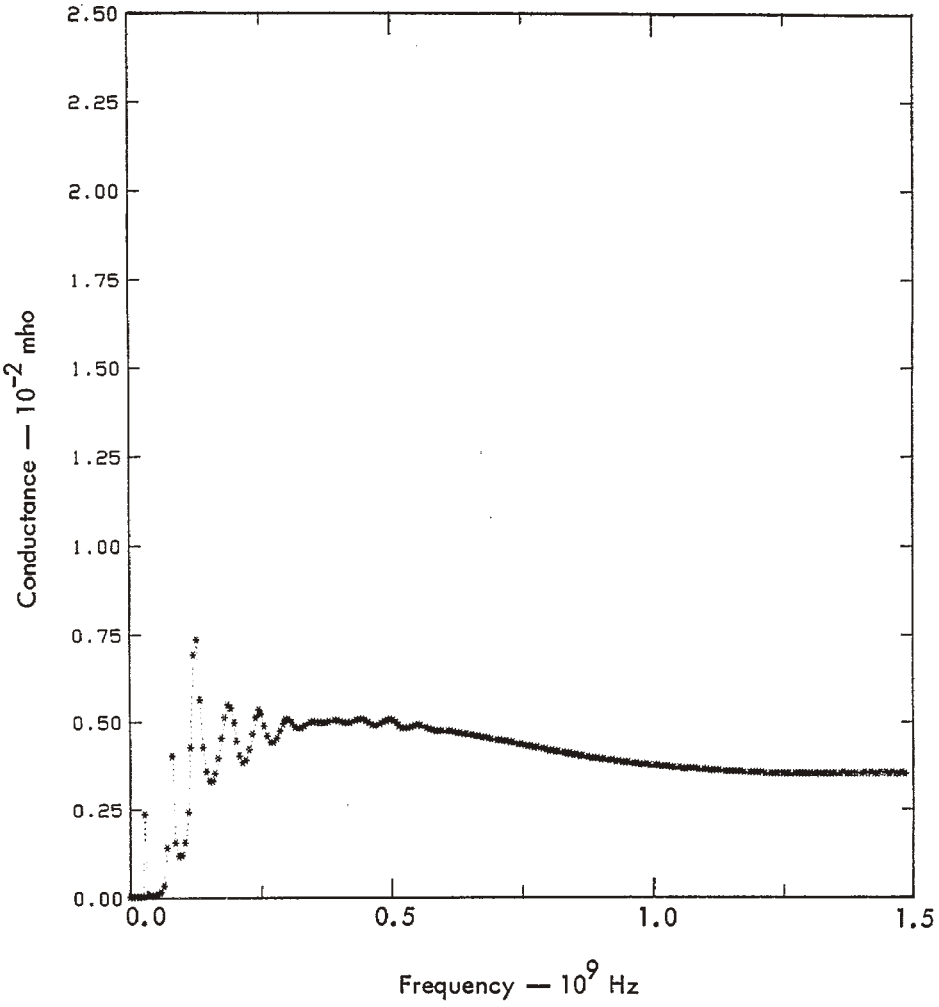

Fig. A3. Antenna characteristics for antenna A3 in Table A1.
(a) Real part of the driving-point admittance.
(Continued on the following four pages.)

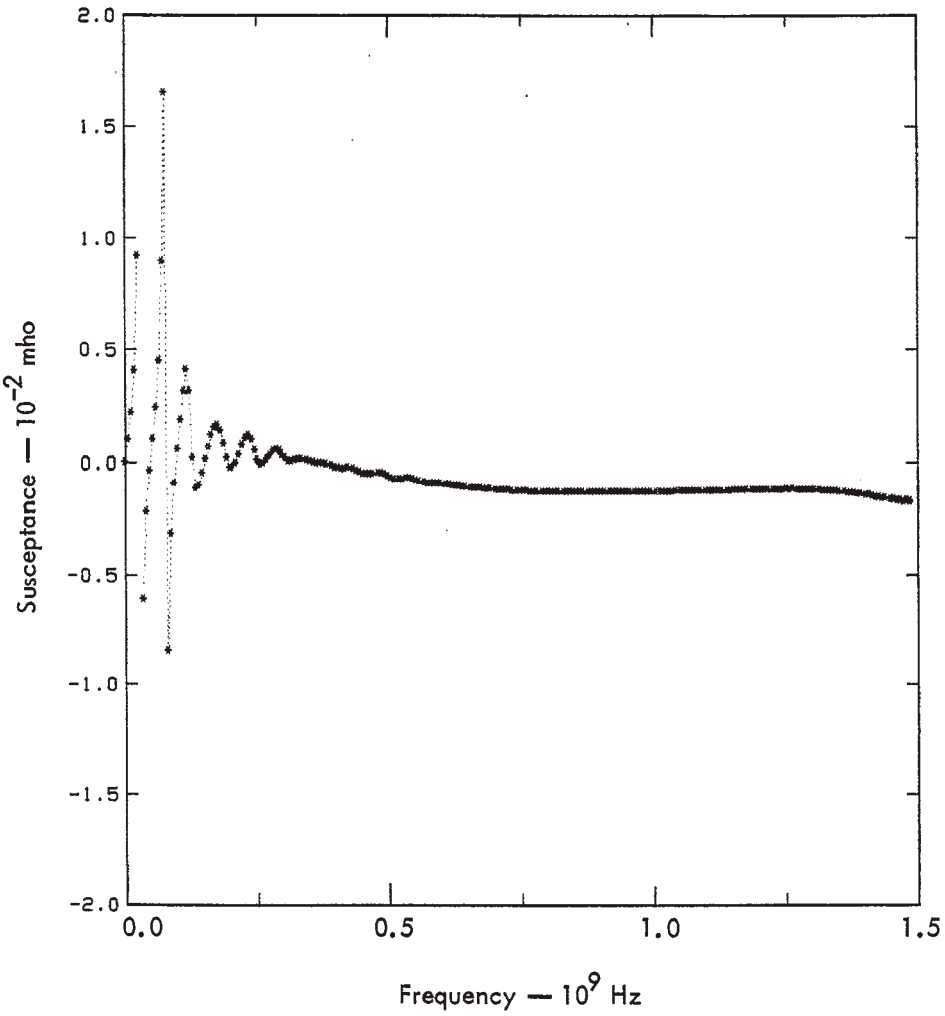

Fig. A3. (Continued.) (b) Imaginary part of the driving-point admittance.

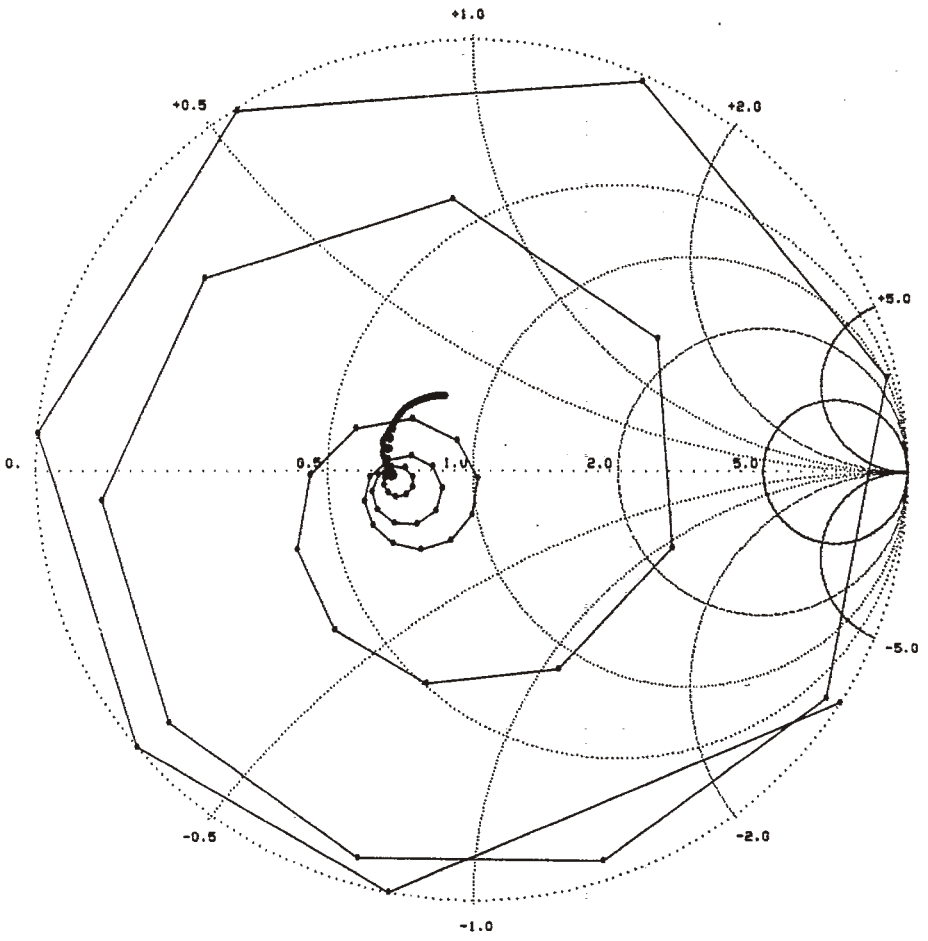

$Z_0 = 300\ \Omega$

Fig. A3. (Continued.) (c) Driving-point impedance normalized to 300 Ω.

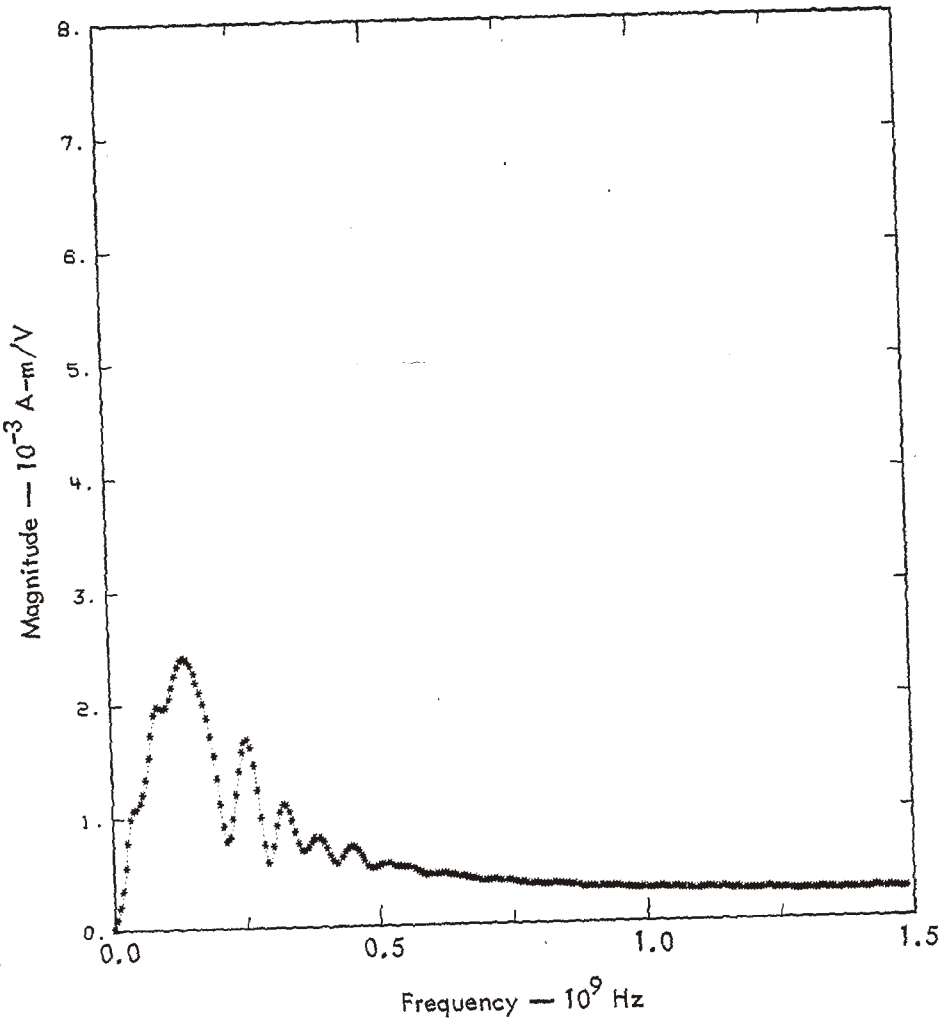

Fig. A3. (Continued.) (d) Magnitude of the boresight transfer admittance.

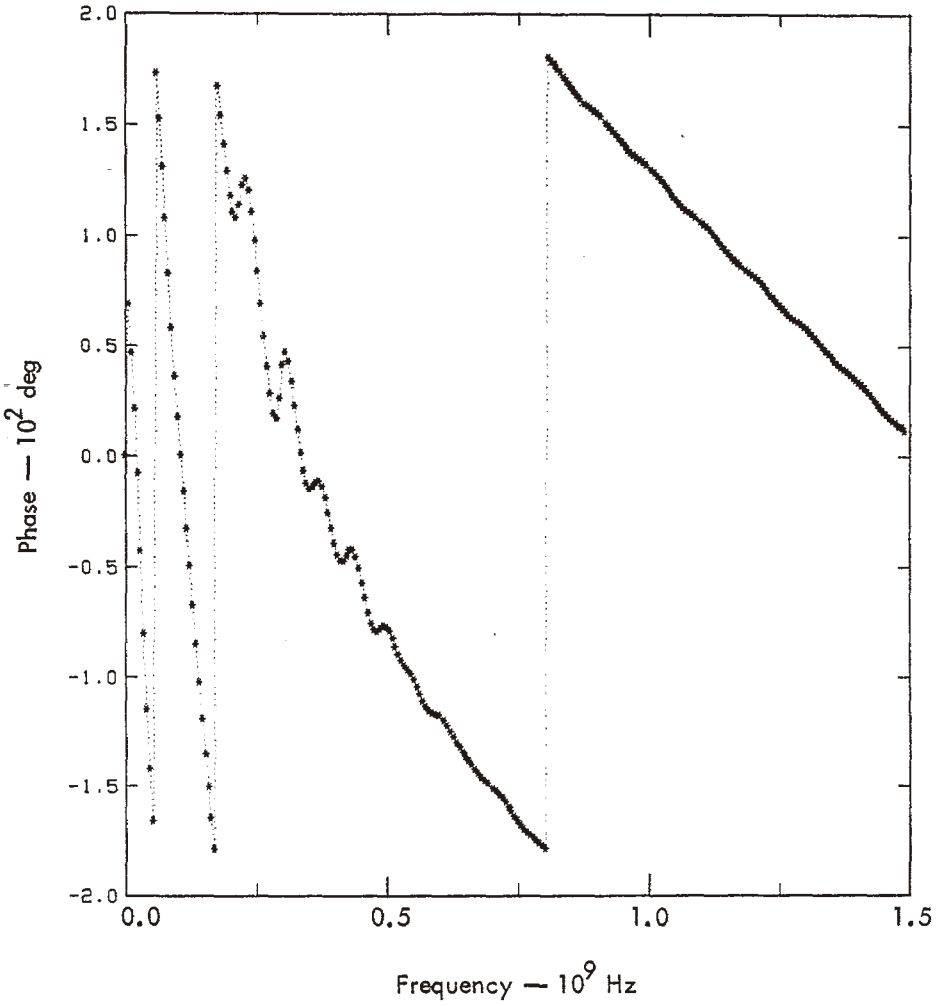

Fig. A3. (Continued.) (e) Phase of the boresight transfer admittance.

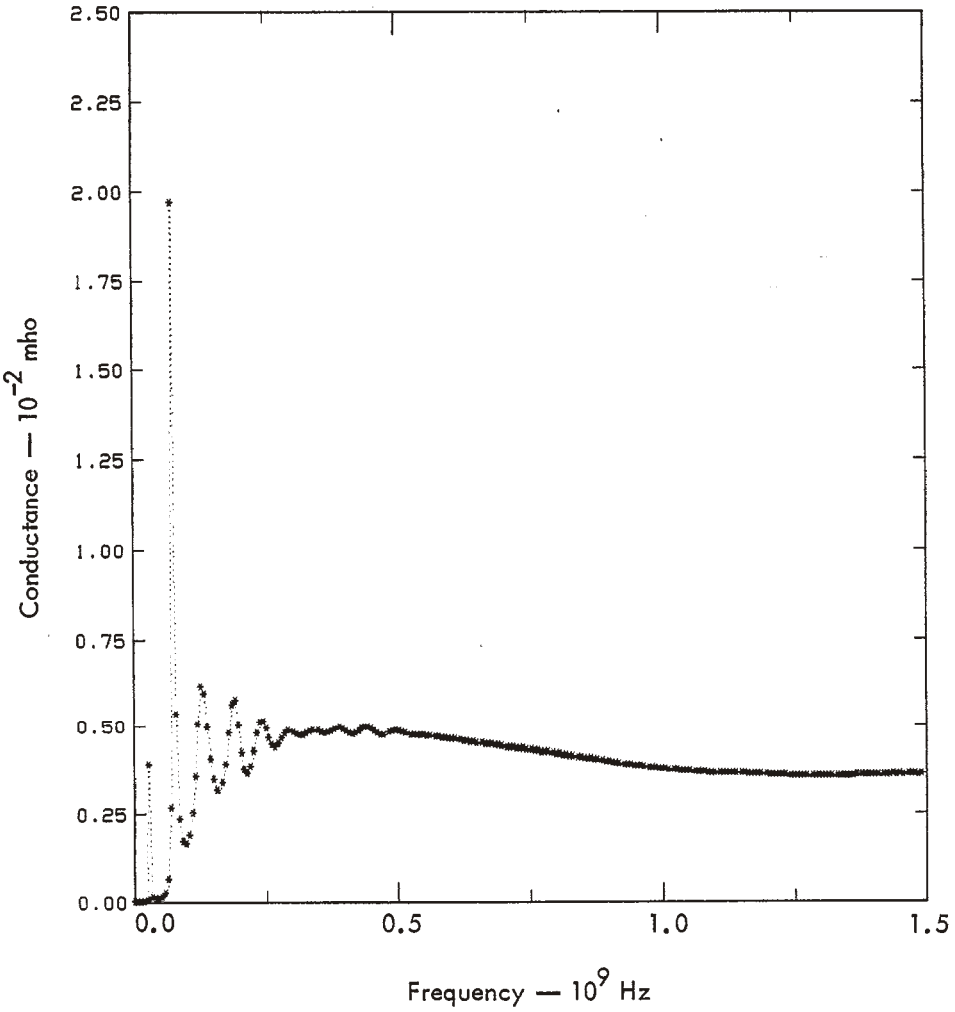

Fig. A4. Antenna characteristics for antenna A4 in Table A1.
(a) Real part of the driving-point admittance.
(Continued on the following four pages.)

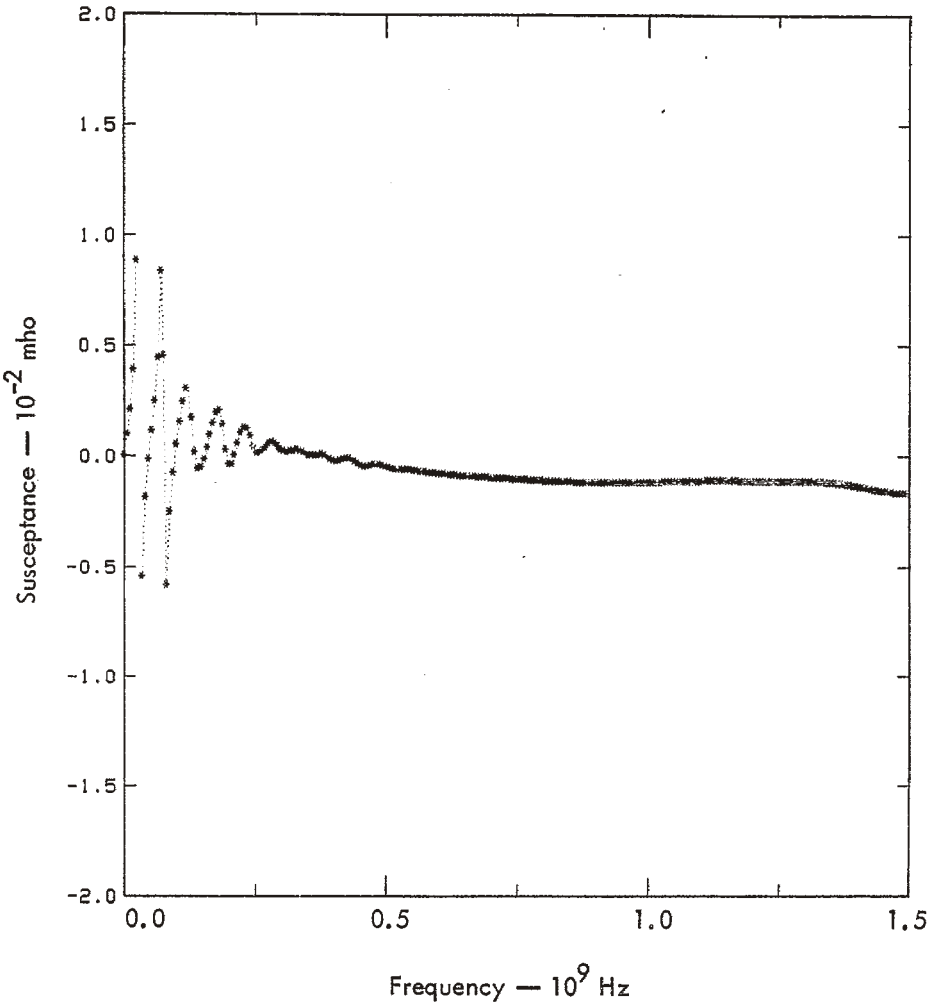

Fig. A4. (Continued.) (b) Imaginary part of the driving-point admittance.

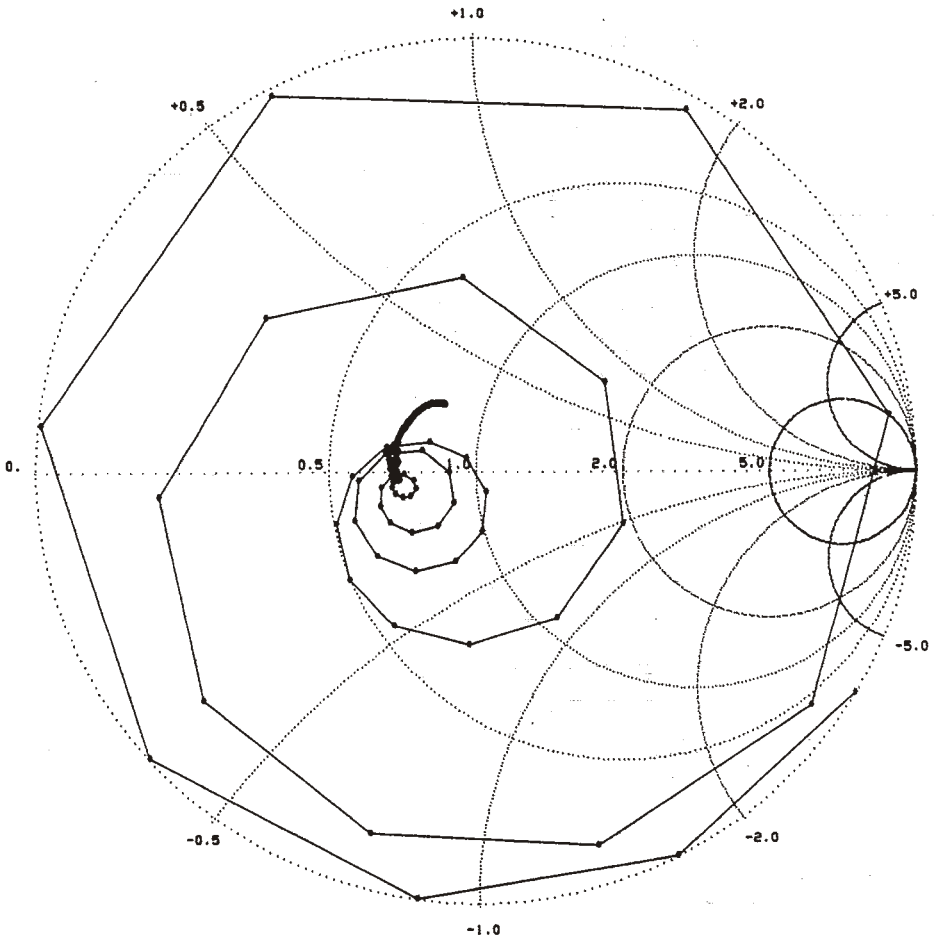

$Z_0 = 300\ \Omega$

Fig. A4. (Continued.) (c) Driving-point impedance normalized to 300 Ω.

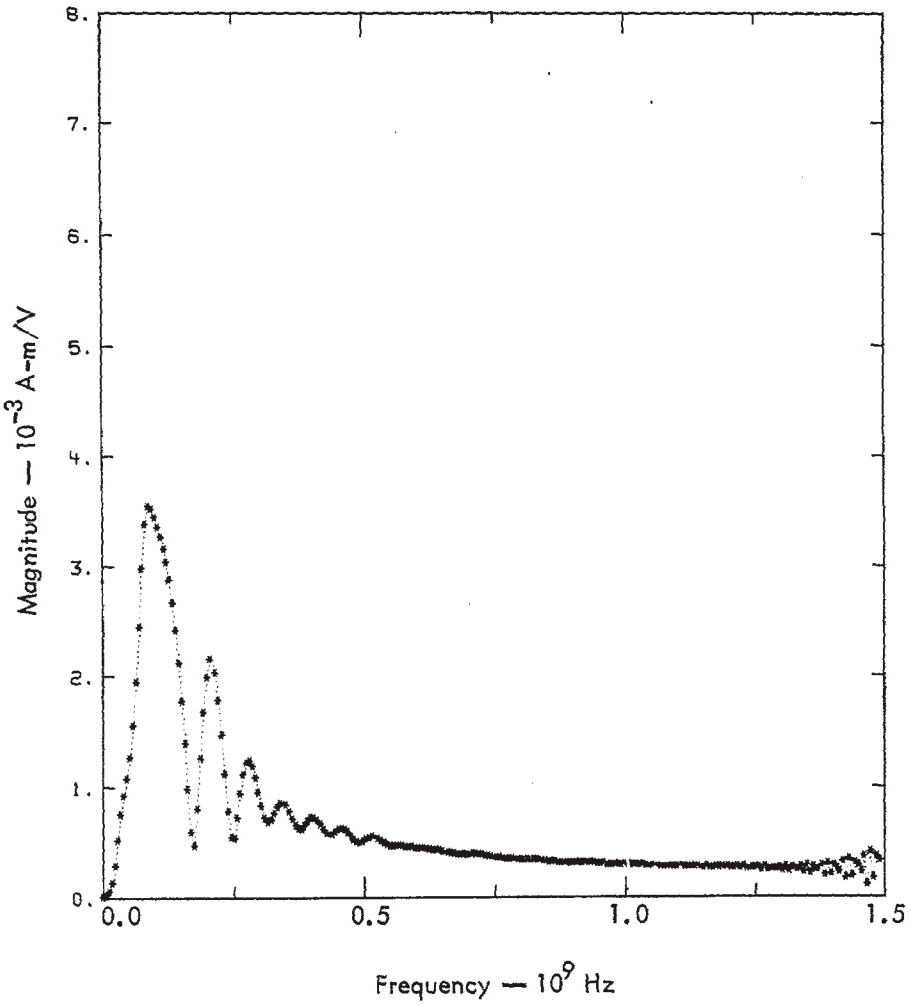

Fig. A4. (Continued.) (d) Magnitude of the boresight transfer admittance.

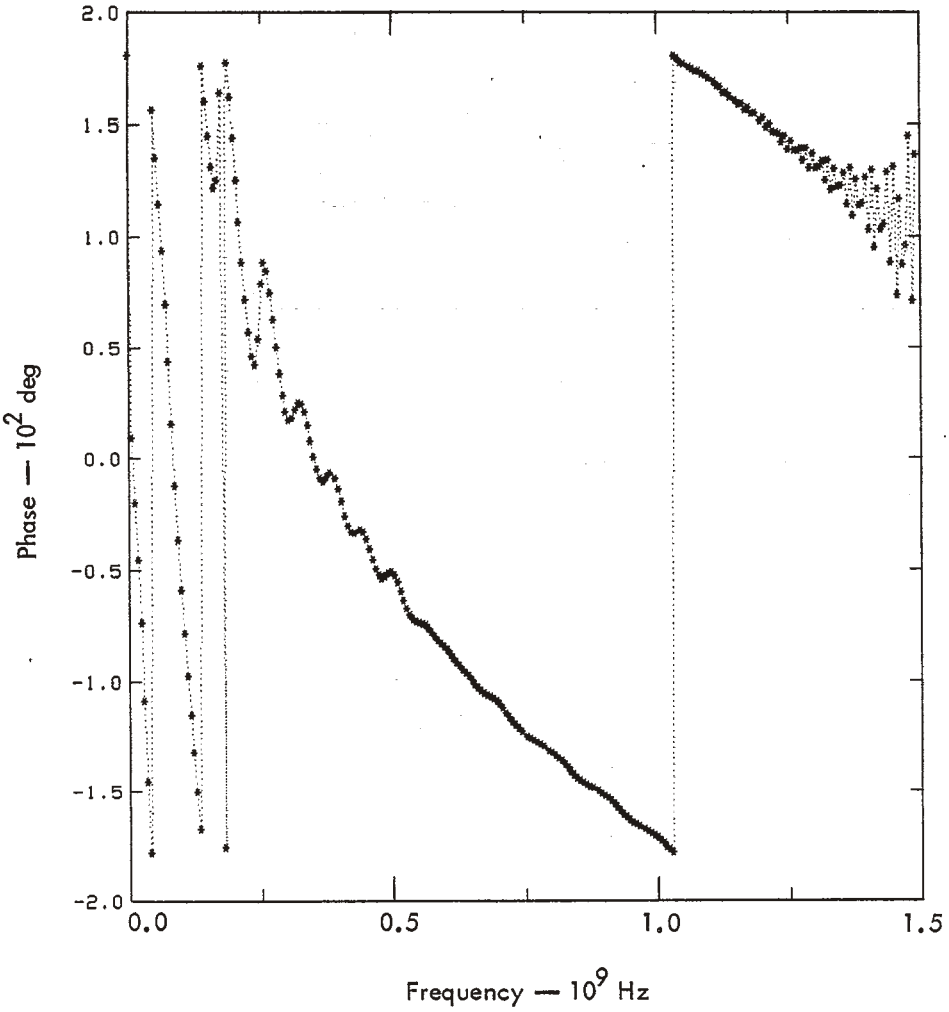

Fig. A4. (Continued.) (e) Phase of the boresight transfer admittance.

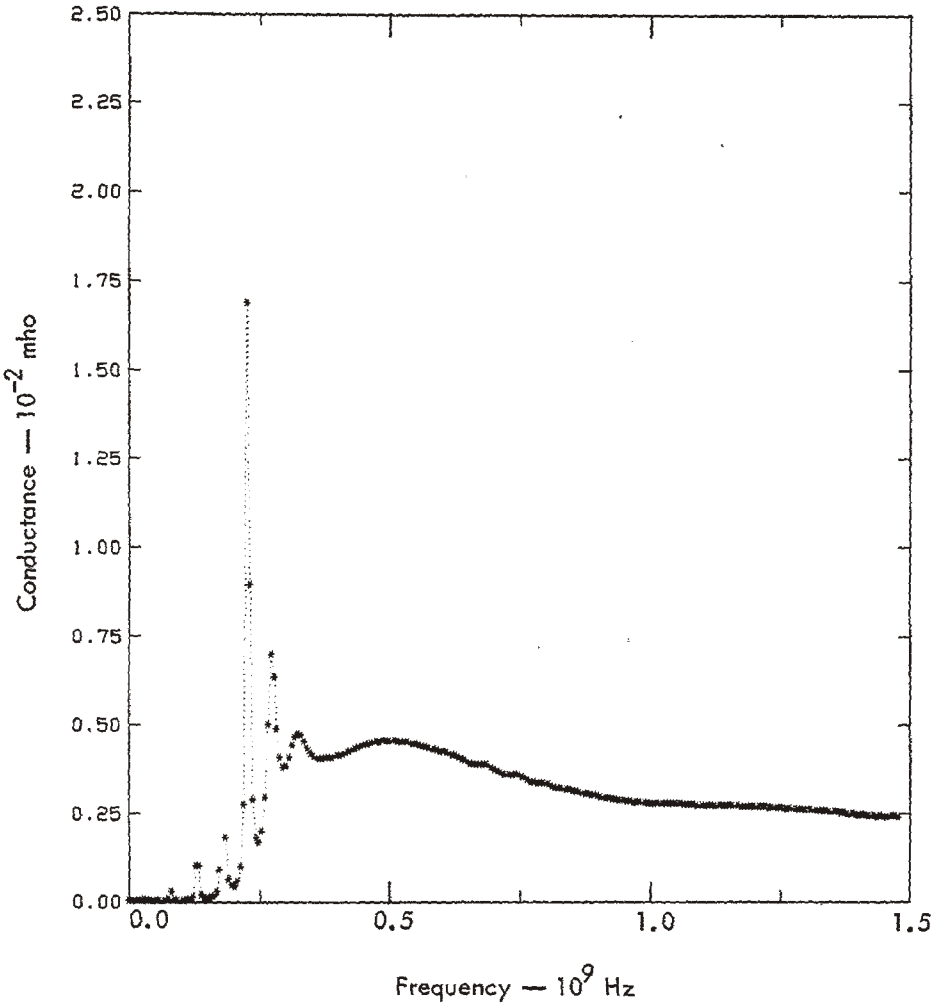

Fig. A5. Antenna characteristics for antenna A5 in Table A1.
(a) Real part of the driving-point admittance.
(Continued on the following four pages.)

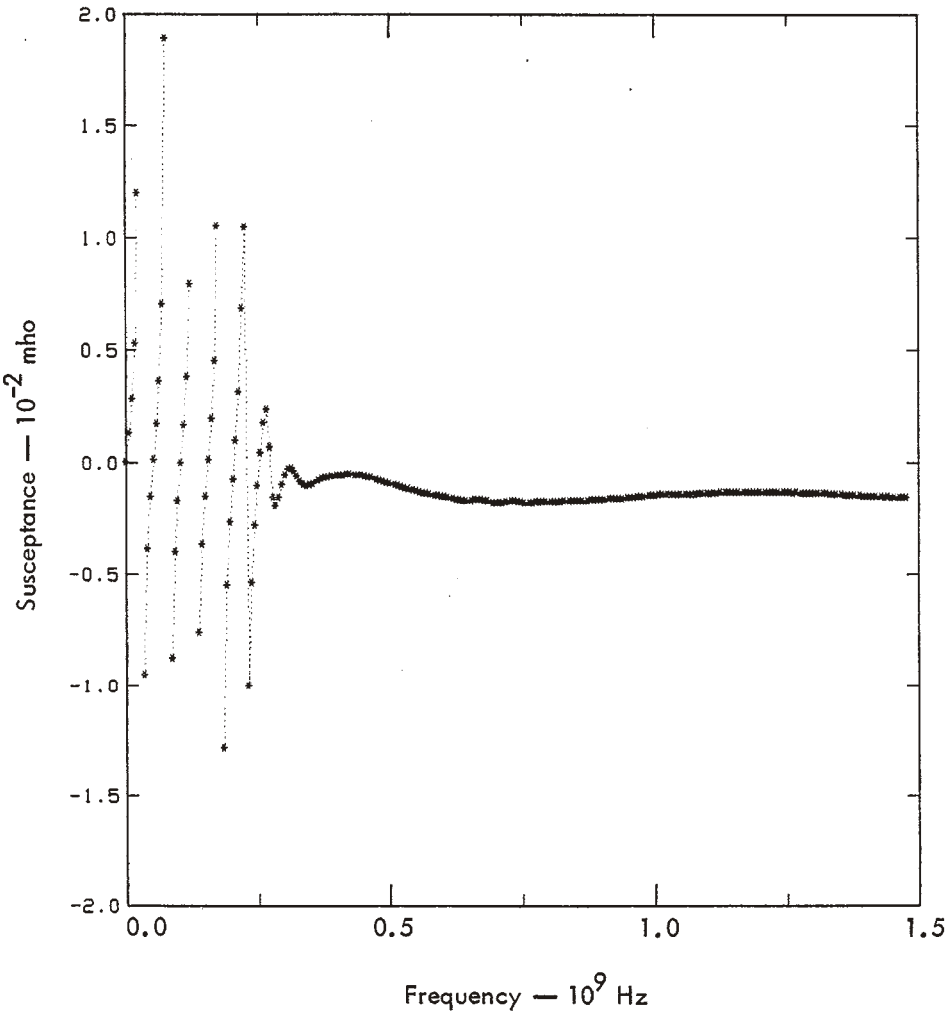

Fig. A5. (Continued.) (b) Imaginary part of the driving-point admittance.

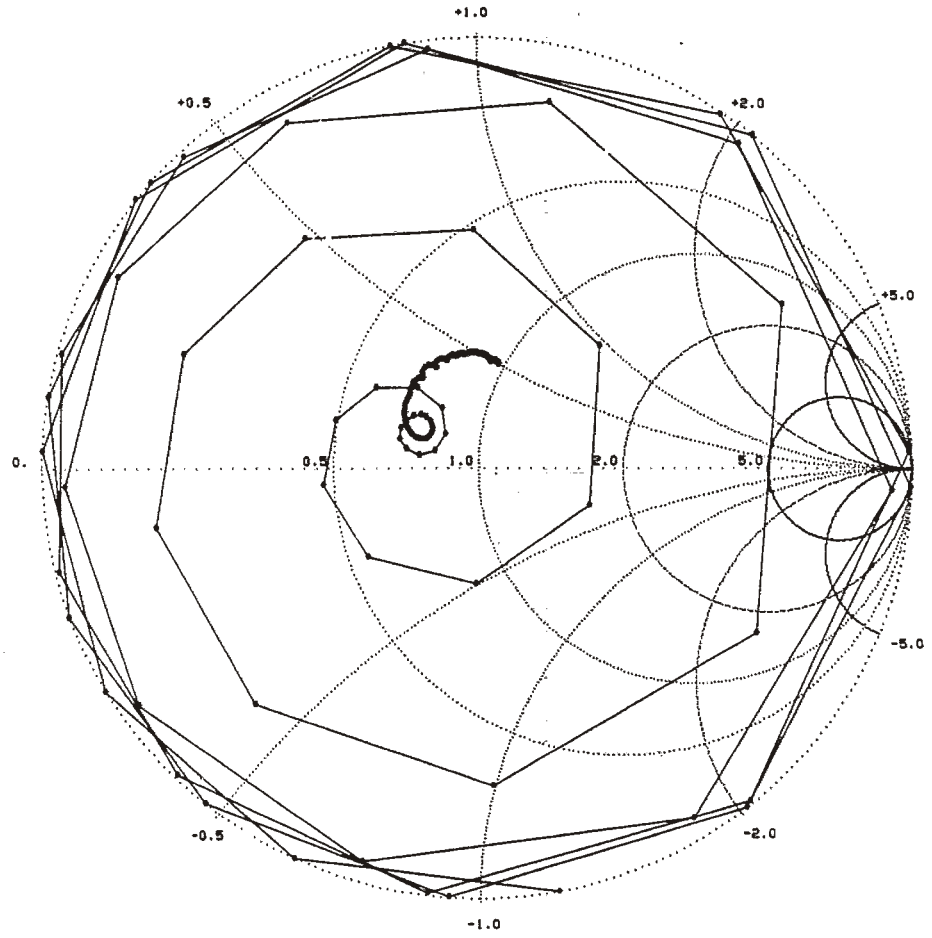

$Z_0 = 300\ \Omega$

Fig. A5. (Continued.) (c) Driving-point impedance normalized to 300 Ω.

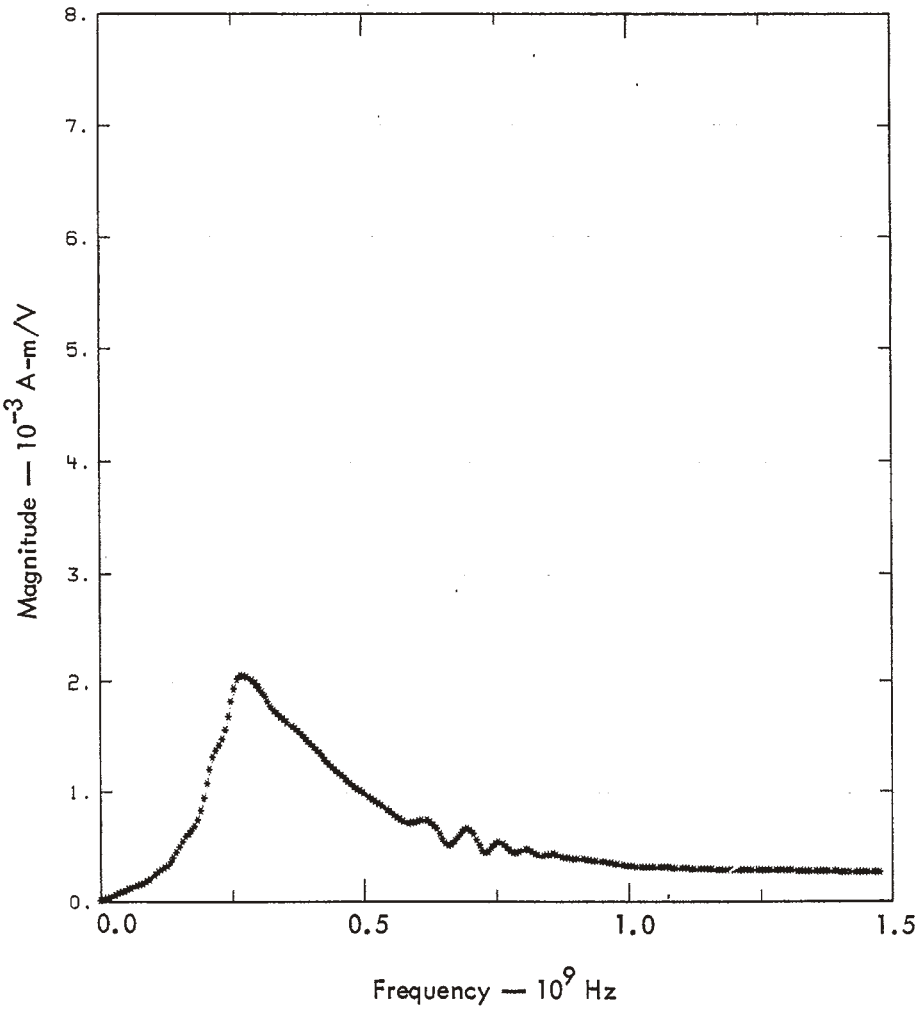

Fig. A5. (Continued.) (d) Magnitude of the boresight transfer admittance.

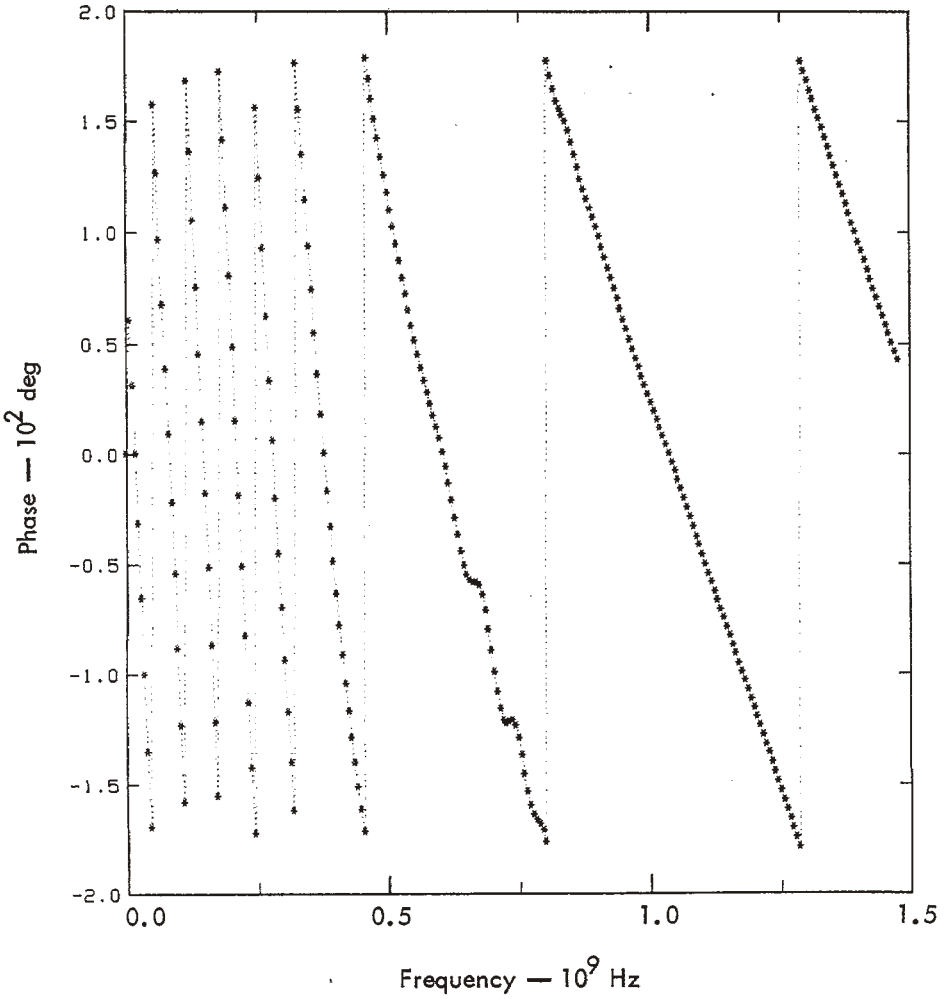

Fig. A5. (Continued.) (e) Phase of the boresight transfer admittance.

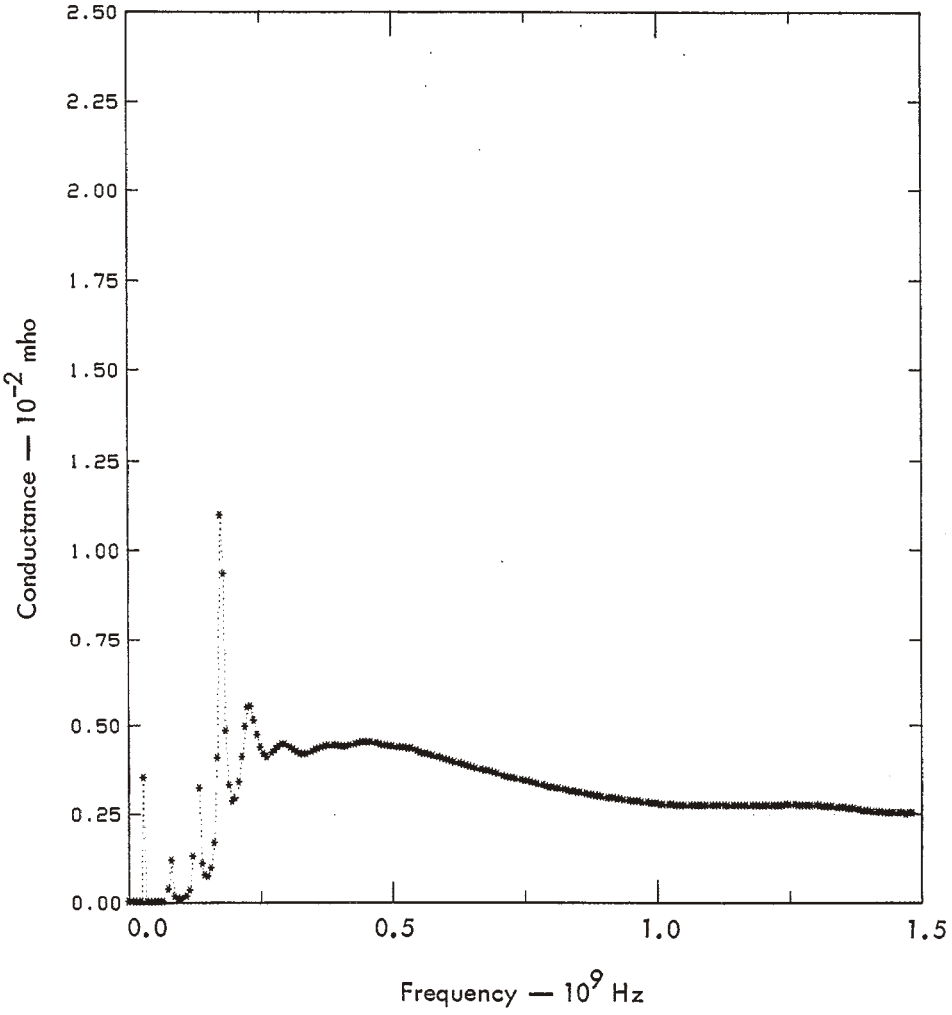

Fig. A6. Antenna characteristics for antenna A6 in Table A1.
(a) Real part of the driving-point admittance.
(Continued on the following four pages.)

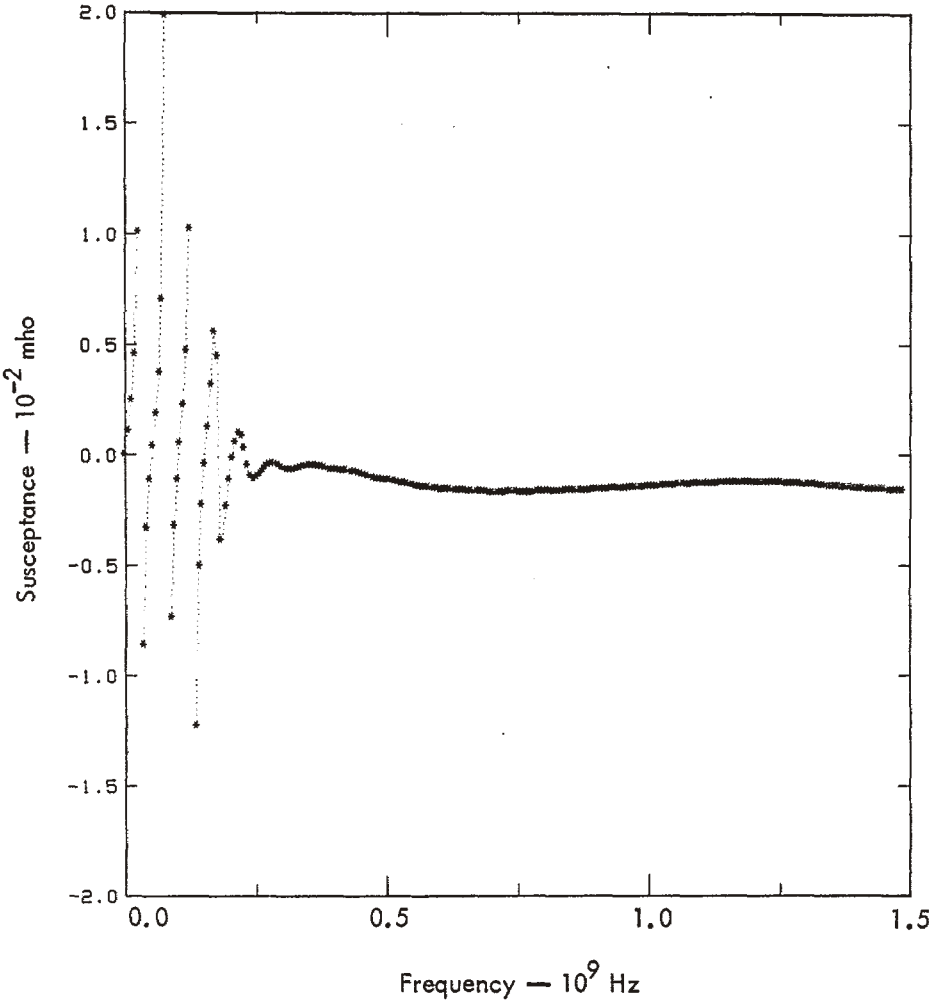

Fig. A6. (Continued.) (b) Imaginary part of the driving-point admittance.

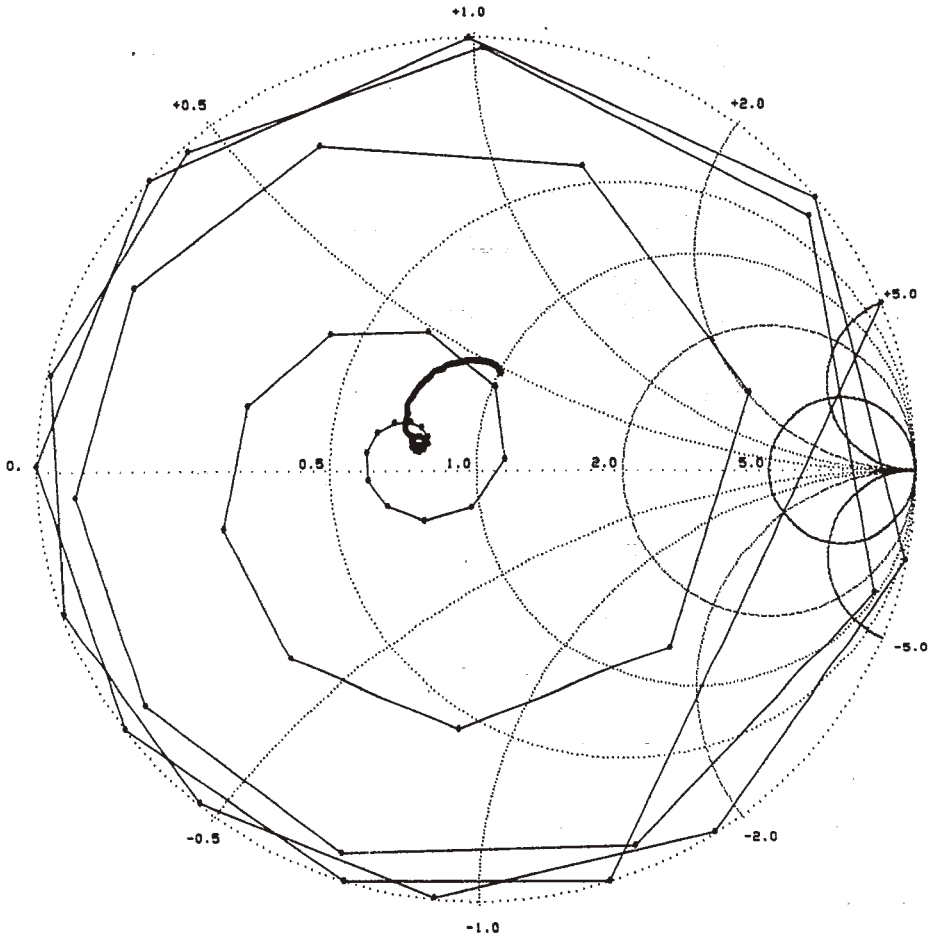

$Z_0 = 300\ \Omega$

Fig. A6. (Continued.) (c) Driving-point impedance normalized to 300 Ω.

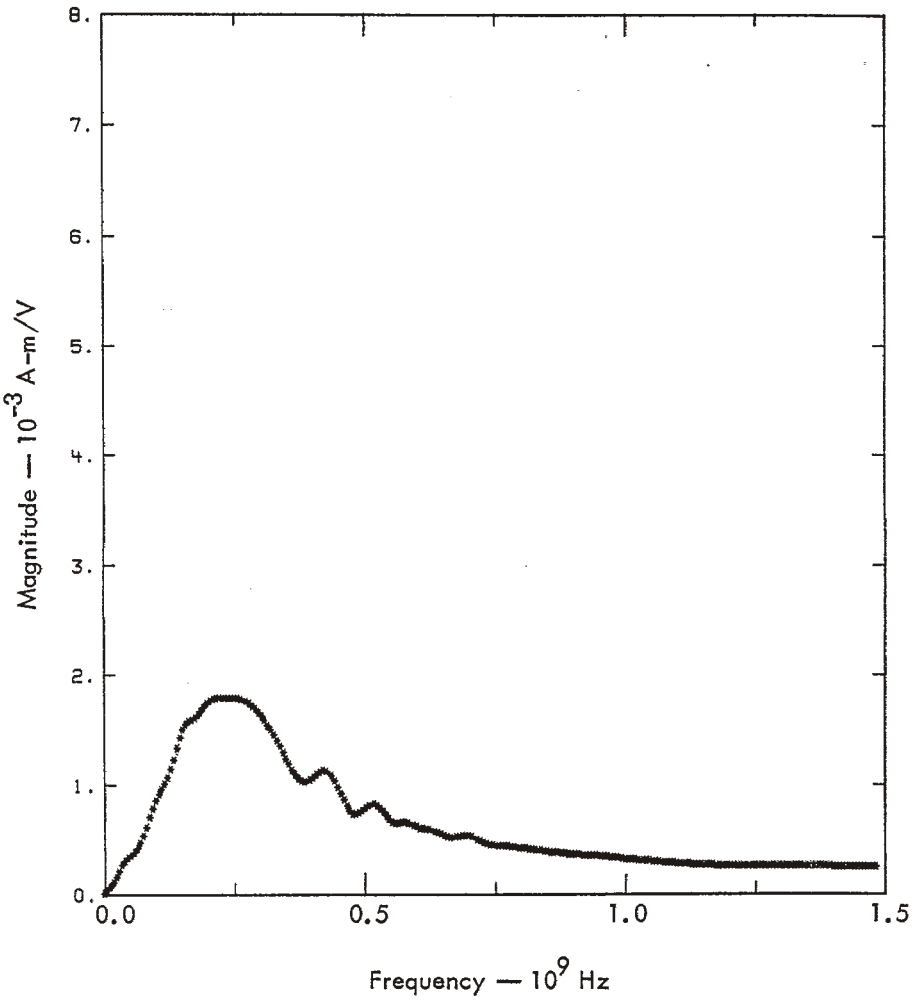

Fig. A6. (Continued.) (d) Magnitude of the boresight transfer admittance.

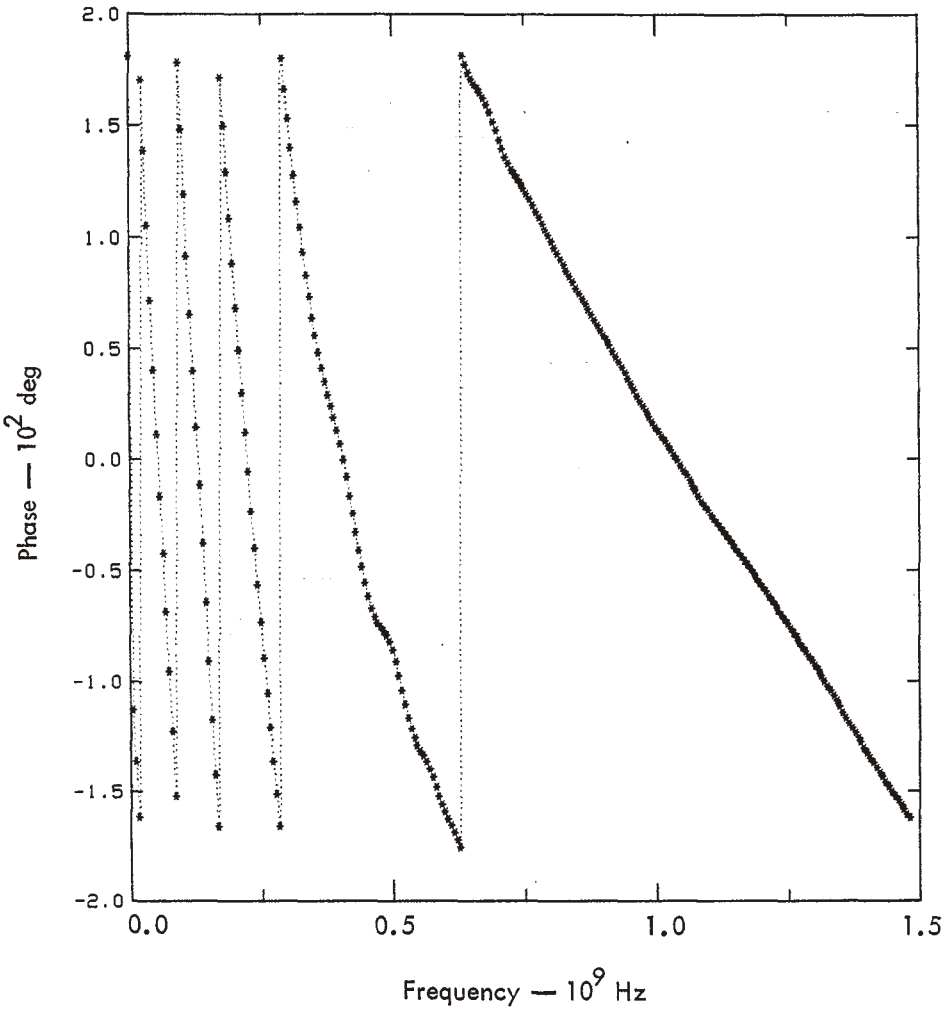

Fig. A6. (Continued.) (e) Phase of the boresight transfer admittance.

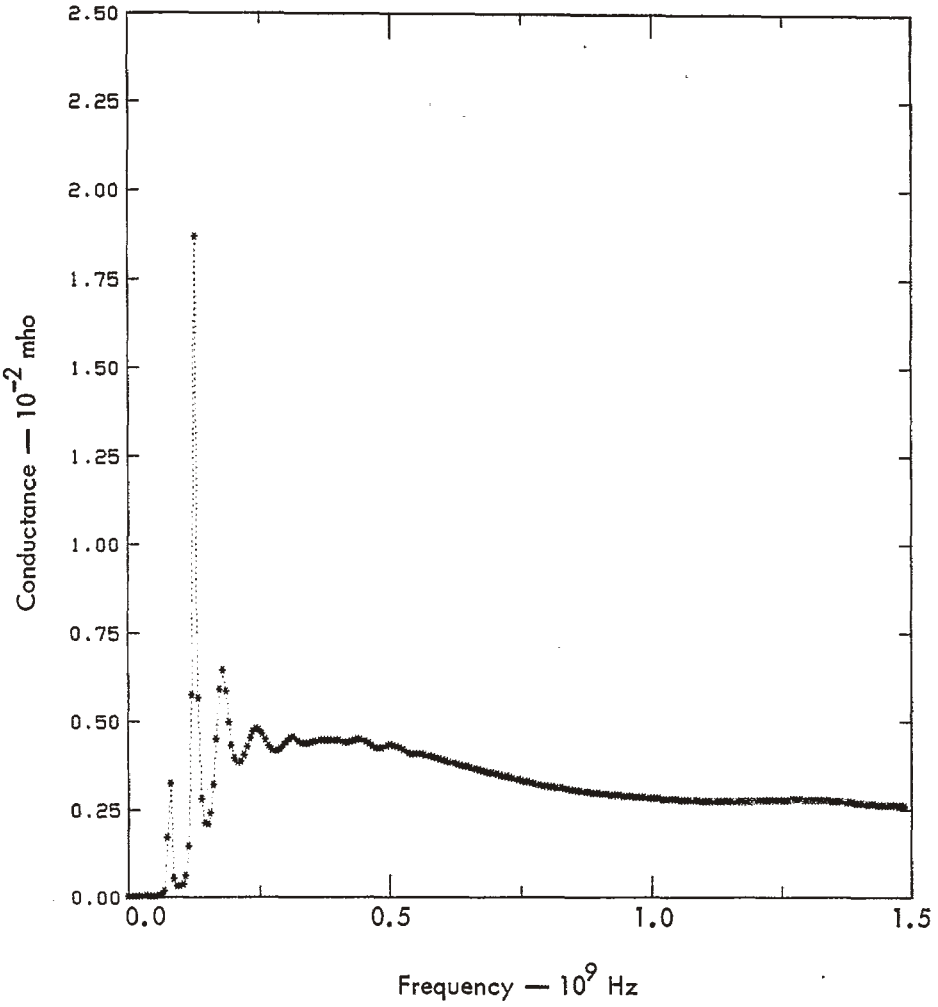

Fig. A7. Antenna characteristics for antenna A7 in Table A1.
(a) Real part of the driving-point admittance.
(Continued on the following four pages.)

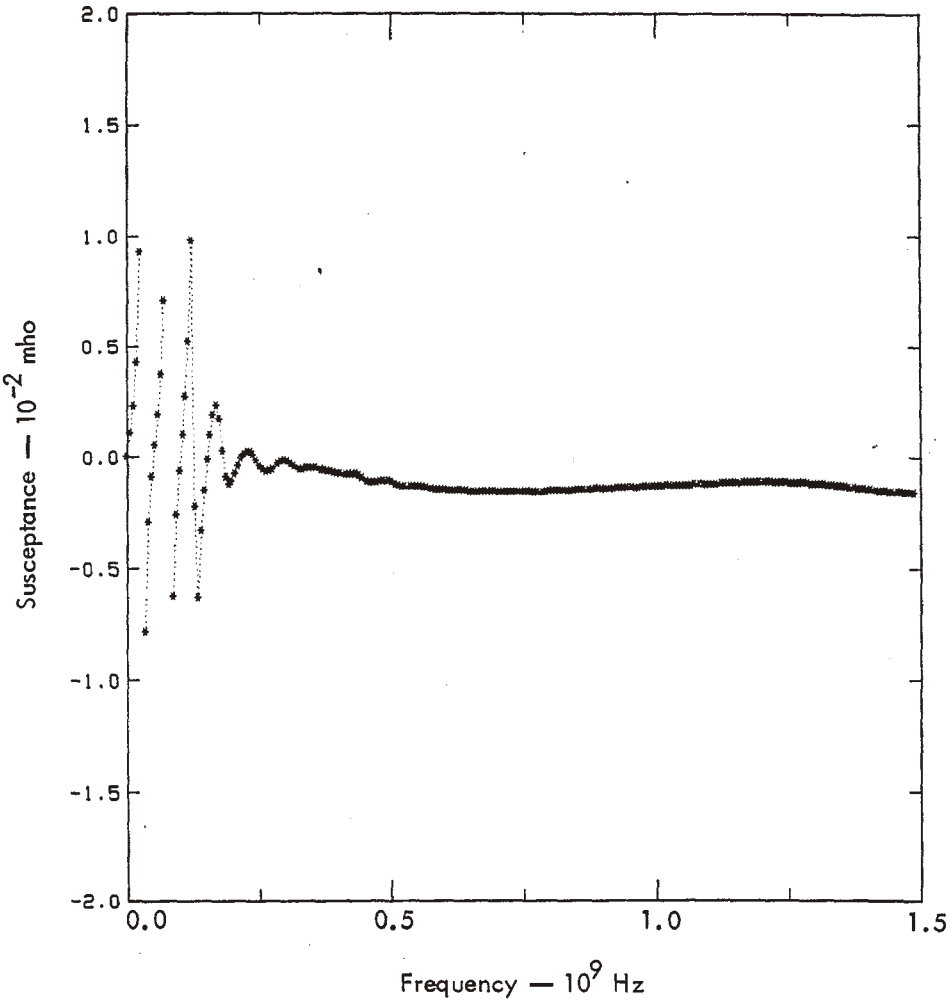

Fig. A7. (Continued.) (b) Imaginary part of the driving-point admittance.

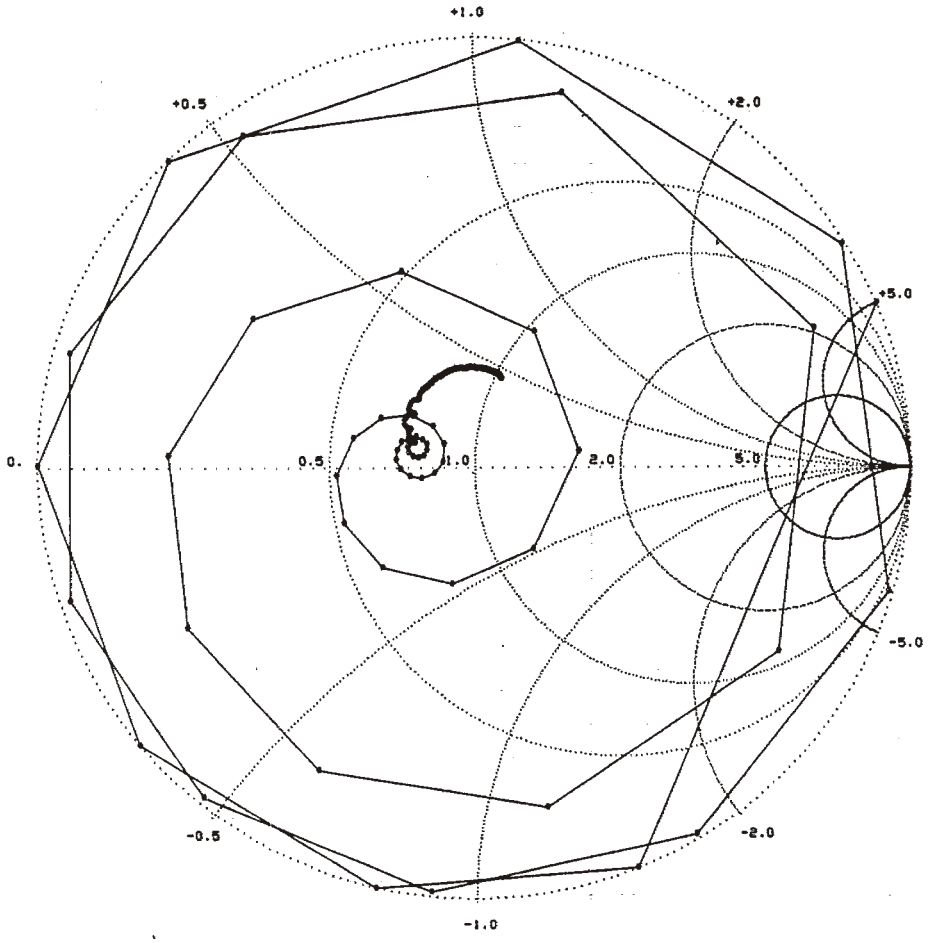

$Z_0 = 300\ \Omega$

Fig. A7. (Continued.) (c) Driving-point impedance normalized to 300 Ω.

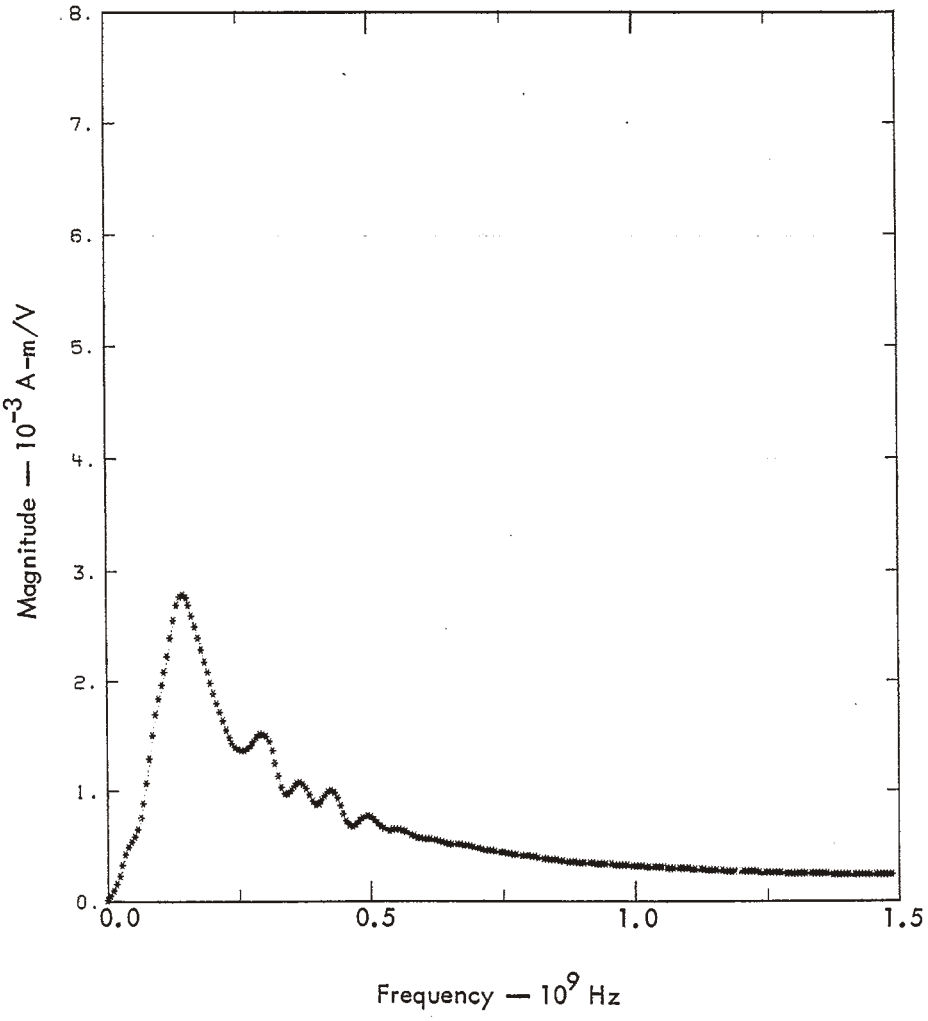

Fig. A7. (Continued.) (d) Magnitude of the boresight transfer admittance.

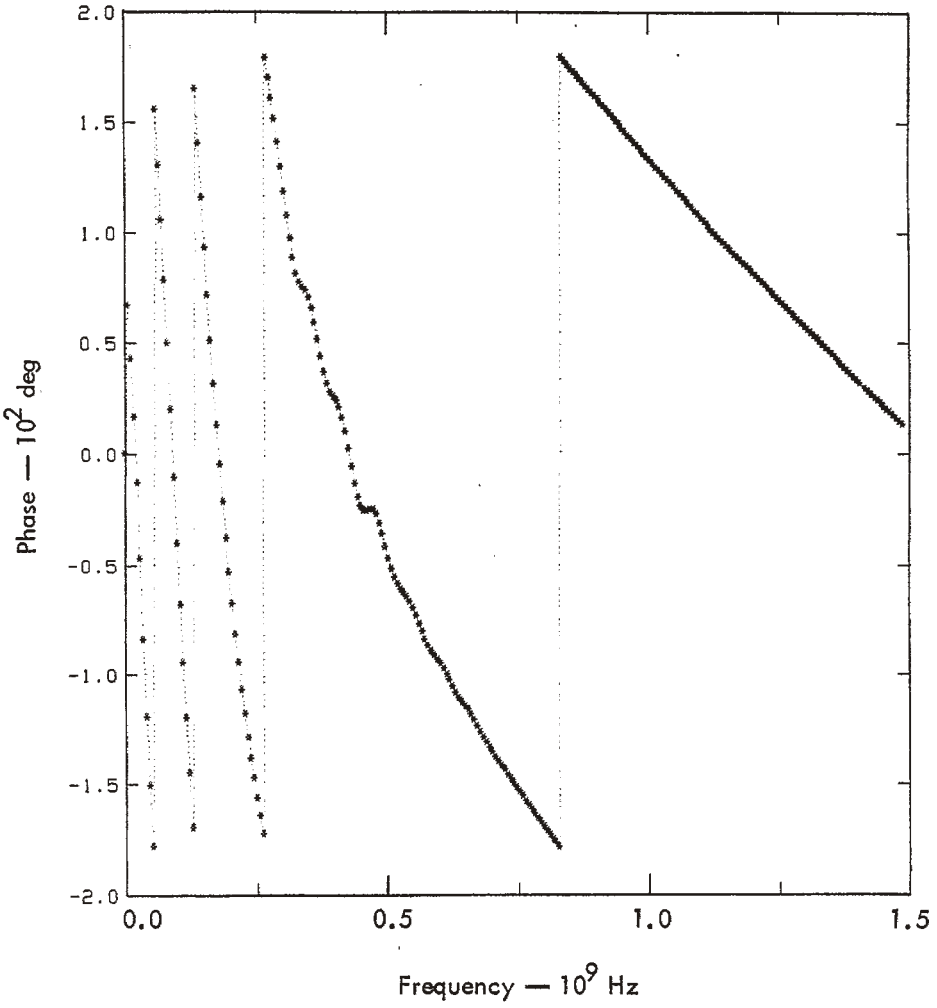

Fig. A7. (Continued.) (e) Phase of the boresight transfer admittance.

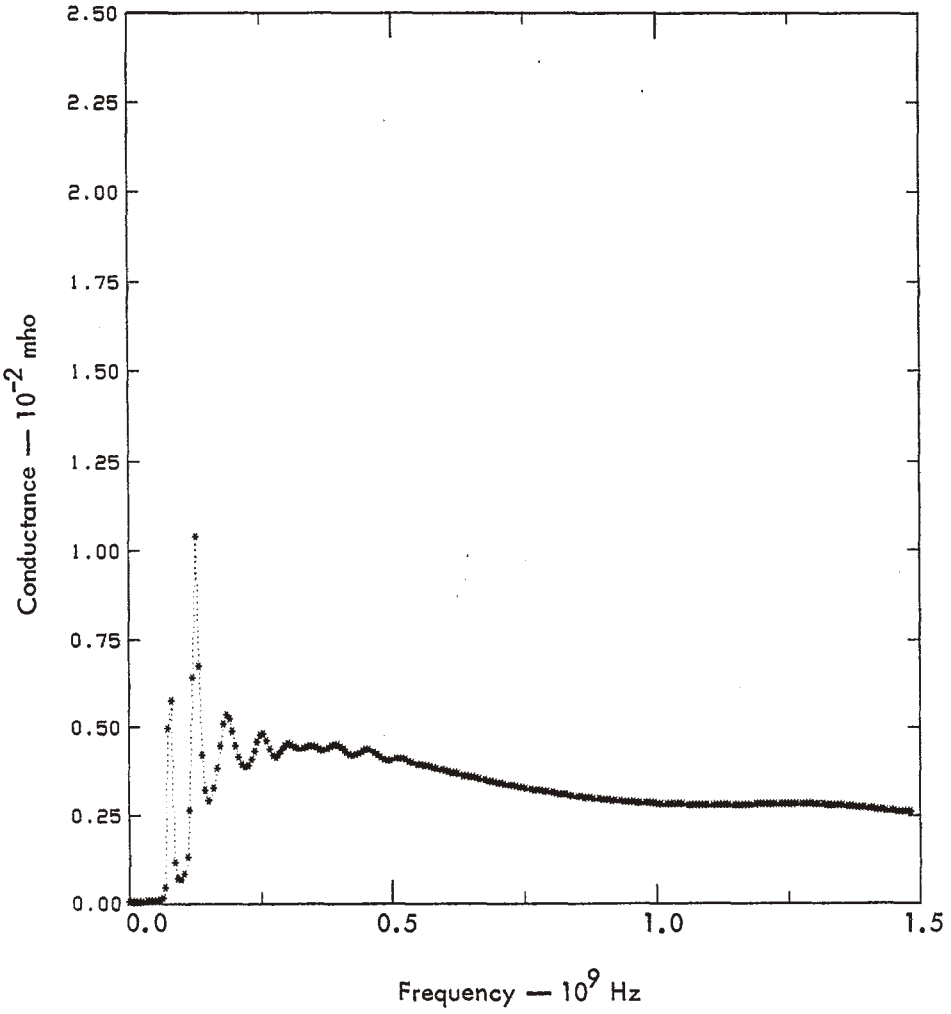

Fig. A8. Antenna characteristics for antenna A8 in Table A1.
(a) Real part of the driving-point admittance.
(Continued on the following four pages.)

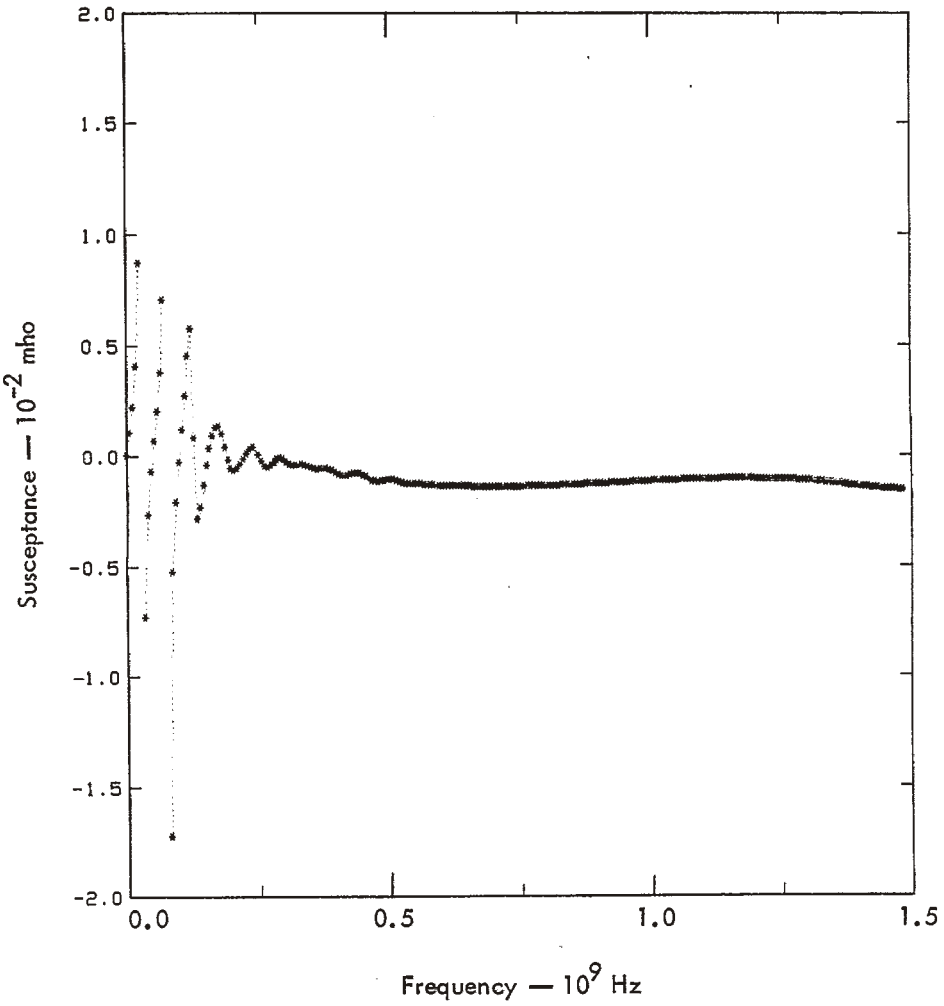

Fig. A8. (Continued.) (b) Imaginary part of the driving-point admittance.

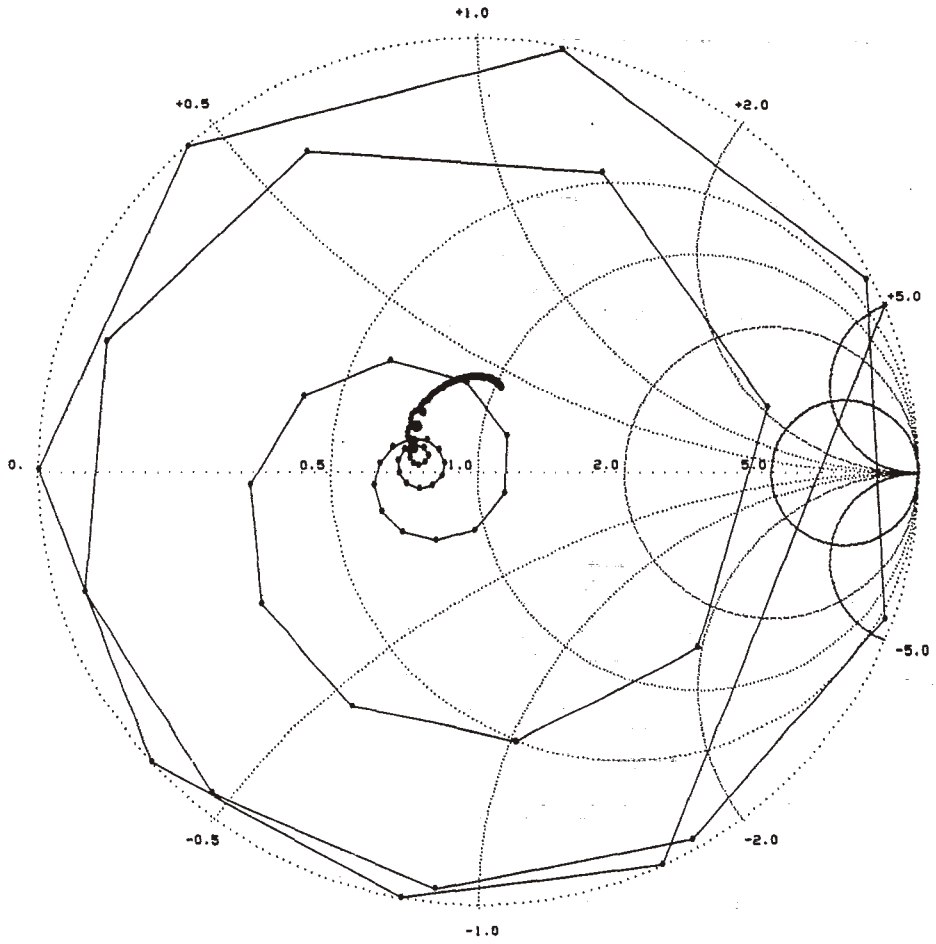

$Z_0 = 300\ \Omega$

Fig. A8. (Continued.) (c) Driving-point impedance normalized to 300 Ω.

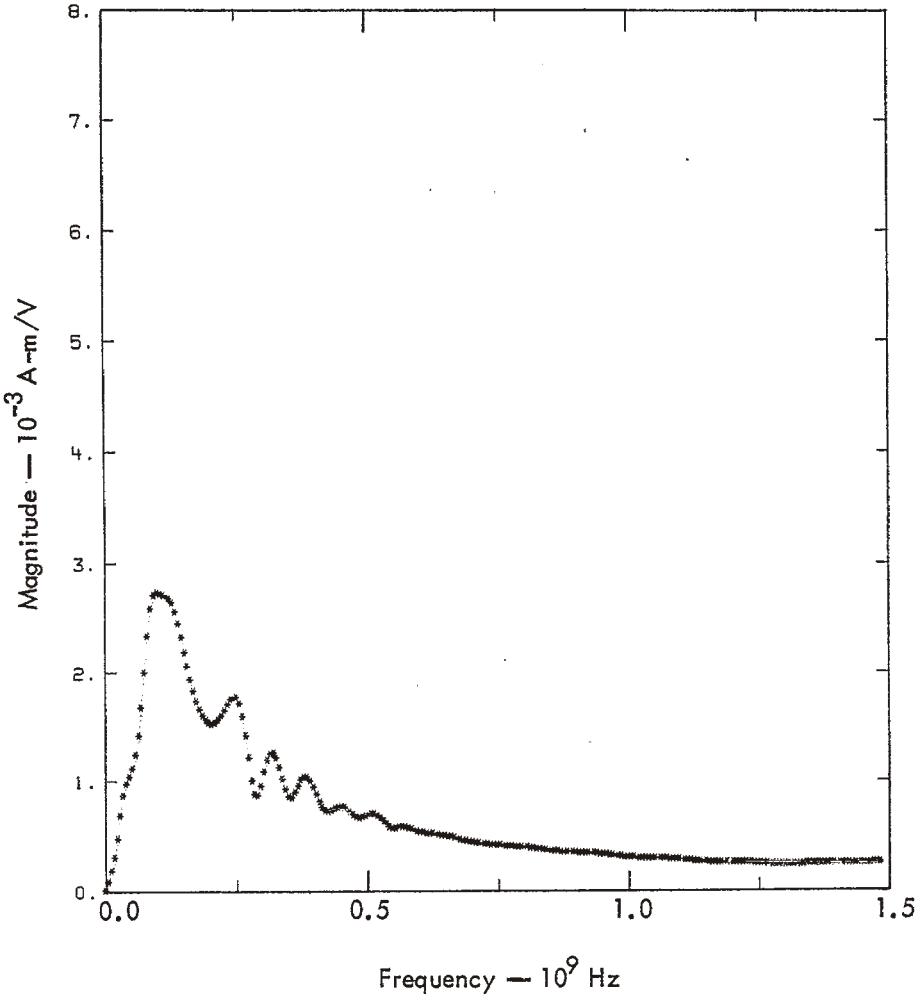

Fig. A8. (Continued.) (d) Magnitude of the boresight transfer admittance.

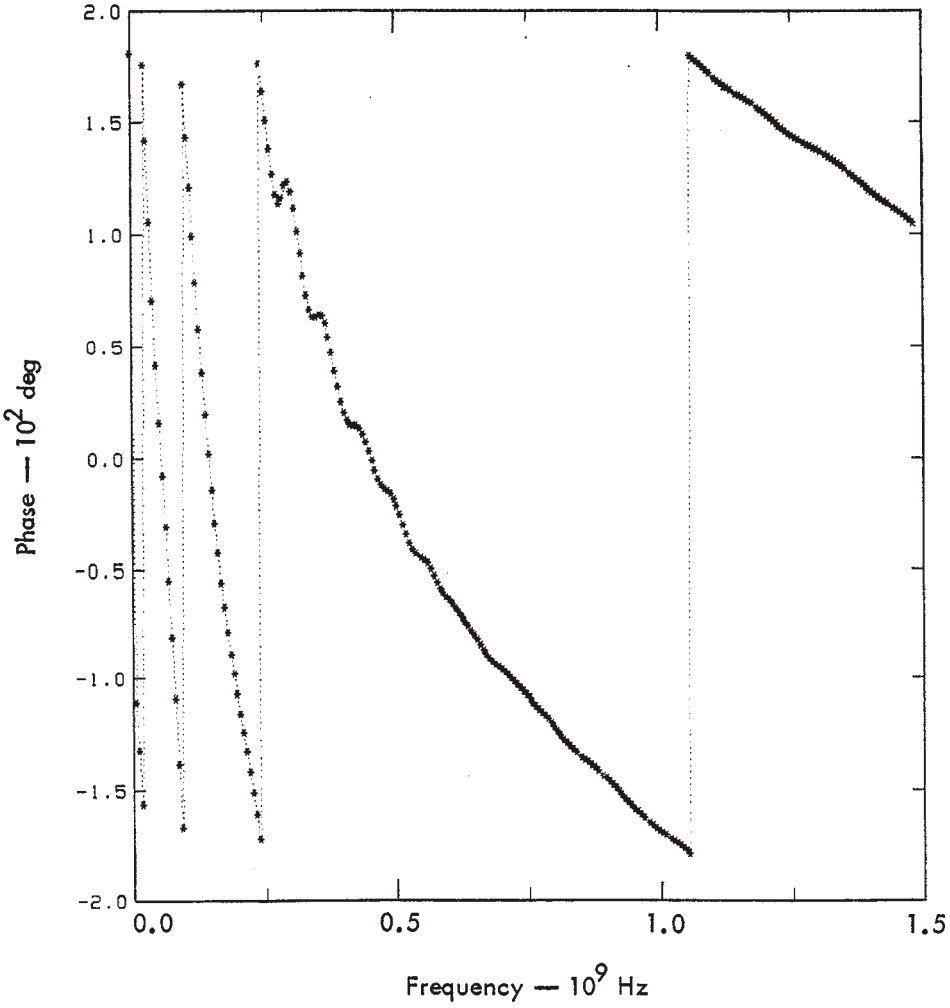

Fig. A8. (Continued.) (e) Phase of the boresight transfer admittance.

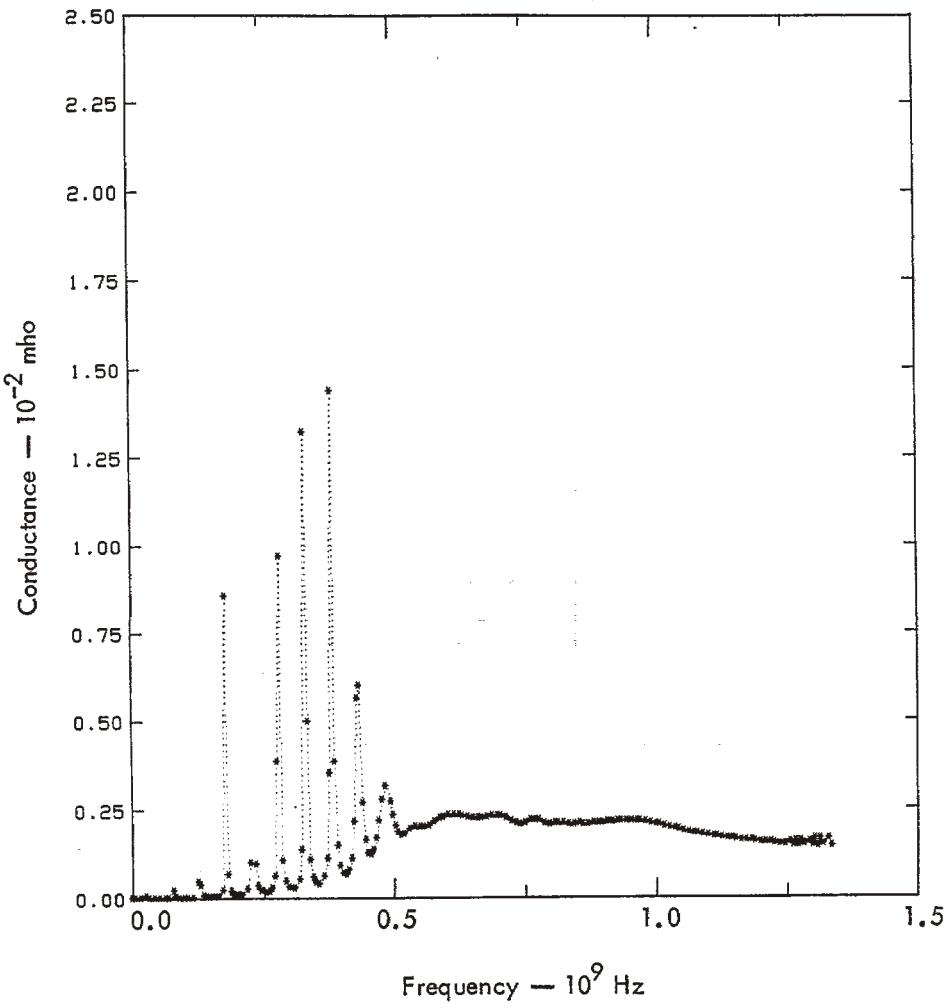

Fig. A9. Antenna characteristics for antenna A9 in Table A1.
(a) Real part of the driving-point admittance.
(Continued on the following four pages.)

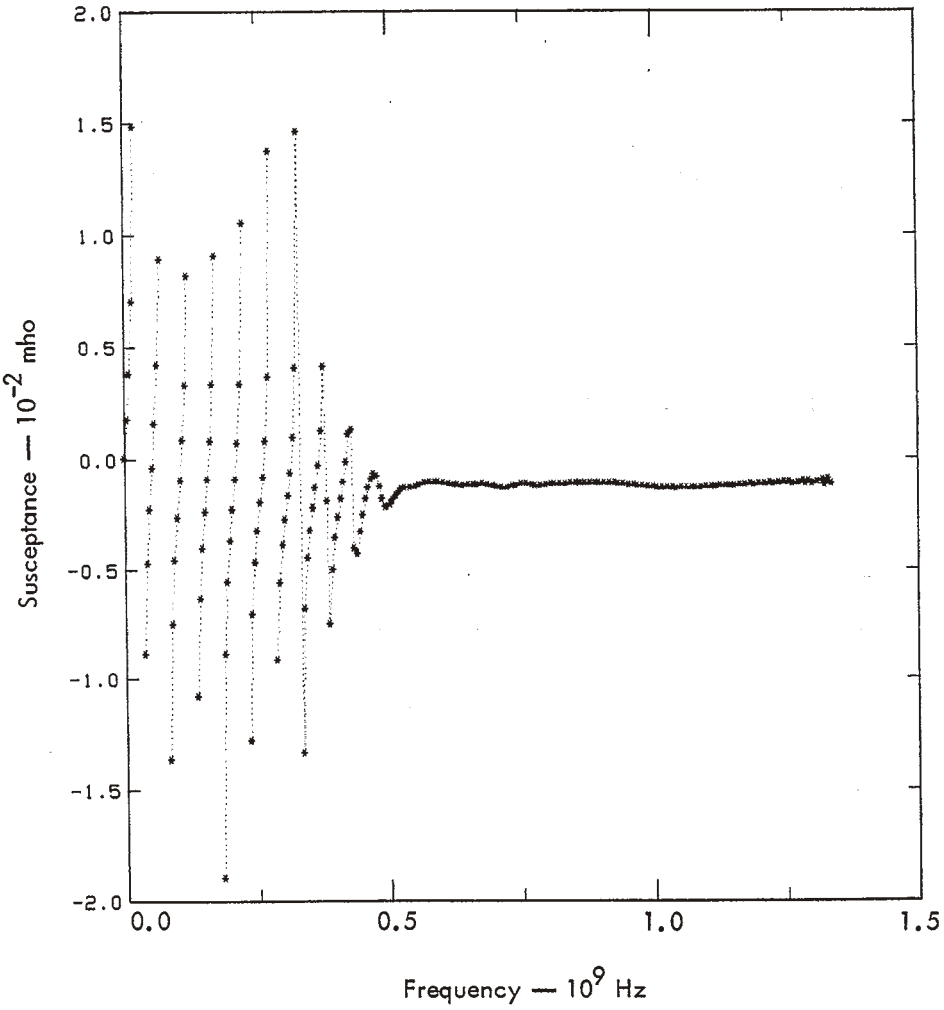

Fig. A9. (Continued.) (b) Imaginary part of the driving-point admittance.

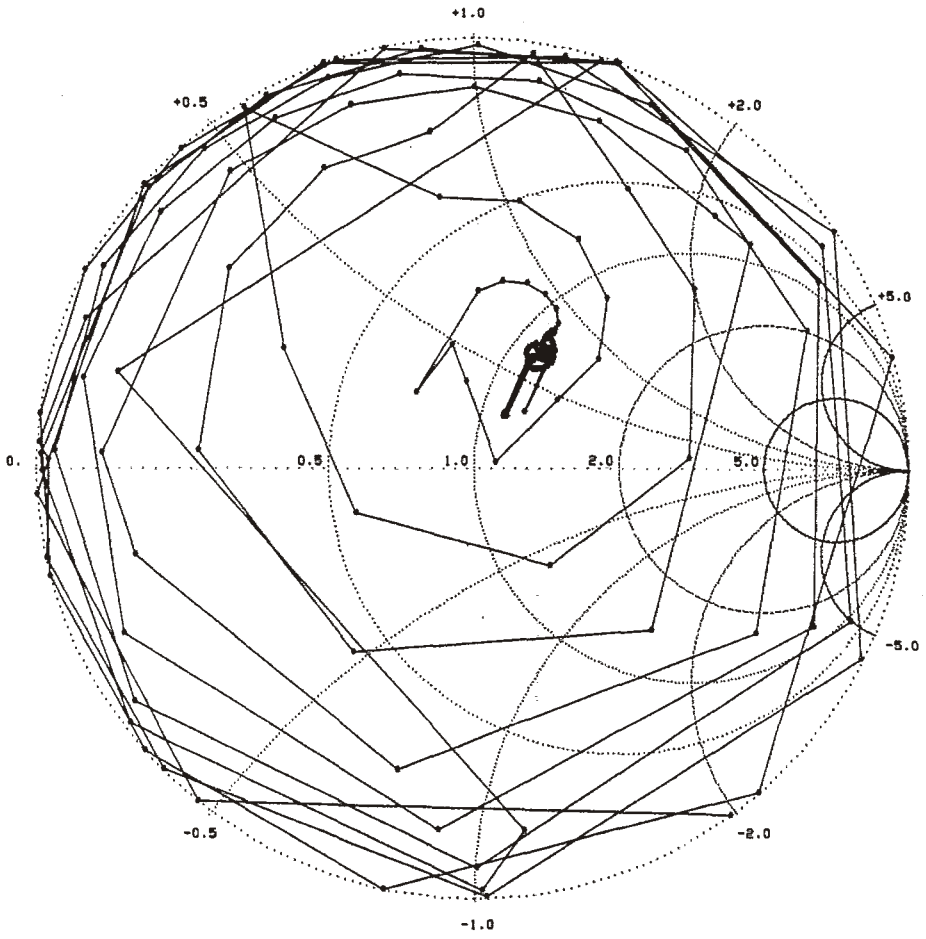

$Z_0 = 300\ \Omega$

Fig. A9. (Continued.) (c) Driving-point impedance normalized to 300 Ω.

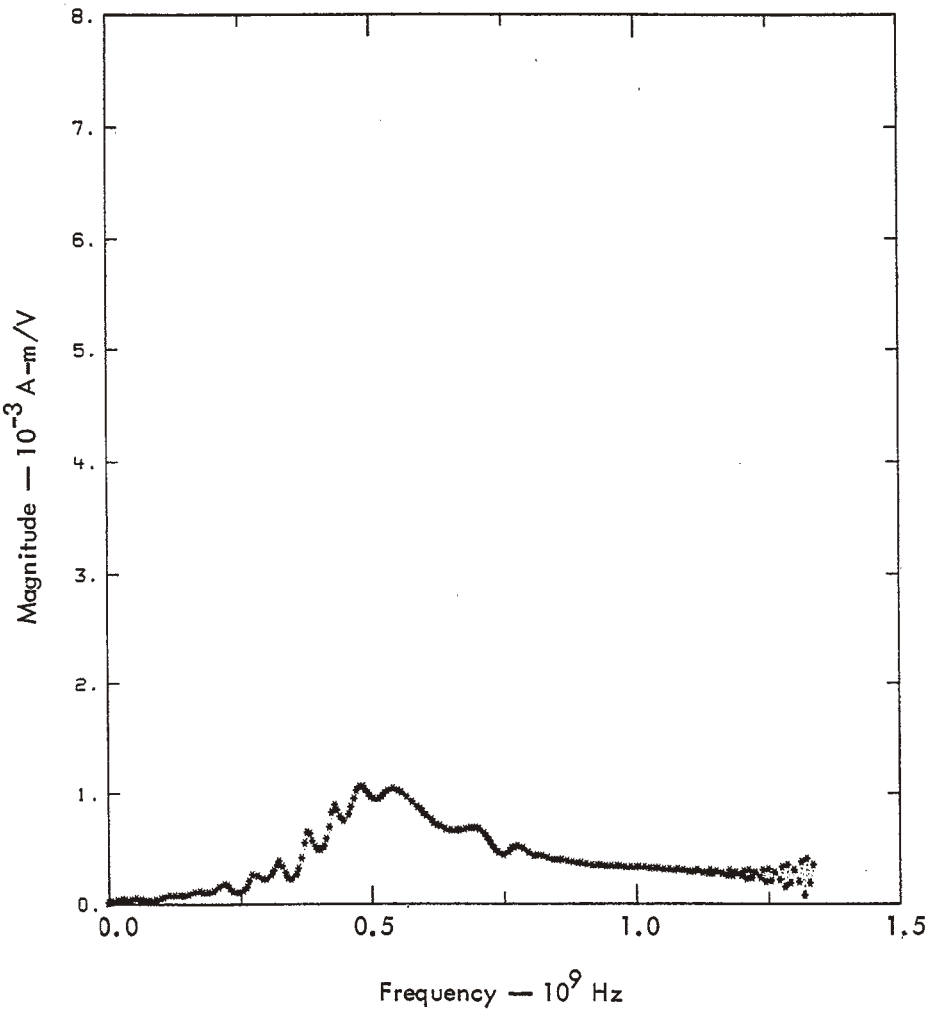

Fig. A9. (Continued.) (d) Magnitude of the boresight transfer admittance.

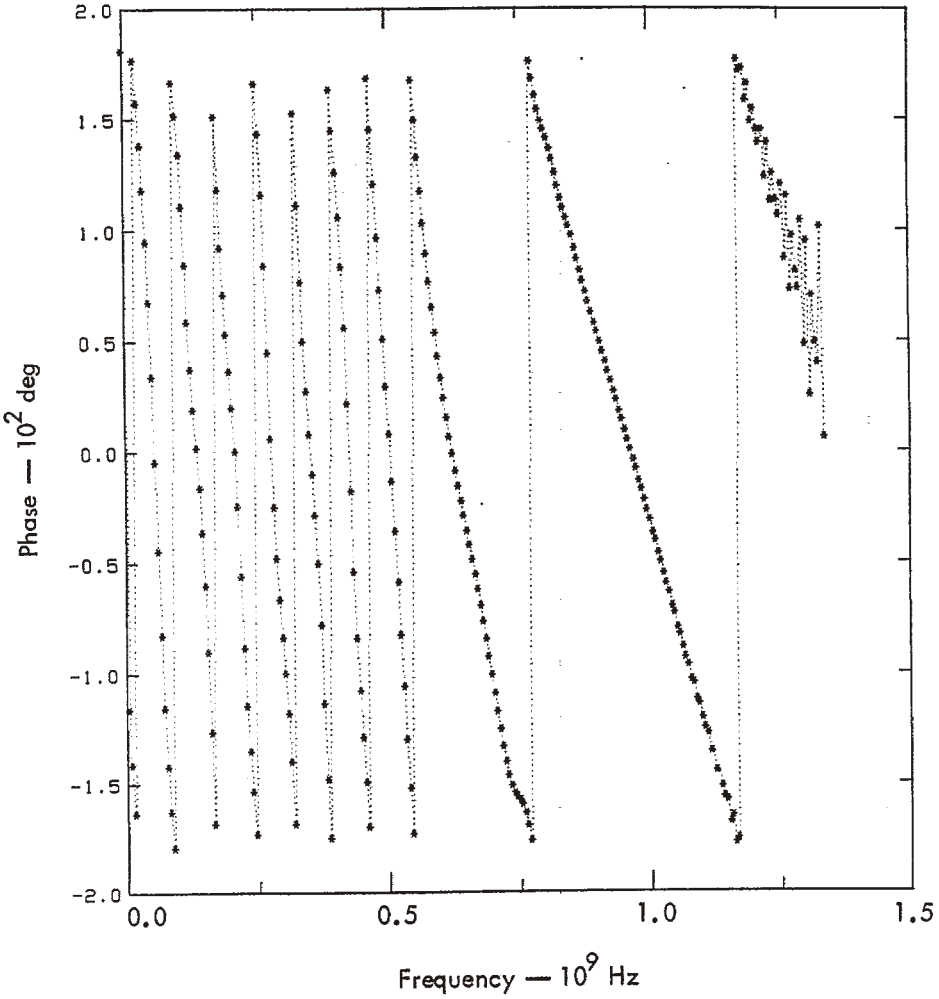

Fig. A9. (Continued.) (e) Phase of the boresight transfer admittance.

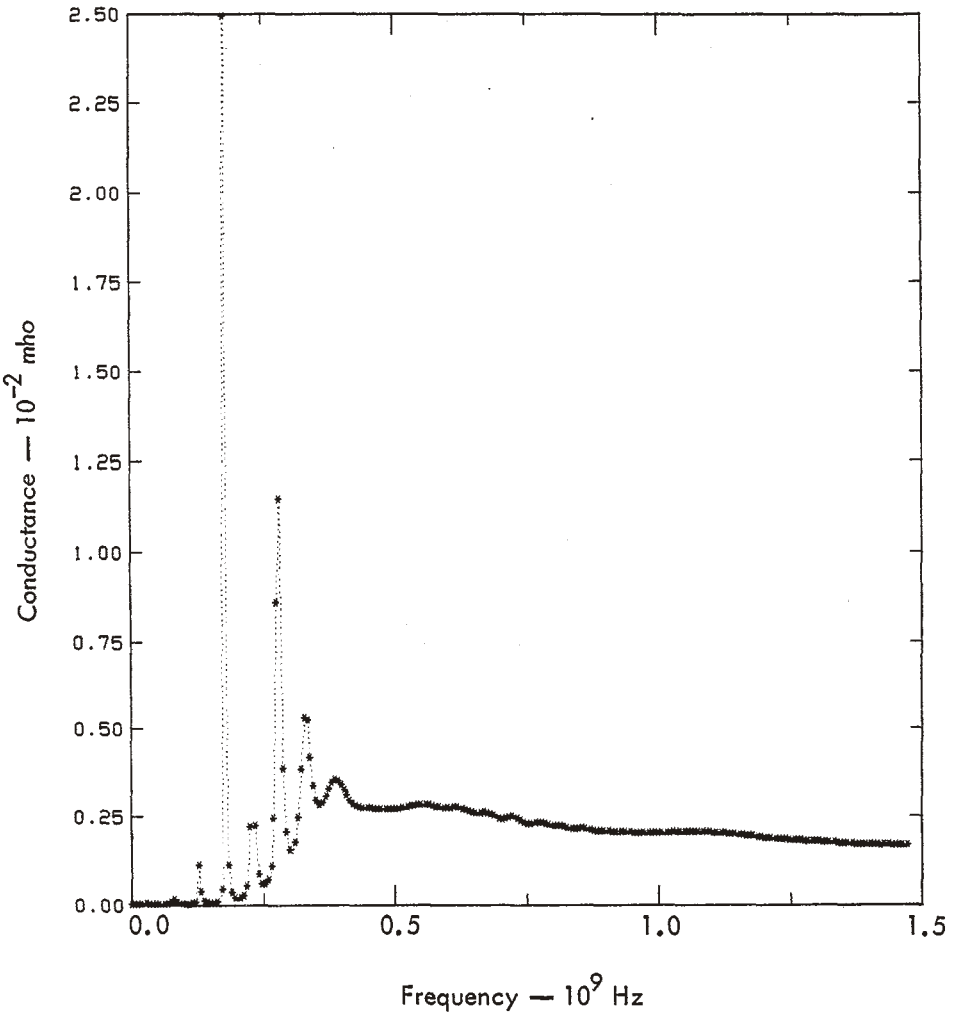

Fig. A10. Antenna characteristics for antenna A10 in Table A1.
(a) Real part of the driving-point admittance.
(Continued on the following four pages.)

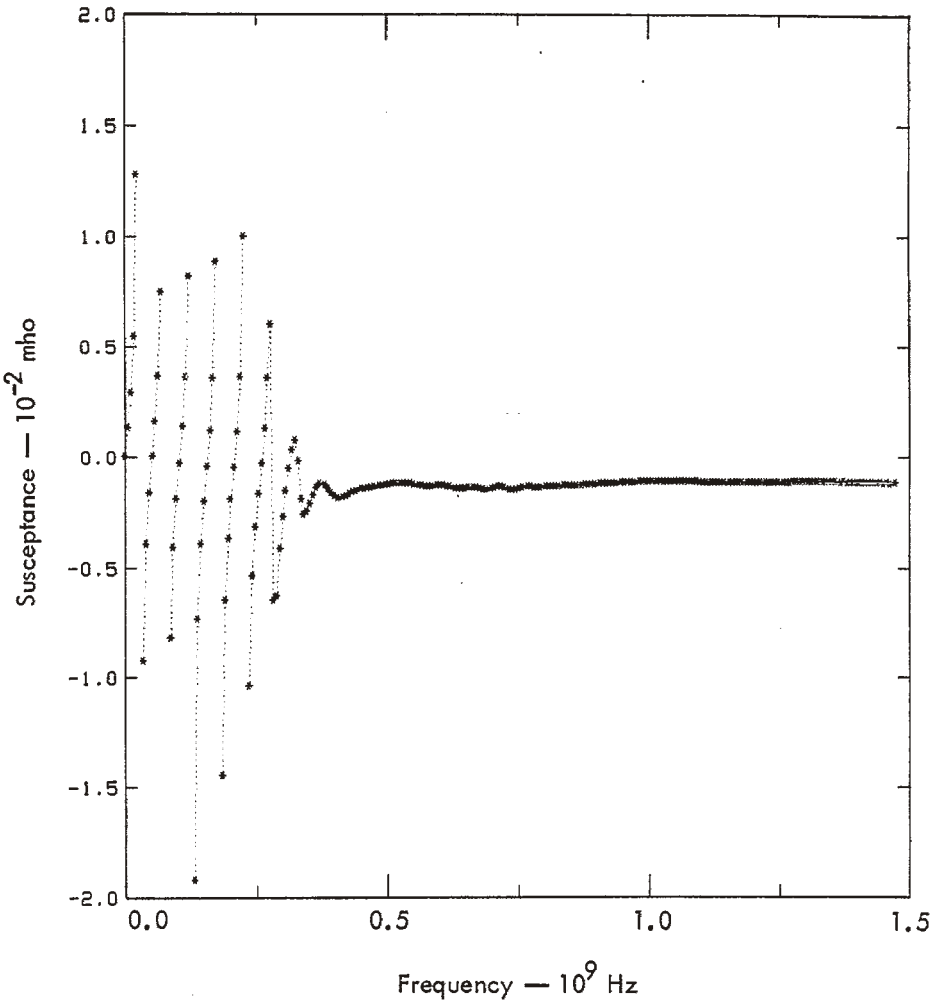

Fig. A10. (Continued.) (b) Imaginary part of the driving-point admittance.

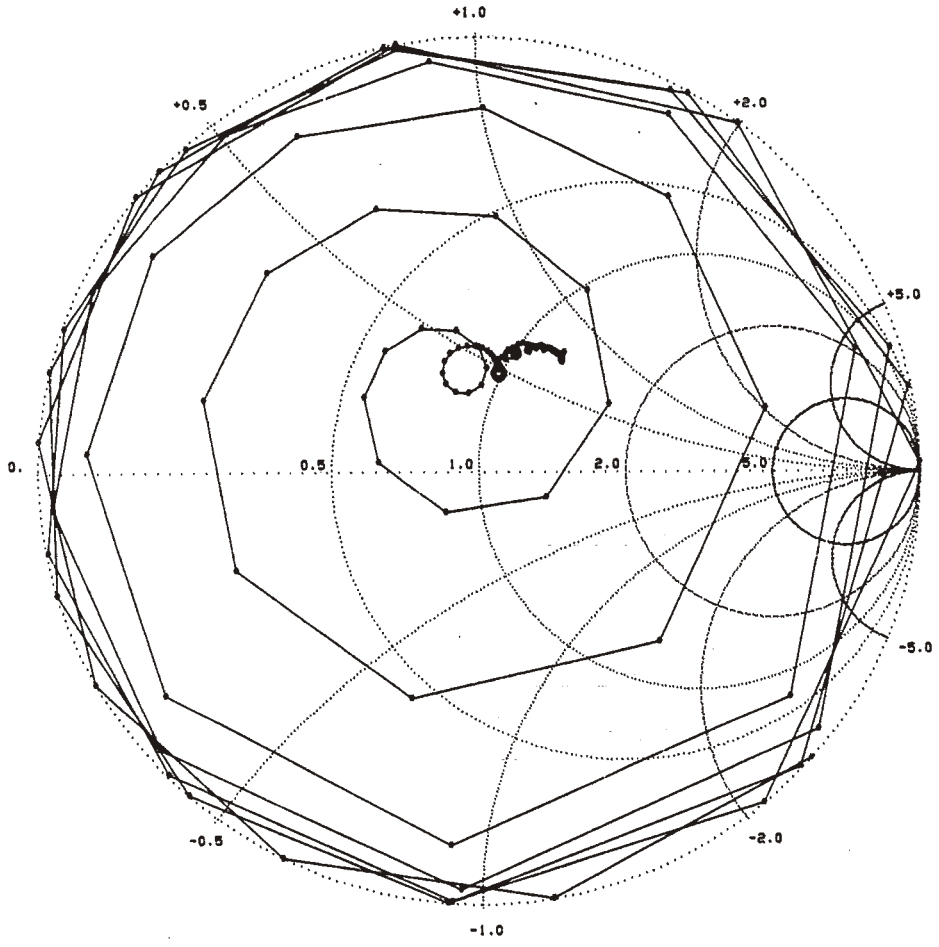

$Z_0 = 300\ \Omega$

Fig. A10. (Continued.) (c) Driving-point impedance normalized to 300 Ω.

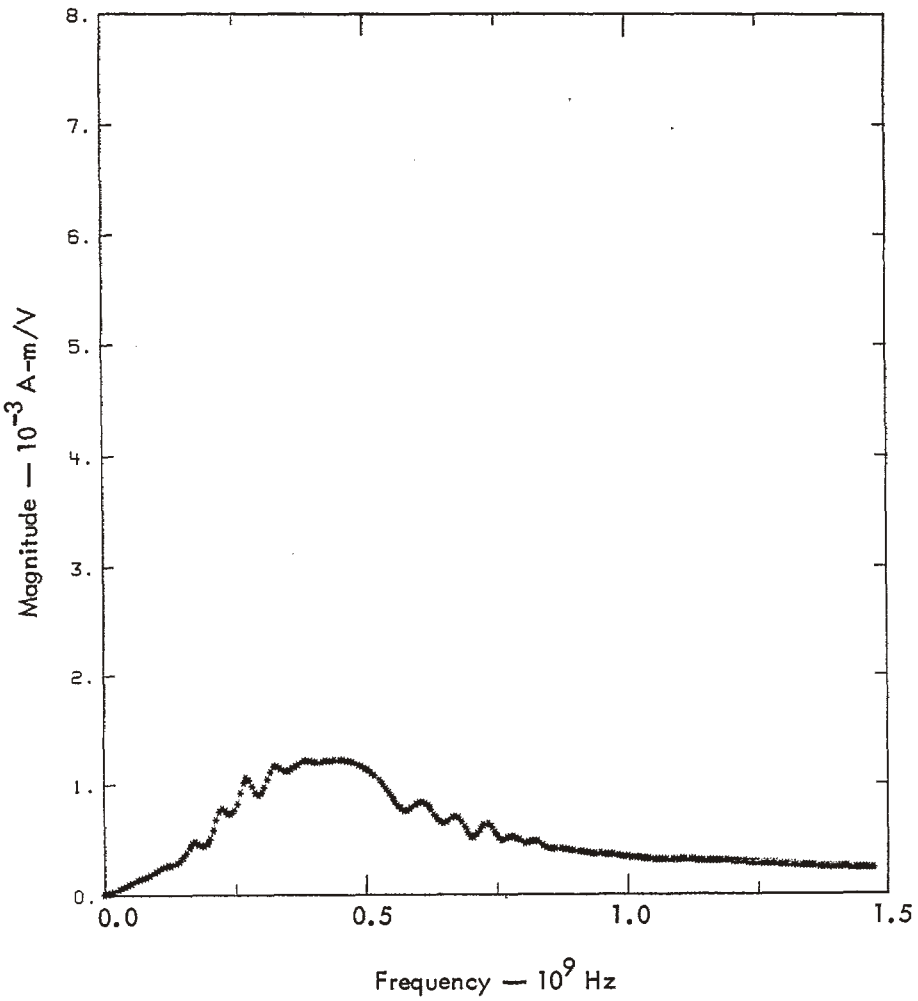

Fig. A10. (Continued.) (d) Magnitude of the boresight transfer admittance.

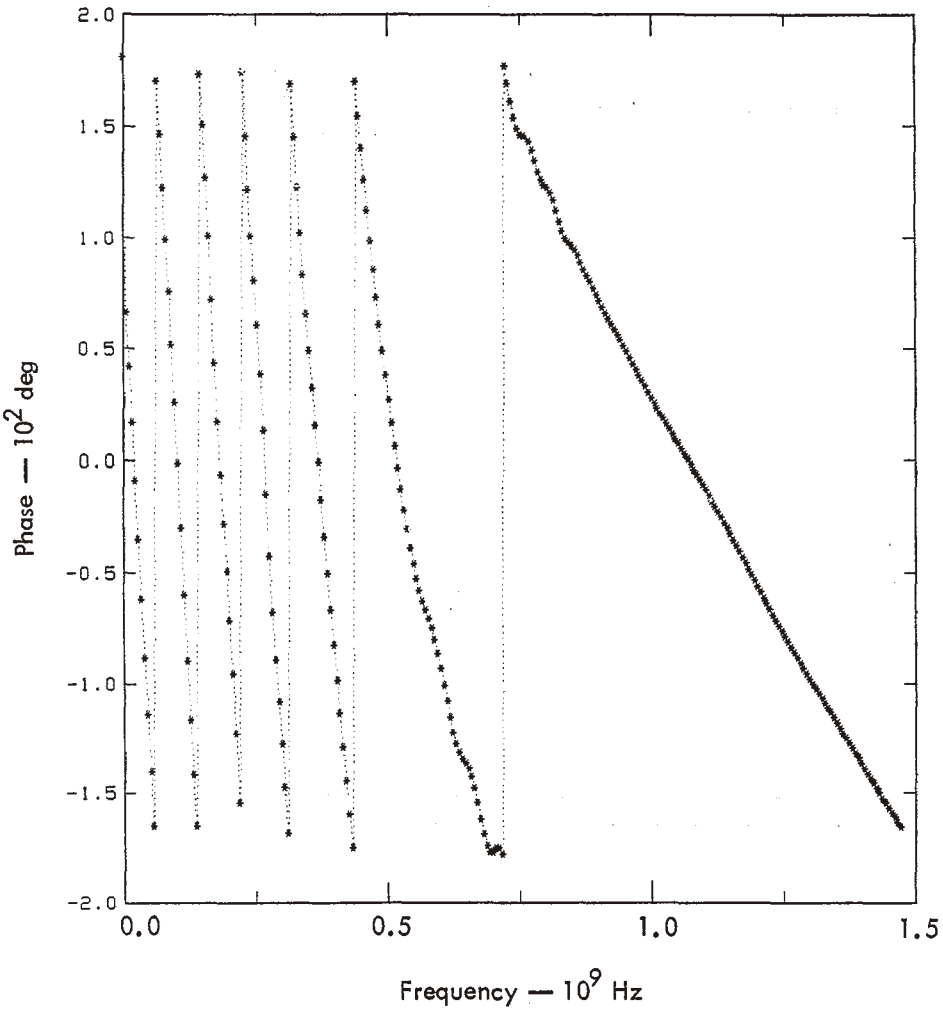

Fig. A10. (Continued.) (e) Phase of the boresight transfer admittance.

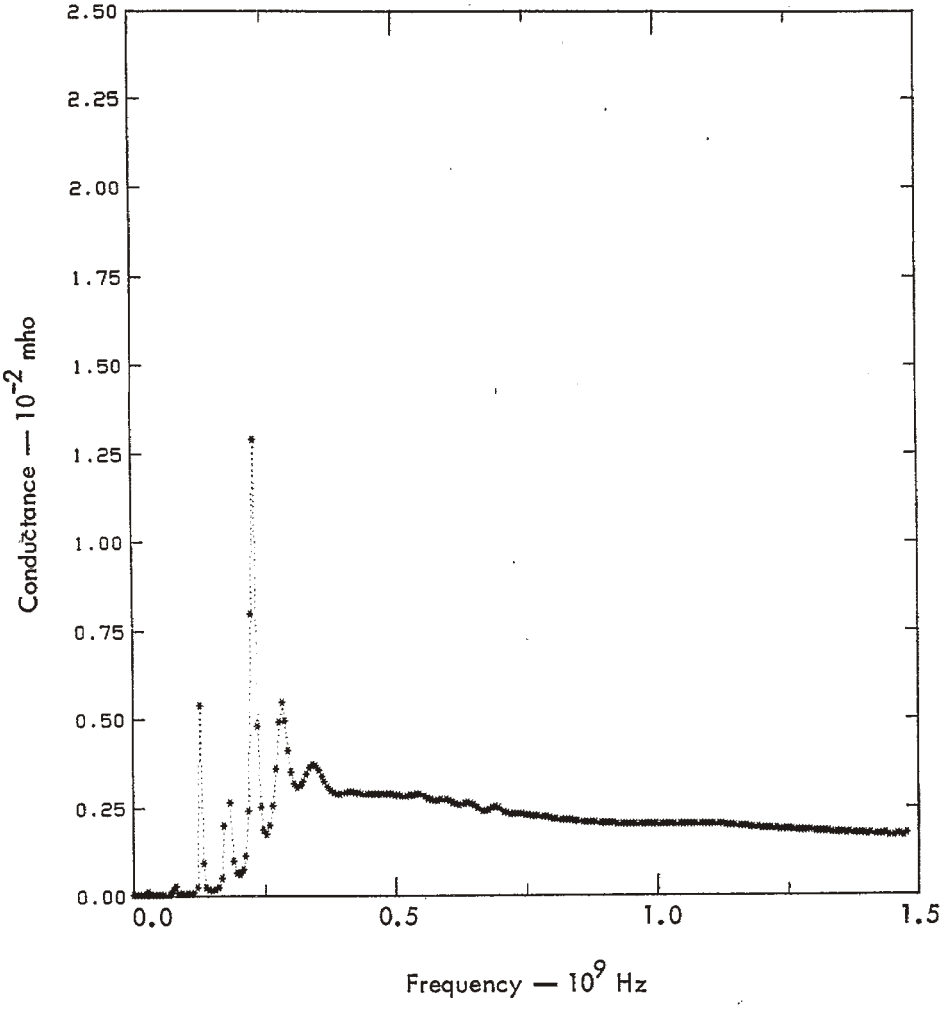

Fig. A11. Antenna characteristics for antenna A11 in Table A1.
(a) Real part of the driving-point admittance.
(Continued on the following four pages.)

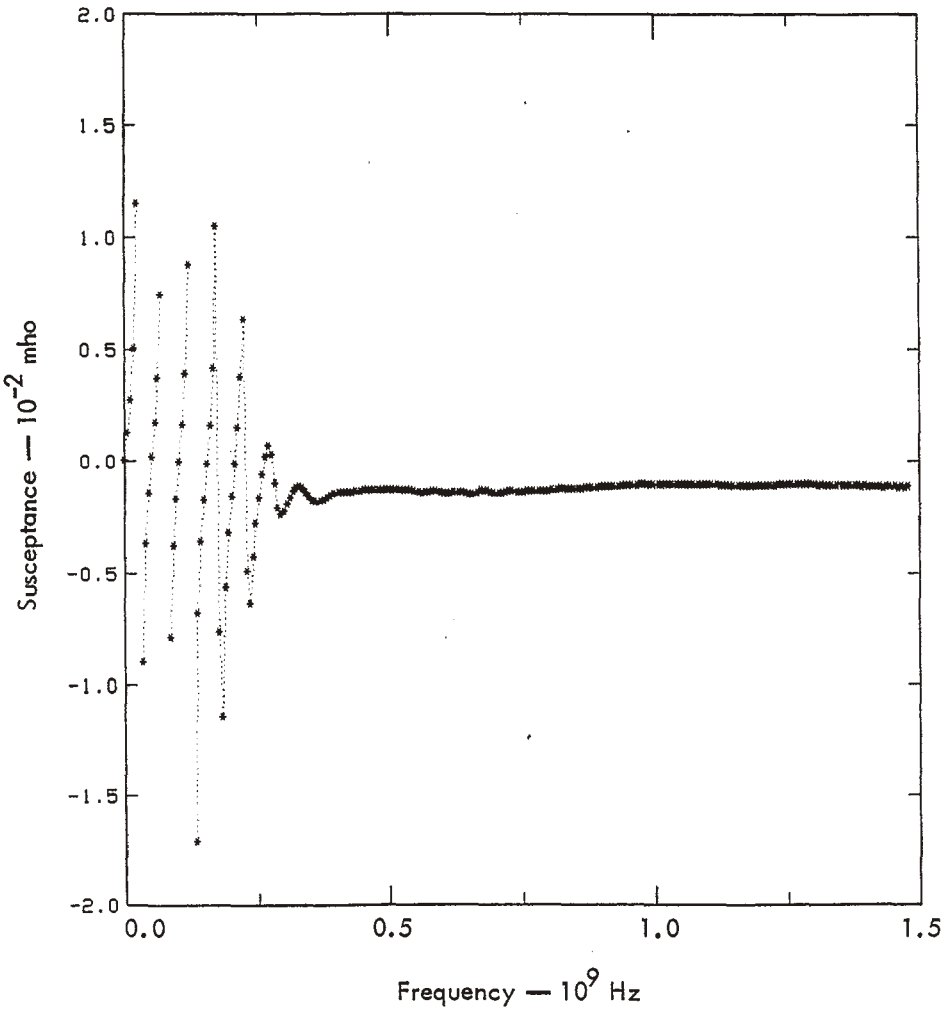

Fig. A11. (Continued.) (b) Imaginary part of the driving-point admittance.

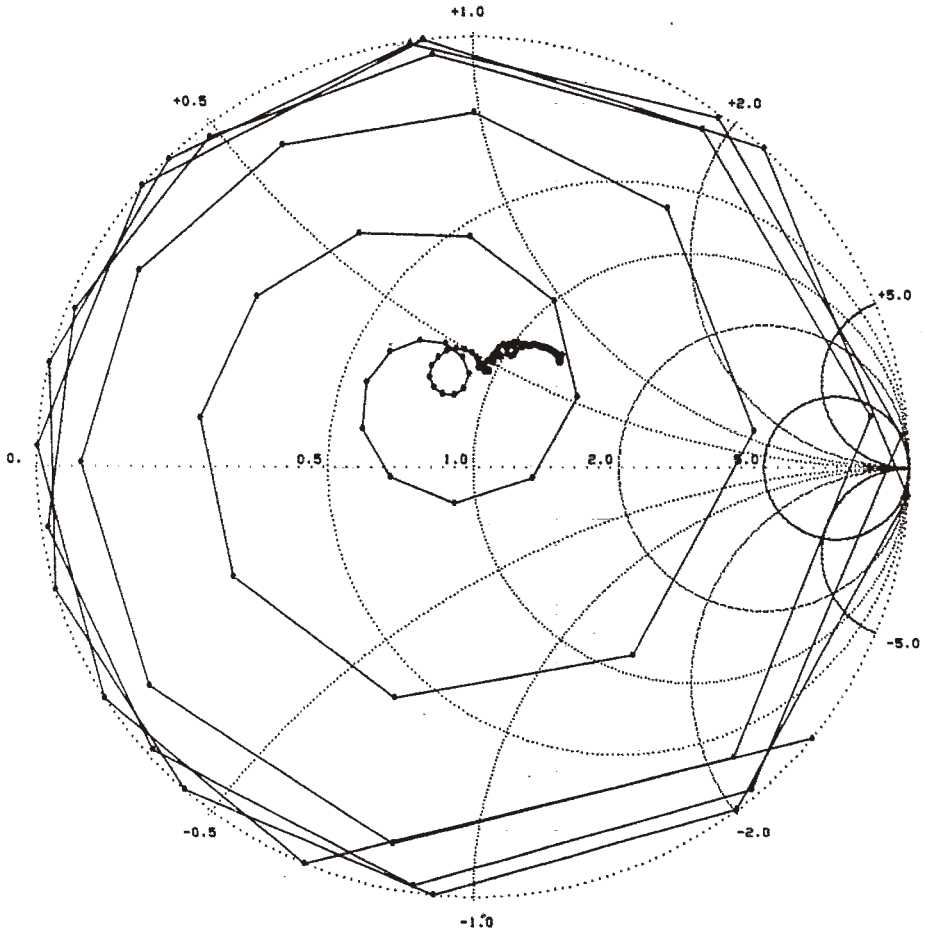

$Z_0 = 300\ \Omega$

Fig. A11. (Continued.) (c) Driving-point impedance normalized to 300 Ω.

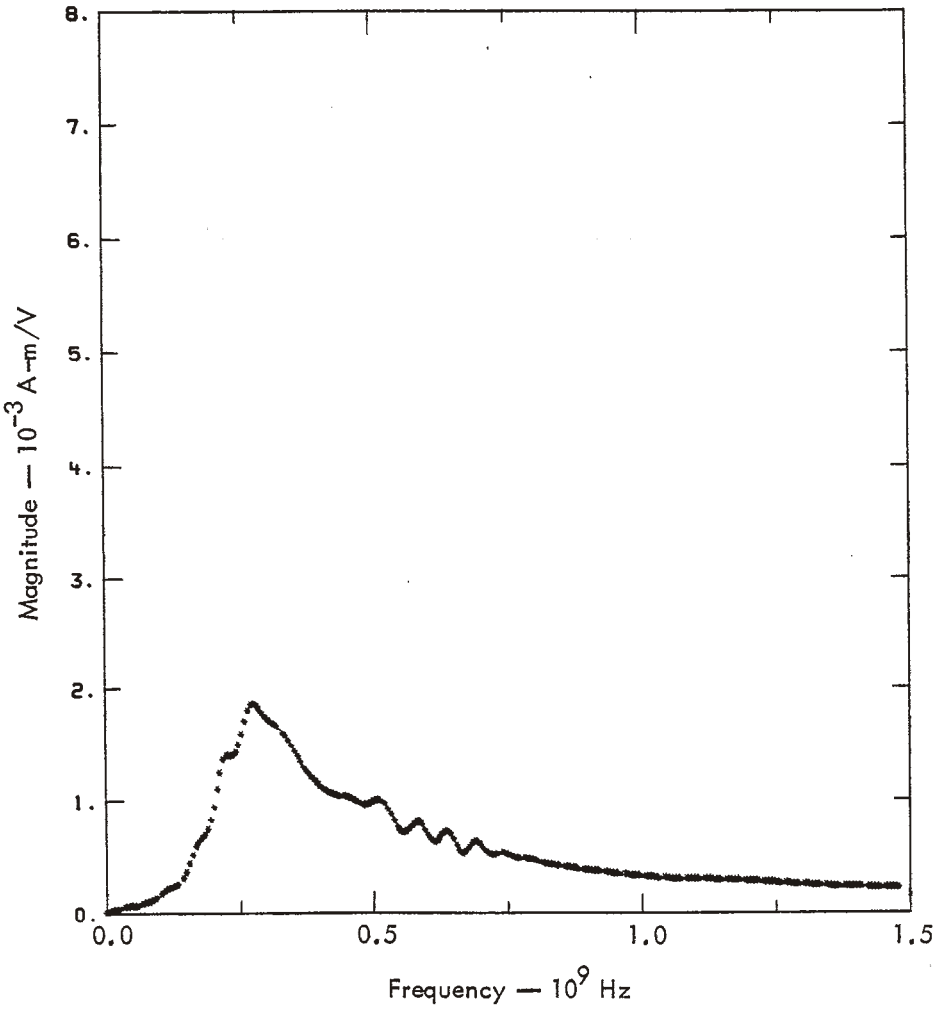

Fig. A11. (Continued.) (d) Magnitude of the boresight transfer admittance.

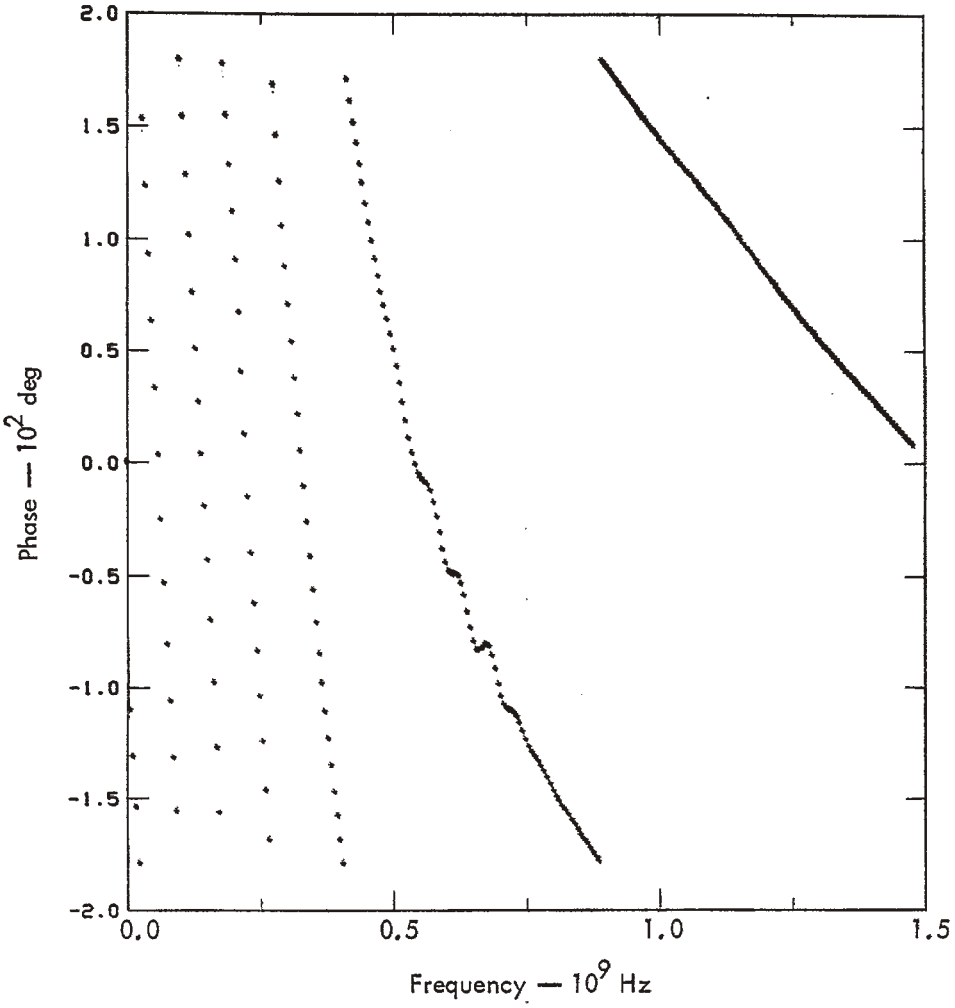

Fig. A11. (Continued.) (e) Phase of the boresight transfer admittance.

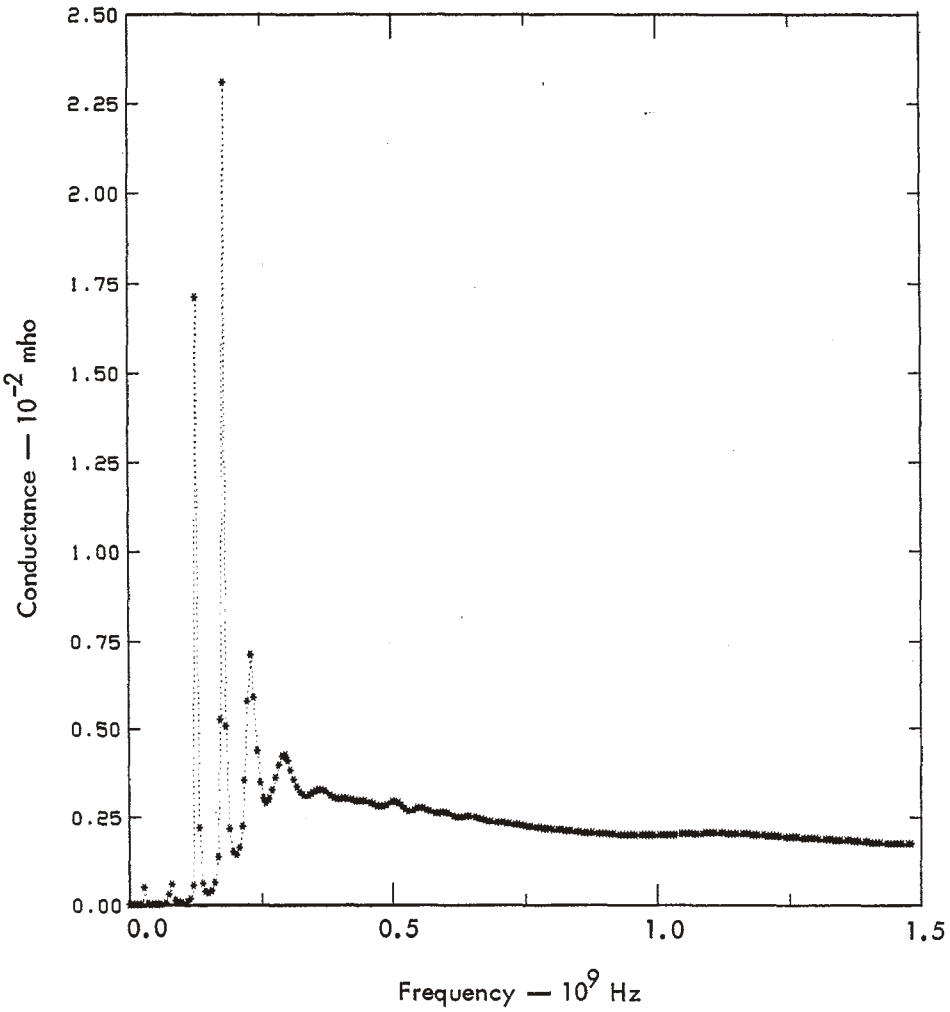

Fig. A12. Antenna characteristics for antenna A12 in Table A1.
(a) Real part of the driving-point admittance.
(Continued on the following four pages.)

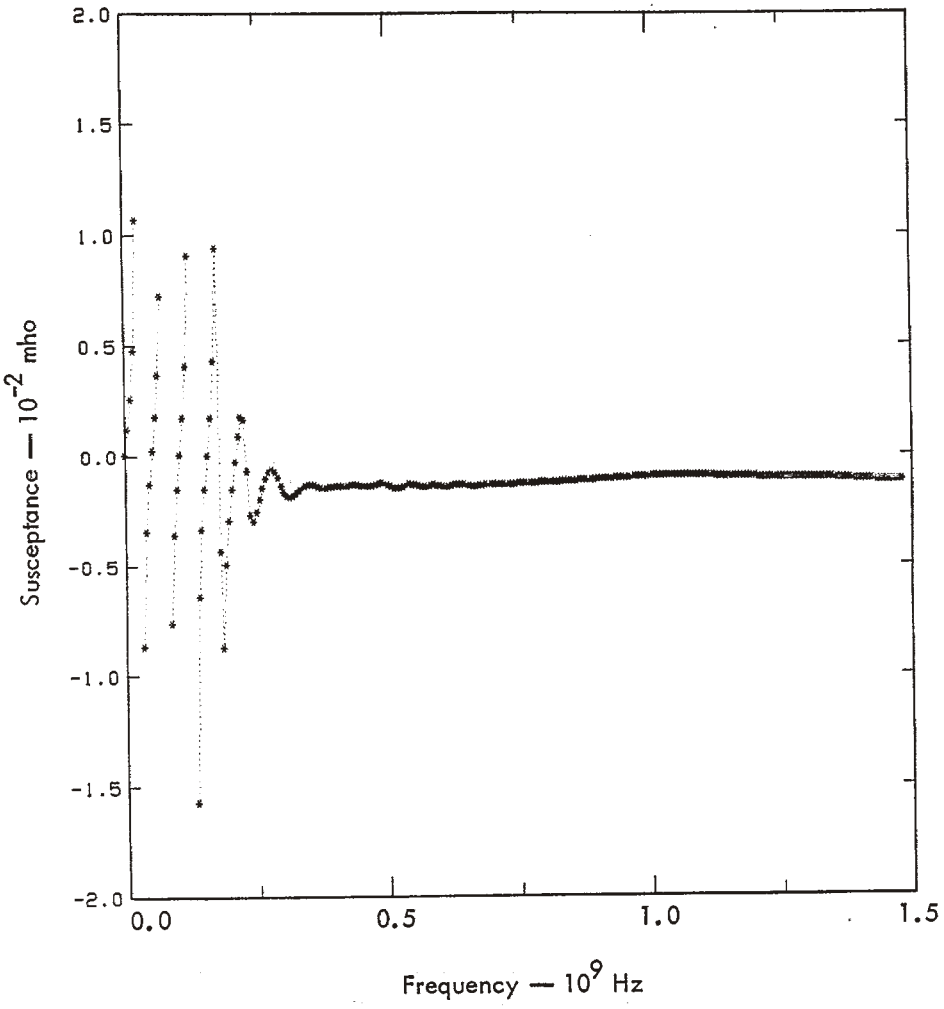

Fig. A12. (Continued.) (b) Imaginary part of the driving-point admittance.

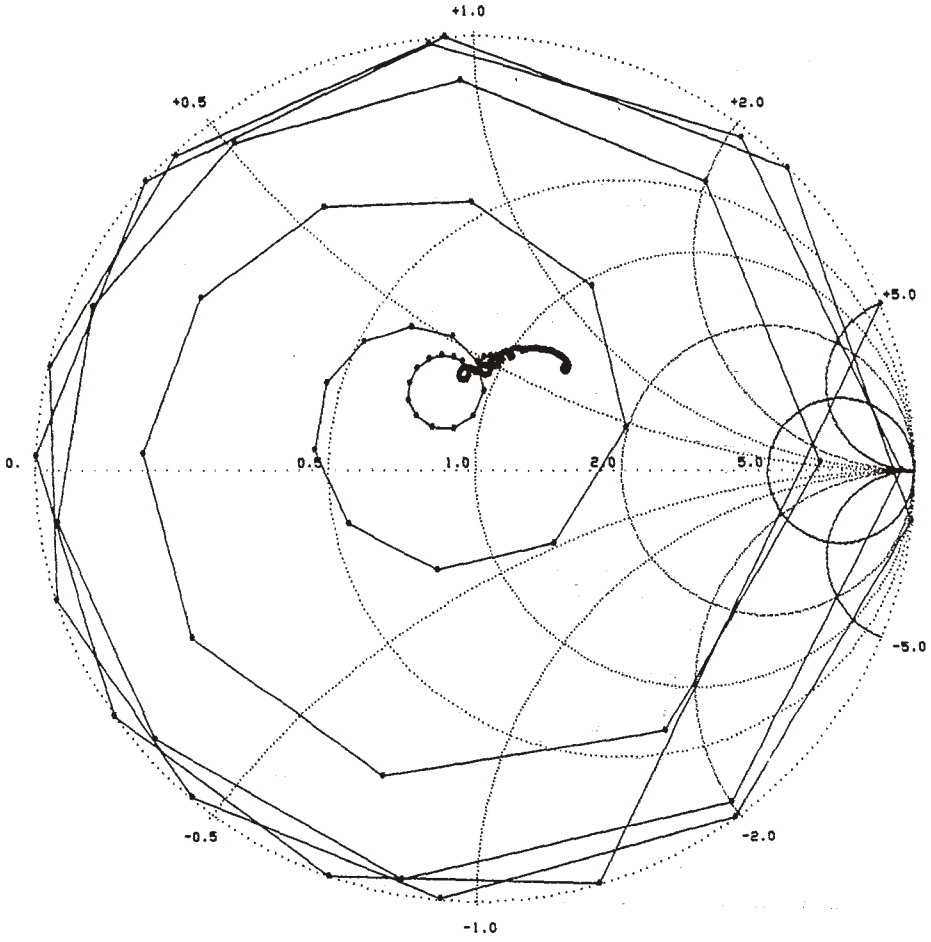

$Z_0 = 300\ \Omega$

Fig. A12. (Continued.) (c) Driving-point impedance normalized to 300 Ω.

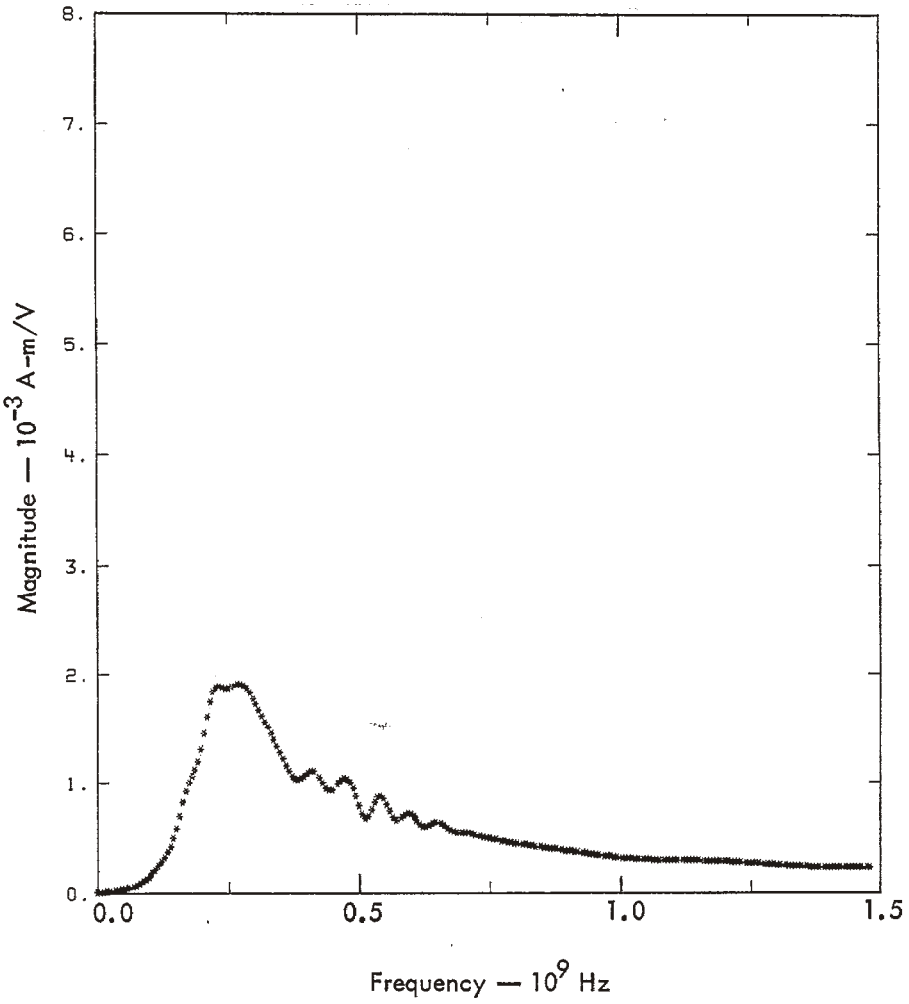

Fig. A12. (Continued.) (d) Magnitude of the boresight transfer admittance.

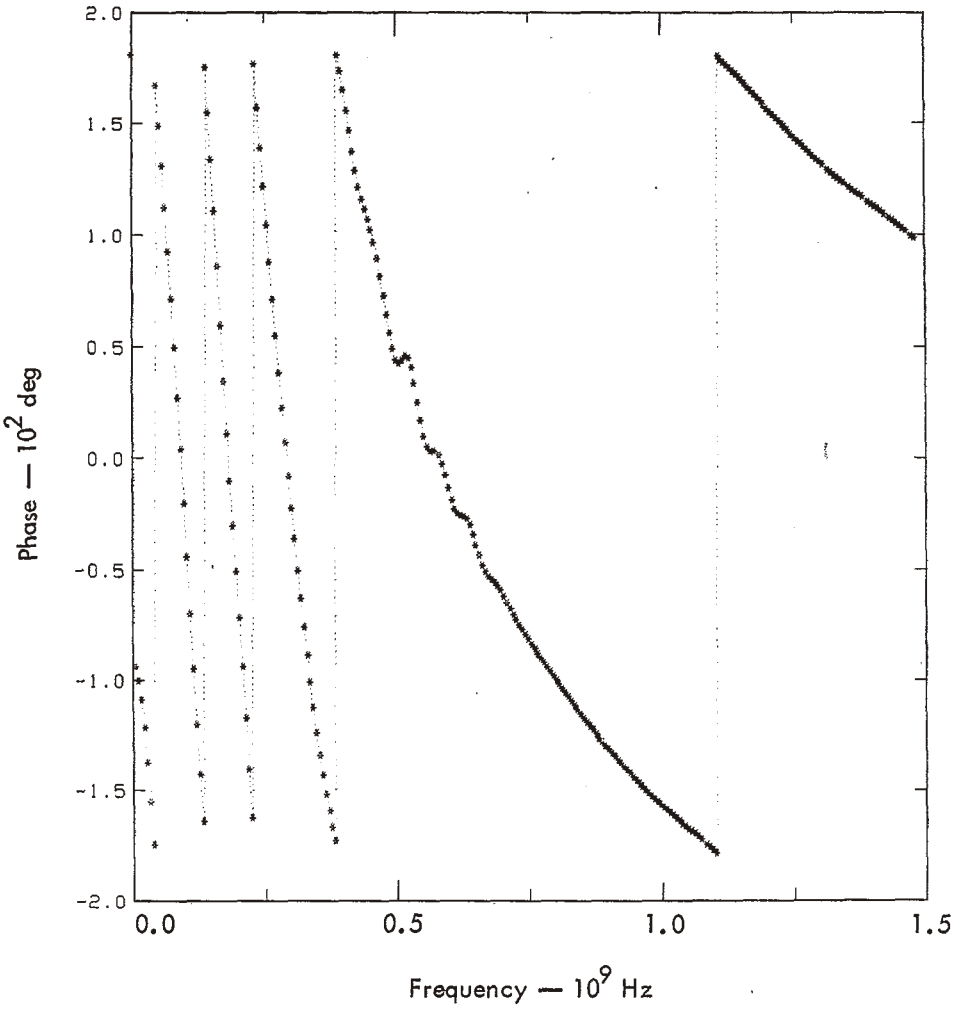

Fig. A12. (Continued.) (e) Phase of the boresight transfer admittance.